Optimization and Application of Time-of-Flight Secondary Ion Mass Spectrometry (ToF-SIMS) for the Detection of Nanomaterials in Tissue Thin Sections

DISSERTATION
zur Erlangung des Grades eines Doktors
der Naturwissenschaften

vorgelegt von
Lothar Veith (M. Sc.)

eingereicht bei der Naturwissenschaftlich-Technischen Fakultät
der Universität Siegen
Siegen 2018

Betreuer und erster Gutachter

Prof. Dr. Carsten Engelhard

Universität Siegen

Zweiter Gutachter

Prof. Dr. Joachim Wegener

Universität Regensburg

Tag der mündlichen Prüfung

28.01.2019

gedruckt auf alterungsbeständigem holz- und säurefreiem Papier

Abstract

The increasing use of nanoparticle (NP)-containing products leads to an enhanced emission of NP into the environment. The potential dangers associated with the exposition of organisms to these materials are barely investigated and the fate of the NP upon uptake into the body is not completely understood. One reason is the lack of suitable analytical techniques, which allow the sensitive detection of NP in tissue at high spatial resolution. Prerequisites for a reliable identification are high sensitivity, high mass resolution and high spatial resolution without the need for markers.

Time-of-Flight secondary ion mass spectrometry (ToF-SIMS) is promising in this regard because it allows the simultaneous detection of atomic and molecular species from surfaces without markers. However, its potential for the detection of NP in tissue has not yet been adequately explored. In the scope of this work, a suitable ToF-SIMS method is developed and optimised for the analysis of a variety of oxidic NP in lung tissue sections. The suitability of ToF-SIMS for the successful detection of nanomaterials in biological tissue is demonstrated by means of correlations and cross-validations of ToF-SIMS data with the results of reference techniques.

In this thesis, rat lung tissue sections, containing different kinds of nanoparticles are analysed by ToF-SIMS and compared with reference techniques. Paramagnetic Fe_2O_3/SiO_2 (core/shell) NP (primary particle size 10-20 nm; aggregate size 190 ± 20 nm) are detected by microscopic techniques (dark-field and bright-field microscopy) and ToF-SIMS colocalizing in the tissue sections. The NP are mostly attached to alveolar wall and only marginally internalized by cells. The colocalization of ToF-SIMS signal distributions for $^{56}Fe^+$ and $^{28}Si^+$ proves that the core/shell structure of the particles remains intact in the tissue. The phosphocholine head group ($C_5H_{15}NPO_4^+$) is colocalized with tissue (CH_4N^+) but not with the NP indicating that lipids do not adsorb onto NP under these conditions.

The distribution of fluorescence-tagged SiO_2 NP (25 nm) in rat lung tissue is revealed by fluorescence microscopy and ToF-SIMS. Extremely similar signal distributions for the fluorescence tag and ToF-SIMS signals (SiO_3^-) are obtained. Furthermore, the distributions of protein (CN^-) and phosphate-based signals (PO_3^-) can be related to the particle distribution.

Rat lung tissue sections inhomogenously laden with CeO_2 NP (10-200 nm) are subjected to successive analyses by first micro X-ray fluorescence (μ-XRF) and second ToF-SIMS. This approach allows a relatively fast screening of the complete section for elevated Ce levels at 25 μm lateral resolution, before selecting suitable regions-of-interest for high-resolution ToF-SIMS analysis at submicrometer lateral resolution (670 nm). Ce-related signal distributions (*e.g.* $^{140}Ce^+$, $^{140}CeO^+$, $^{140}CeO_2^+$) are detected along tissue-related signals (K_2CN^+) at a mass resolution of $R = 4000$. Besides pre-analyses, the μ-XRF also allows a coarse cross-validation of the ToF-SIMS signal distributions.

ZrO_2 NP (primary sizes of 9-10 nm) are mainly detected as agglomerates in phagocytic cells by both high-spatial resolution techniques, ToF-SIMS and ion beam microscopy (IBM). Both techniques detect ZrO_2 related signals at high lateral resolutions (400-600 nm for ToF-SIMS and about 1000 nm for IBM). Only small quantities of NP are found in the lung epithelium. Besides the NP-related signals, S and P signal from IBM colocalize with PO^+ and SO_2^+ from ToF-SIMS. The presence of S-, P- and Zr-related signals in both techniques enables a cross-validation of the results. Additionally, ToF-SIMS signals indicating the distribution of certain compounds such as phospholipids ($C_4H_8N^+$, $C_6H_{12}N^+$, $C_5H_{15}NPO_4^+$) and amino acids (K_2CN^+, $C_2H_6N^+$, $C_3H_8N^+$) are detected at mass resolutions of up to 9000.

In summary, different oxidic nanoparticle types with sizes from 9 nm to more than 200 nm are directly detected by ToF-SIMS (without the need for markers) in rat lung tissue sections. The results are confirmed by independent techniques such as bright- and dark-field microscopy, μ-XRF and IBM. The presented ToF-SIMS analyses reveal the distribution of nanoparticles at high confidence and provide further elemental and molecular information from the particle-surrounding matrix (*e.g.* amino acids or lipid residues). Lateral resolutions of 400 nm and mass resolutions of up to 9000 with the ability to acquire organic and inorganic signals simultaneously across the whole mass-range are unique features highlighting the great potential of ToF-SIMS for the detection of nanoparticles in tissue. These results serve as a basis for the analysis of the fate of the nanoparticles in mammalian bodies for future nanotoxicology studies.

Zusammenfassung

Die steigende Anzahl der Anwendungen von Nanopartikel (NP) -haltigen Produkten führt zu einer verstärkten Emission von NP in die Umwelt. Die möglichen Gefahren, die von einer Exposition durch diese Materialien ausgehen, sind noch nicht vollständig bekannt. So ist zum Beispiel der Verbleib der NP bei einer Aufnahme in den Körper nicht vollständig verstanden. Ein Grund dafür ist der Mangel an geeigneten analytischen Techniken, die den empfindlichen Nachweis von NP im Gewebe bei hoher räumlicher Auflösung ermöglichen. Die Anforderungen für eine zuverlässige Identifikation der NP sind eine hohe Empfindlichkeit, hohe Massenauflösung und hohe räumliche Auflösung ohne die Notwendigkeit für den Einsatz von Markern.

Flugzeit-Sekundärionenmassenspektrometrie (ToF-SIMS) ist für diese Anwendung eine sehr vielversprechende Methode, da diese Technik die gleichzeitige direkte Detektion von atomaren und molekularen Spezies von Oberflächen ohne den Einsatz von Markern ermöglicht. Allerdings wurde das Potenzial dieser Technik für den Nachweis von NP im Gewebe bisher nicht ausreichend untersucht. Im Rahmen dieser Arbeit wird daher eine geeignete ToF-SIMS-Methode für die Analyse von oxidischen NP in Lungengewebeschnitten etabliert und optimiert. Die Eignung der ToF-SIMS für die erfolgreiche Erkennung von NP in biologischem Gewebe wird durch Korrelationen und Kreuzvalidierungen von ToF-SIMS-Daten mit den Ergebnissen von Referenztechniken demonstriert.

In dieser Arbeit werden Ratten-Lungengewebeschnitte, welche unterschiedliche Typen von NP enthalten mit ToF-SIMS und Referenztechniken analysiert und die Ergebnisse gegenübergestellt. Paramagnetische Fe_2O_3/SiO_2 (core/shell) NP mit einer Primärpartikelgröße von 10-20 nm (Aggregatgröße von 190 ± 20 nm) werden sowohl mit Hilfe von Hellfeld- und Dunkelfeldmikroskopie als auch mit ToF-SIMS untersucht. Die Signale der unterschiedlichen Techniken zeigen eine extrem ähnliche Lateralverteilung der Signale. Die Verteilung zeigt, dass die Partikel sich zumeist an den alveolaren Wänden und nur zu sehr geringen Anteilen innerhalb von Zellen wiederfinden. Die Kolokalisation der $^{56}Fe^+$ und $^{28}Si^+$ Signale bestätigt die Stabilität der Fe/Si Core/Shell-Struktur auch im Gewebe. Die Phosphocholin-Kopfgruppe $C_5H_{15}NPO_4^+$ liegt kolokalisiert mit dem Gewebesignal CH_4N^+ aber nicht mit den NP vor. Dies legt die These nahe, dass Phospholipide unter den gegebenen Bedingungen nicht an die NP adsorbieren.

Die Verteilung von Fluoreszenzmarkierten SiO_2 NP (25 nm) im Lungengewebe der Ratte kann durch die Verwendung von Fluoreszenzmikroskopie und ToF-SIMS aufgeklärt werden. Beide Techniken zeigen extrem ähnliche Lateralverteilungen von Fluoreszenzsignalen und ToF-SIMS SiO_3^- Signalen. Zudem können weitere ToF-SIMS Signalverteilungen von z.B. Protein (CN^-) und Phosphat-basierten Signalen der Partikelverteilung zugeordnet werden.

Weiterhin wurden Rattenlungengewebeschnitte mit inhomogener Beladung von CeO_2 NP (10-200 nm) nacheinander mit Mikroröntgenfluoreszenzanalyse (μ-XRF) und ToF-SIMS untersucht. Dieser Ansatz ermöglicht eine relativ schnelle Untersuchung des gesamten Gewebeschnittes auf erhöhte Ce-Level. Trotz der Lateralauflösung von 25 μm eignet sich diese Technik zur Auswahl von Untersuchungsbereichen für die folgende hochauflösende ToF-SIMS Analyse (Lateralauflösung 670 nm). Die Lateralverteilung diverser Ce-haltiger Spezies (z. B. $^{140}Ce^+$, $^{140}CeO^+$, $^{140}CeO_2^+$) zeigen insbesondere in der Nähe von Gewebe-spezifischen Signalen (K_2CN^+) hohe Intensitäten. Die erreichte Massenauflösung der ToF-SIMS liegt hier bei ca. $R = 4000$. Neben der Voranalyse von Gewebeschnitten zur Auswahl relevanter Nanopartikel-haltiger Bereiche können die Signale der μ-XRF auch für eine grobe Kreuzvalidierung der ToF-SIMS Ergebnisse dienen.

ZrO_2 Nanopartikel mit Primärpartikelgrößen von 9-10 nm wurden sowohl von ToF-SIMS als auch von der Ionenstrahlmikroskopie (IBM) in Form von Agglomeraten in der Nähe in phagozytischen Zellen detektiert. Dabei wurden Lateralauflösungen von 400-600 nm für die ToF-SIMS und 1000 nm für die Ionenstrahlmikroskopie erreicht. Es wurden nur geringe Mengen von Nanopartikeln im Lungenepithel detektiert. Neben den Nanopartikelsignalen (Zr; ZrO^+ in ToF-SIMS) konnten auch die Verteilungen der S- und P-Signale der IBM mit der ToF-SIMS in Form von SO_2^+ und PO^+ abgeglichen werden. Diese Kreuzvalidierung mit zwei Methoden erlaubt eine sehr hohe Sicherheit bei der Zuordnung der Signale. Mit der ToF-SIMS wurden zudem weitere Signalverteilungen gefunden, welche auf die Verteilung von bestimmten Verbindungen wie z.B. Phospholipiden ($C_4H_8N^+$, $C_6H_{12}N^+$, $C_5H_{15}NPO_4^+$) oder Aminosäuren (K_2CN^+, $C_2H_6N^+$, $C_3H_8N^+$) hindeuten. Dabei konnten Massenauflösungen von bis zu 9000 erreicht werden.

Zusammenfassend kann gesagt werden, dass verschiedene oxidische Nanopartikeltypen mit Größen von 9 nm bis zu mehr als 200 nm mit der ToF-SIMS ohne die Notwendigkeit von Markern im Lungengewebe von Ratten nachgewiesen werden können. Diese Ergebnisse werden durch unabhängige Techniken, wie Hell- und Dunkelfeldmikroskopie, μ-

XRF und IBM bestätigt. Die vorgestellten ToF-SIMS-Analysen zeigen die Verteilung von Nanopartikeln mit einer sehr hohen Zuverlässigkeit und liefern zudem weitere Informationen über die Verteilung von anderen Elementen und Molekülen in der Umgebung der Nanopartikel (z.B. Aminosäuren oder Lipide). Lateralauflösungen von 400 nm und Massenauflösungen von bis zu 9000 zusammen mit der Fähigkeit der simultanen Erfassung von organischen und anorganischen Signale über den gesamten Massenbereich sind einzigartige Eigenschaften, welche das große Potential der ToF-SIMS für die Detektion von Nanopartikeln in Geweben hervorheben. Diese Ergebnisse legen den Grundstein für weitere zukünftige nanotoxikologische Studien zum Verbleib von Nanomaterialien im Körper von Säugetieren.

Table of Contents

Chapter 1

Introduction

1. Introduction

Nanoparticles (NP) are defined as particles with sizes between 1-100 nm in all three dimensions in space.[1] Due to their small volume and large surface area NP have properties (*e.g.* catalytic activity, optical features) often superior to those of the bulk materials.[2, 3] Therefore, they are increasingly used in a variety of applications in research, in production, and for commercial end products, such as drug carriers, functional clothing, cosmetics, energy conversion, and food packaging.[4-10] The growing use of nanoparticles is accompanied by the risk of emission into the environment and an exposition to living organisms. Several toxic effects were observed for nanoparticles administered intratrachelly (*e.g.* 23.5 nm CuO) and gastrointestinally (*e.g.* 58 nm ZnO) to rodents in earlier studies.[11-13] As nanoparticles stay airborne for a much longer time than larger particles due to their small size, the risk of inhaling NP is particularly high.[4, 14] Consequently, inhalation is one of the most important exposition pathways for nanoparticles to enter the body and the lung is the most relevant organ for particle uptake via inhalation.[14-16] Upon inhalation, extraneous particles are deposited along the respiratory airways depending on their size.[17, 18] Larger particles often are deposited earlier in and around the major bronchioles. Due to their small sizes, nanomaterials often reach the end of the respiratory pathway: the alveoli. Upon deposition, the internal lung clearance mechanisms are activated and the materials are supposed to be removed from the lung.[15, 19] However, for small particles an internalization of the particles along with toxic reactions is conceivable.[20-22] The analysis of the deposition and clearance process is therefore a major topic of toxicological research.[23, 24] Due to the small size of the particles powerful analytical techniques are required to enlighten these processes. The commonly used techniques often do not allow high-resolution imaging in conjunction with the identification of organic and inorganic materials or need labelling to identify substances (*e.g.* laser ablation inductively coupled mass spectrometry (LA-ICP-MS),[25] scanning electron microscopy coupled to energy dispersive X-ray spectroscopy (SEM-EDX)[26] or fluorescence microscopy (FM)[27]). Secondary ion mass spectrometry based on a sector-field mass analyzer (*i.e.* dynamic SIMS) provides high-resolution imaging, but only has a low number of detection channels and is therefore not suited for untargeted analysis of unknown samples.[28]

The combination of high lateral resolution along with the detection of both, particle and biological matter without labelling is desired.[5, 29] Furthermore, high sensitivity is necessary to detect low amounts of particle material.

Time-of-Flight secondary ion mass spectrometry (ToF-SIMS) is a promising technique for toxicological studies.[30] It allows the detection of inorganic and organic, atomic and molecular ions from surfaces with a high sensitivity.[31-33] Due to this feature and due to its 3D-imaging capabilities this technique is frequently used for the detection and localization of anomalies, defects or features in a variety of analytical questions.[34-38] With spatial resolution in the nanometre range and the simultaneous detection of ions from the complete mass range, the use of this technique for nanomaterial detection within tissues is promising.

Although the figures of merit for ToF-SIMS are promising, the detection capabilities of this technique for nanomaterials in biological tissue are hardly explored. The reasons are the low amounts of available material present in the nanoparticles and the accompanying limitations in data acquisition and evaluation (*e.g.* need for high spatial resolution along with sufficient mass resolution, chapter 2).

In this thesis, novel ToF-SIMS methods are developed and optimized to evaluate whether or not ToF-SIMS can be used to study the distribution of nanoparticles in lung tissue sections. The results are carefully compared and validated with dark-field microscopy (DFM), fluorescence microscopy (FM), micro X-ray fluorescence spectroscopy (µ-XRF) and ion beam microscopy (IBM).

Chapter 2

Scope of the Thesis

2. Scope of the Thesis

The goal of this thesis is the **sensitive** and **reliable** detection of nanoparticles within lung tissue sections **without the need for markers** or labelling at simultaneously **high lateral resolution** and **mass resolution** by ToF-SIMS.

These challenges with respect to **sensitivity** derive from the low amount of material available in a single nanoparticle. Strategies for an optimal ionisation and detection have to be applied. The low amount of material present in nanoparticles is also challenging in terms of **reliability**: typical peak patterns (*e.g.* isotopic peak patterns) are not detectable. Furthermore, the low signal-to-noise ratio makes an unambiguous detection difficult. A **marker-free** detection is an important goal in toxicology in order to avoid artefacts induced by the marker. However, ensuring a sensitive and reliable detection of nanoparticles without the assistances of markers is difficult. Finally, a simultaneous optimization of **mass resolution** as well as **lateral resolution** is challenging when applying ToF-SIMS. A high mass resolution is a precondition for the reliable and sensitive detection of nanoparticles discussed before. However, in order to achieve information in the tissue on a cellular level, a high lateral resolution is an indispensable requirement.

In the first part of this thesis, the individual challenges are elucidated and the strategies to overcome them are explained. In detail, the technology of ToF-SIMS is explained considering the aspects of sensitivity, mass resolution, lateral resolution and marker freeness (chapter 3.1). With respect to increasing the reliability of the ToF-SIMS data a number of techniques such as conventional light microscopy techniques, fluorescence microscopy, micro X-ray fluorescence spectroscopy (µ-XRF) and ion beam microscopy (IBM) are applied to the samples. Therefore, basic concepts of these techniques are explained in chapter 3.2. A brief consideration on the analysed nanoparticle species (chapter 3.3) and the targeted tissue (chapter 3.4) highlights the requirements in terms of the challenges **sensitivity**, **reliability**, **marker-freeness**, **high mass resolution**, and **high lateral resolution**. Finally, the state-of-the-art with respect to nanoparticle detection in tissue by secondary ion mass spectrometry (SIMS) is given in order to allow an assessment of the results of this thesis (chapter 4).

In a second part of this thesis, nanomaterial-specific ToF-SIMS methods are carefully developed and optimized to be able to detect different types of NPs in lung tissue (chapter

5-8). In each study, custom ToF-SIMS measurement strategies are combined with other analytical techniques in order to achieve the detection and identification of NP in lung tissue slides. In chapter 5, optical microscopy is applied to samples containing rather large (220 nm) Fe/Si core/shell nanoparticles. In order to show the potential of ToF-SIMS (*i.e.* sensitivity), smaller NP are in the focus of a second study (chapter 6). A marker-based detection of smaller (28 nm) SiO_2FITC particles is presented in comparison to fluorescence microscopy. Without the aid of a marker the detection and identification of rather large (155 nm) CeO_2 nanoparticles by ToF-SIMS as well as μ-XRF is demonstrated (chapter 7). Finally, the marker free detection and identification of smaller ZrO_2 nanoparticles (70-80 nm) by IBM and ToF-SIMS is discussed in chapter 8.

A summarizing conclusion (chapter 9) highlights the achievements with respect to the goal of the thesis and the individual challenges and gives future perspectives for further developments of ToF-SIMS analyses in the field.

Chapter 3

Fundamentals

3. Fundamentals

3.1 ToF-SIMS

In this chapter, the general principle of ToF-SIMS is briefly described (chapter 3.1.1), followed by a description of the individual instrumental components (chapter 3.1.2). Afterwards, the operational modes are described (chapter 3.1.3) and the basic data evaluation strategies are presented along with typical examples of analytical questions (chapter 3.1.5). Based on this overview the operational parameters are explained (chapter 3.1.5).

The description of the components, operational modes and data evaluation are focusing on the IONTOF TOF.SIMS^5 instrument and the software (Surface Lab 6.7) used in this thesis. Therefore, they do not necessarily display the setup for instruments of other manufacturers.

3.1.1 The Principle of ToF-SIMS

3.1.1.1 Principle

In ToF-SIMS secondary ions are formed when primary ions hit a surface. The induced collision cascade leads to the emission of particles, neutral atoms, electrons as well as positively and negatively charged ions (“secondary ions”). The mass separation and the detection of the secondary ions is performed by a Time-of-Flight mass analyzer. Ions are extracted from the sample surface by an electric field and are separated in a field-free drift tube. The detection of the ions is facilitated by a multi-stage detector system. The ToF detection chain enables the sequential detection of all ion species of the same polarity formed in the collision cascade.

3.1.1.2 Sputtering

The exact secondary ion formation process is still a matter of research and not yet completely understood. However, several models explain parts of the sputtering and ionization process.

The base of the formation of secondary ions is the sputtering process. In this process, a surface is bombarded with a high energy ion beam, which leads to the emission of electrons, atoms and ions as well as neutral and charged clusters. Only a fraction of 10^{-6}-10^{-1} of the emitted species is positively or negatively charged and available for detection by ToF-SIMS[39]. The linear cascade theory by P. Sigmund describes the sputtering process[40]: The interaction of a single ion with a surface is envisioned to induce a cascade of collisions. The energy of the impinging ion is transferred to the atoms in the surface by these collisions. If the impetus energy returns to the surface in the course of the cascade, the emission of neutral and charged species can occur. After losing most of its energy, the primary ion is deposited in the material.

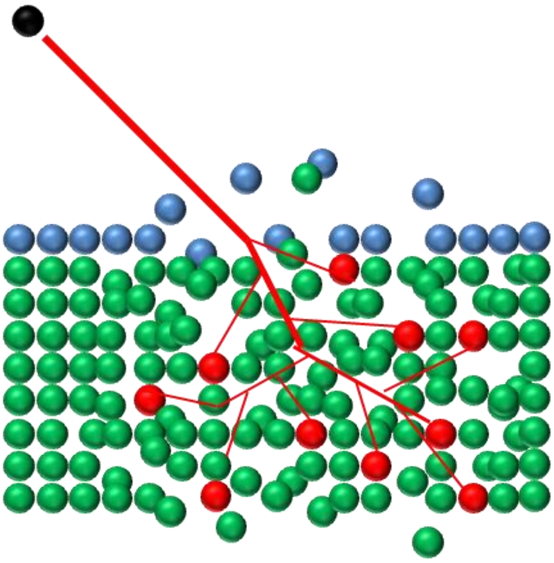

Figure 3-1: Graphical representation of the SIMS collision cascade process upon impact of a primary ion (black). The blue balls represent atoms from the topmost surface. The green balls represent the sub-surface layers of the sample. The red grey balls represent atoms, which were directly hit and displaced by the recoils (adapted from [41] with permission from The Royal Society of Chemistry).

Figure 3-1 shows a schematic representation of the collision cascade for the impact of a monoatomic ion (black) onto a sample. Individual atoms within a hypothetical section of a sample are shown. The outermost atomic layer is marked in blue colour. On its trajectory, the ion (black) impacts onto the surface displacing surface atoms (blue) and subsurface atoms (green). Atoms that were directly hit and displaced are coloured in red. These are called "primary recoils". Atoms hit by further recoils are referred to as "secondary recoils". The secondary recoils transport the major part of the energy in the cascade. The cascade of the collisions evokes compositional changes in the surface and in the deeper internal structure. Although only a small area is directly hit, the influence extends into the depth of the sample (*e.g.* implantation depth of 10.1 nm for 25 keV Bi_3^+ in trehalose films[42]) and thus affects a considerable volume of the sample. As a consequence, amorphization of inorganic samples and destruction of the sample integrity of inorganic sample are induced. Furthermore, the emission of species mainly from the top layers is observed.

The model shown in Figure 3-1 neglects the existence of bonds between the individual atoms. Considering the impact on the molecular structure it has to be pointed out that an ion with an energy in the keV range can destroy any molecular bond even after several collisions. As a consequence, the impact of a high energy ion induces an alteration of the sample's integrity (*e.g.* crystal structure, molecular composition, *etc.*) in a region of several nanometres around the trajectory.[43]

A relatively new development in the field are polyatomic primary ions. Examples are *e.g.* C_{60} sources, and Au or Bi ion sources, which form Au_x^+ (x = 1-5) or Bi_y^+ (y = 1-7), respectively. Their effects are not yet fully understood and no comprehensive theory is known. Due to the higher mass and volume, the impact area is expected to be larger for polyatomic ions compared to monoatomic ions[44, 45]. However, the clusters are expected to fall apart upon impact and the impact energy per atom is lower. Consequently, the penetration depth of the collision cascade is shallower. The impact of polyatomic primary ions leads to non-linear emission effects with much higher secondary ion yields per impacting ion. Furthermore, the damaging effects are reduced.[43]

Before the polyatomic primary ions were developed, the only way to achieve information on molecules and fragments thereof was the use of the so-called "static SIMS":

As the atomic as well as the molecular structure in the volume is affected by an impacting primary ion, the sample surface would not resemble the initial state upon a second impact. In consequence, for molecular analysis the number of ions impinging a surface area has to be limited. The term "static SIMS" relates to analyses, in which the probability to hit a spot more than once during the course of the ToF-SIMS analysis is low.[46] The surface area damaged by a single ion is known as the disappearance cross section (σ). For static conditions the ion dose applied to a defined area (primary-ion-dose density, PIDD) has to comply with the following equation 1 to keep the surface damage low[47]:

$$\boldsymbol{PIDD \ll \frac{1}{\sigma}} \qquad (1)$$

In practice this most often means that no more than 1% of a surface is damaged (which relates to a dose of less than 10^{12}-10^{13} primary ions/cm²). As a result, static SIMS can be safely used for the analysis of molecular monolayers.

For dynamic SIMS, as opposed to "static SIMS", the applied primary ion dose density is sufficiently high, in such way that a single spot statistically is hit more than once and a significant erosion of the surface can take place. As a result, the relation of PIDD and disappearance cross section σ is as follows:

$$\boldsymbol{PIDD > \frac{1}{\sigma}} \qquad (2)$$

In this study, the detection of nanomaterials in tissues is the goal. Not only the surface composition but the depth composition is of interest (see chapter 3.1.3.3). Consequently, a gradual removal of the surface is necessary to analyze the samples up to a significant depth of several micrometers and detect the NP with a good sensitivity. As a result, the PIDD applied to the surface is significantly higher than 10^{13} primary ions/cm² often exceeding 10^{15} ions/cm².

3.1.1.3 Models of Ionization in ToF-SIMS

Several models were developed to explain the ion formation in ToF-SIMS. They are based on different physical models (*e.g.* thermodynamic[48], quantum mechanical[49], empirical[50]). However, all models are only valid for specific conditions. Briefly the *bond breaking model*, the *Plog model*, the *precursor model* and the *desorption ionization model* explaining the ionization for inorganic and organic species are described within this chapter. Since the nanoparticles used in this thesis are based on metal oxides, the ionization process can be explained best by models for the inorganic oxides.

The *bond breaking model* suggests the presence of “preformed” ions (A^+B^-) in polarized oxides or salts existing in the solid. Upon sputtering, these are emitted as neutrals (A and B) or ions (A^+ and B^-) depending on their distance to the surface and the potential energy levels in the ionic and neutral states.[51]

The *Plog model* assumes an emission of neutral species for the formation of polyatomic ions. These neutral species are converted into ions, if their internal energy is high enough to dissociate into ions upon minimal fragmentation within a sufficient distance to the electronic influence of the surface.[52]

Both of these models are supported by experimental data, which mostly favours the emission of diatomic species with a subsequent bond cleavage. However, the direct emission of atomic species as well as oxide species with subsequent ionization upon bond cleavage also contributes to the ionization processes. The final result is a separation into charged ions and/or electrons. The summarizing ionization concept is called the *nascent ion molecule* concept.[43, 53]

For the ionization of organic molecules different models are required. Benninghoven suggested the *precursor model* for the ionization of organic molecules from clean metal surfaces. In this model “preformed” molecular ions such as *e.g.* $[M+H]^+$ and $[M-H]^-$ (precursors) are assumed to be present on the surface and are emitted upon transfer of sufficient energy. The cascade mechanism evoked on the impact of a primary ion induces an energy gradient on the surface around the impact point. Molecules in the central area experience a high energy returning to the surface after the impact and are destroyed or fragmented and emitted as atomic species. At the edge of the excited area, the energy returning to the surface is not sufficient to exceed the intermolecular forces in the surface layer (*i.e.* the surface binding energy). In consequence, no emission takes place. However, between both of the extremes the returned energy is sufficient to overcome the surface binding energy (intermolecular forces) but not cause fragmentation to the molecules (*i.e.* exceed the intramolecular forces). As a result, the preformed molecular ions are emitted. Fragments of the molecules are emitted closer to the centre of impact, where the energy is high enough to overcome intermolecular as well as intramolecular forces. The assumptions of the model are in good agreement with experimental results.[43, 54, 55]

In the *desorption ionization model* the energy from the ion impact leads to the excitation of vibrational states of molecules or clusters. The similarity of the spectra from SIMS, fast atom bombardment, laser and plasma desorption ionization leads to the conclusion that the initial energy deposition is not relevant. In this model the desorption and ionization events are separate in time and space. The desorption is a fundamentally vibrational or thermal process. Pre-formed ions (*e.g.* A^+B^-) are emitted directly in the ionized state. The ionization of other molecules is supposed to take place in the gas phase at the edge of the top surface layer by ion/molecule reactions or electron ionization. Furthermore, in the vacuum phase unimolecular dissociations due to the internal energy may lead to the formation of fragment molecular ions.[43, 46, 56]

With respect to the topic of this thesis it is to question, which model is suited best to describe the scenario on the surface of a nanoparticle-containing tissue section. On the on hand, the ionization of the inorganic nanoparticles is explained by the *nascent ion molecule* concept, whereas on the other hand, the ionization of the organic molecules should be described by the *precursor model* or the *desorption ionization model*. However, both models are derived from experiments with monoatomic primary ions and therefore can only be regarded as approximate guidelines for the polyatomic SIMS experiments in this thesis.

3.1.1.4 Quantitative Measurements

Quantitative analyses of compounds in samples by ToF-SIMS is a major challenge as will be explained in this section.

The equation 3 below illustrates the basic relation between the secondary ion yield and several influential factors for elemental ions generated from a metal sample for dynamic SIMS experiments. However, as the theories for polyatomic primary ion bombardment are not yet sufficiently developed, the equation, which is strictly only valid for monoatomic primary ions, is used to demonstrate the basic relations:

$$\boldsymbol{I_m = I_p Y_m \alpha^+ \theta_m \eta} \qquad (3)$$

The secondary ion current I_m of the species m depends on the flux of primary particles hitting the surface (I_p). The sputter yield (Y_m) and the positive ionization probability (α^+) influence the number of emitted positively charged species from a primary ion collision. θ_m represents the fractional coefficient of the (chemical) species m in the analyzed surface layer. Furthermore, the transmission of the analytical system (η) limits the number of detected species.[46]

However, several further influencing factors have to be considered for static SIMS experiments as well as for the quantification of organic species:

Physical parameters like crystallinity of the target surface, the topography and the mean atomic numbers in the sample influence the sputter yield. Additionally, preferential sputtering and ion beam induced mixing both can influence the sputter yields.[43]

The ionization probability is a major factor influencing the formation of secondary ions as it varies over several orders of magnitude for different species. In this respect, the nature and the extent of the electronic interactions of the desorbing species and the surface play an important role. Depending on the surface composition, the formation of a certain ion species can be strongly enhanced or suppressed. Differences in the secondary ion yields of the positively charged metal ion (Me^+) of several orders of magnitude are usually observed for the case of clean metal surfaces *vs.* the oxidized metals. Furthermore, the presence of one substance in the vicinity of another substance can influence the secondary ion yields. These so called matrix effects leads to the inherently difficult quantification of ToF-SIMS results.[46] Most often the surface composition is not known or even altered during the analysis *e.g.* by adsorption of species from the residual gas. Especially for samples of unknown surface composition/oxidation states an estimation of the ionization probability is challenging.

Furthermore, the disappearance cross section and the penetration depth of the primary ion are important factors, especially for organic components. The size of the analyzed volume per shot, *i.e.* the diameter and the sampling depth, most often are not known and depend on the substrates. The ionization probabilities are different for ionization from the top layers, or the layer beneath.

The introduction of an internal standard at a defined concentration, which behaves exactly in the same way as the analyte regarding solubility, deposition on substrate, at evaporation of solvent, sputtering and ionization, can enable the quantification of analytes from solutions in ToF-SIMS. However, as these prerequisites are most often only fulfilled for isotopically labelled molecules or structurally similar molecules, this approach is only practical for a limited number of sample systems.[57]

Ion counting statistics might also change the outcome of a quantitative analysis. Whereas for dynamic SIMS several quantification examples are known, for static SIMS quantitative information currently appears achievable only for well-known samples under defined conditions.[43]

3.1.2 The Instrumental Setup

Figure 3-2 shows the general setup of the basic components of a TOF.SIMS[5] instrument. Primary ions are formed in the ion gun. In the ion optical column ion packages are formed and focused onto the target. A rastering unit guides the ion packages to the desired positions of the sample. The secondary ions generated by the surface bombardment of the primary ion packages are extracted from the sample and enter the drift tube via transport optics. The detection of the secondary ions is facilitated after the mass separation in the drift tube and a reduction of the influence of the kinetic energy spread on the flight time in the reflectron. Charge compensation on the sample surface is conducted by an electron flood gun supplying low energy electrons to the surface in connection with a sophisticated beam timing scheme.[58]

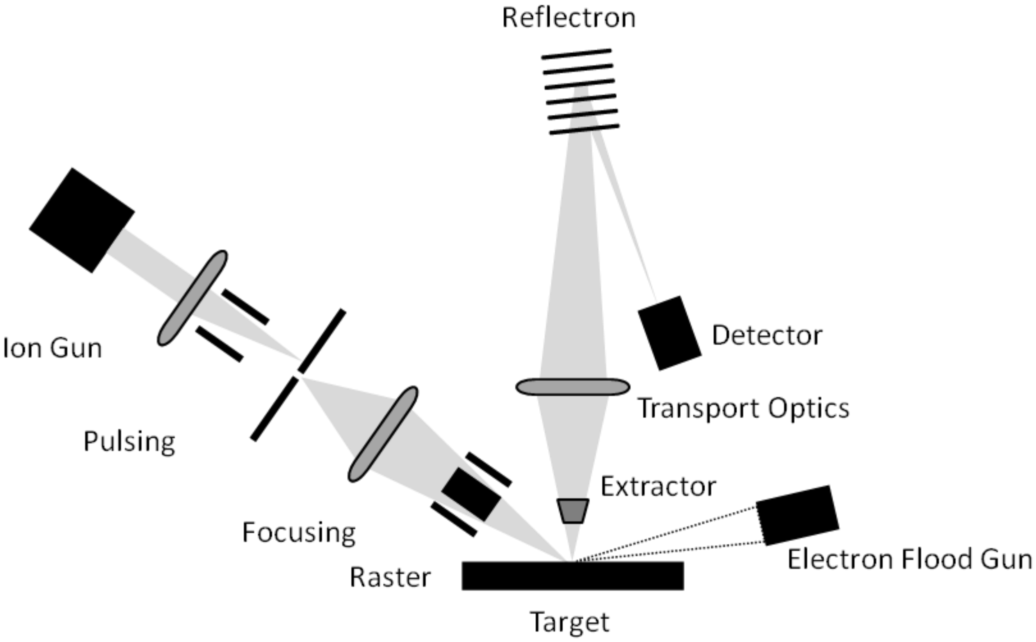

Figure 3-2: Schematic representation of the ToF-SIMS setup with its basic components. The primary ions are generated in the ion gun and directed onto the target. Secondary ions emerging from the impact are extracted into the analyzer and are separated according to their mass-to-charge ratio (*m/z*). The reflectron reduces kinetic energy differences and directs the ions onto the detector. An electron flood gun can be used to neutralize sample charging (adapted from[59] with permission from ION-TOF GmbH).

3.1.2.1 Analysis and Sputter Gun

The bombardment of the sample with ions during analysis and sputtering is performed by ion guns. The requirements for both types of guns are different. The requirements for the *analysis gun* are short pulse widths to achieve a precisely defined starting time for narrow signals in the spectra, a sufficient intensity to reach high secondary ion currents in reasonable time and a high lateral resolution to allow high-resolution imaging of the individual distributions of the components in the sample.

Sputter ion guns require high currents to achieve high erosion rates of the sample. The choice of the sputter ion can influence the secondary ion yields of species on the sample by supporting the formation of electropositive or electronegative ion species via the use of oxygen or caesium ions, respectively. Moreover, the impact behaviour of sputter ions critically defines the detection of organic molecules and the achievable depth resolution. It was found that large cluster ions can increase the secondary ion yields in some cases and offer the possibility for molecular depth profiling, which was not possible earlier due to the extensive fragmentation of organic molecules.

In the following the basic concepts for ion generation in the analysis and sputter ion guns used in this thesis are explained. Furthermore, the additional necessary steps for the treatment of the analysis beam are described.

Ion Generation

Different technical solutions for the generation of ions are available. The requirements for an *analysis gun* are nowadays met by a liquid metal ion gun (***LMIG)***. Most often electron impact ionization guns (***EI)*** or thermal ionization (***TI***) guns are used as sputter guns, because they allow to influence the matrix *e.g.* oxidation or deposition of Cs (compare 3.1.5.3). For organic depth profiling a specially modified version of the EI gun is used: The gas cluster ion beam gun (***GCIB)*** produces large gas cluster ions from gases.

LMIGs are advantageous as *analysis guns*. These sources have a high brightness, which allows high lateral resolution along with sufficient ion currents at short pulse widths. In LMIGs a metal heated to liquidity is flowing around the tip of a needle with a high potential applied (Figure 3-3A). For this purpose, a reservoir and the needle are welded to the heating filament. In the case of bismuth, as used in this study, the metal is alloyed to reduce the melting temperatures. The applied high potential leads to a strong electrostatic force inducing the formation of a Taylor cone. The result is the emission of ions from the nanometre sized apex of the cone. This shows a high brightness, which is ideal for high-resolution imaging applications. However, the total current of these kinds of sources is lower than *e.g.* EI or TI guns[60], which are described below. LMIGs offer monoatomic primary ions as well as relatively small polyatomic cluster ions. The traditionally used Ga^+ and In^+ LMIGs were replaced by further developments introducing the Au_n^+ and Bi_n^+ ion guns[61-64].

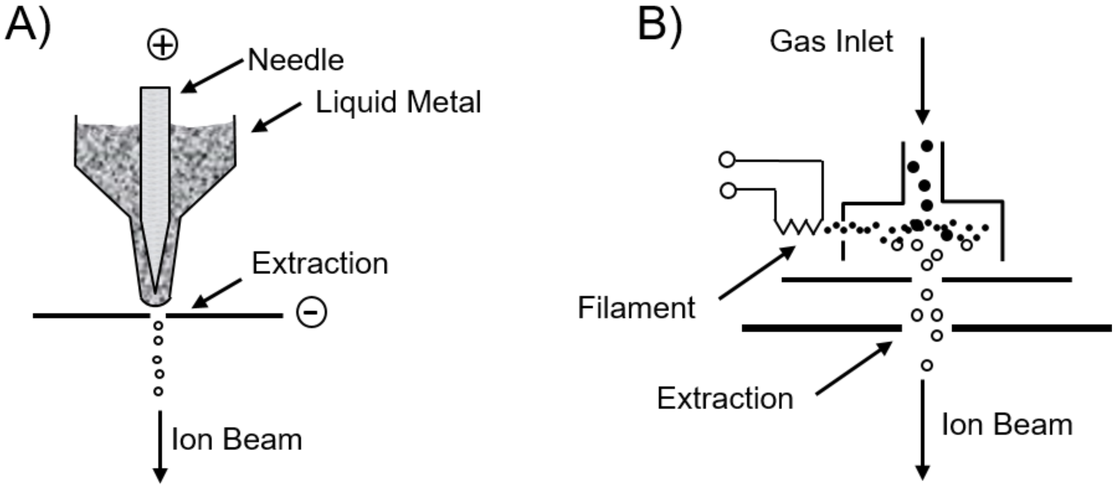

Figure 3-3: Schematic representation of primary ion guns. A) The liquid metal ion gun (LMIG) is used as the analysis gun in this thesis. (adapted from [65] with permission from Elsevier. B) The electron ionization source (EI) source is used for sputtering with oxygen to increase the yield for electropositive species (adapted from [66] with permission from the authors).

O_2 sputter ion beams are frequently used for depth profiling because they enhance the yield for electropositive species in the samples by supplying oxygen to the sample surface[67]. These ion beams can be formed by an ***electron impact ion source*** (Figure 3-3B). The gas is ionized in an ionization chamber by collisions with electrons produced from a filament. The impact of the electrons leads to the production of positively charged cations (*e.g.* O_2^+). This source inherently has a low brightness along with low focus ability because the ions are formed in a larger volume. However, electron impact ion sources are very robust and easy on maintenance. Along with the possibility to use different kinds of gases (*e.g.* to influence the ionization behaviour), this aspect makes these sources versatile tools.[60] An O_2 EI ion gun is used in this work for sputtering of lung tissue in the positive polarity in chapters 5, 7 and 8.

Ar GCIBs have relatively low energies per atom and are therefore a relatively soft erosion technique. Their impact inflicts less fragmentation to molecular species in the surface layer and in the layer beneath the top layer compared to monoatomic ion beams[68]. GCIBs based on large clusters (n > 100) of Ar or other gases allow organic depth profiling and were introduced to the analysis of biological species reducing the amount of fragmentation to organic molecules.[69] Ion formation in GCIBs can be based on the previously mentioned EI sources with some modifications. Ar-clusters are fed into the EI ionization chamber instead of the usual gas supply (Figure 3-4A). However, an additional step before ionization is necessary to form the gas clusters. Highly pressurized gas (~20 bar) is guided into an evacuated nozzle, which leads to an adiabatic expansion of the gas stream. Consequently, the Argon atoms are cooled down travelling at supersonic speeds. Argon atoms with the same trajectories form Ar_x^{n+} clusters with x = 1 - 160,000 and n = 1-30 with significant intensities depending on the initial gas pressure and ionization conditions[70-72], depending on the ionization conditions. A skimmer aperture only lets clusters with the right direction and size pass into the ionization chamber.[60] A ToF mass-filter enables the selection of the desired Ar_x species. This type of ion gun is used in this work for sputtering when also the detection of organic information is desired (chapter 8.3.3).

Cs sputtering favours the formation of electronegative secondary ion species and can be used to reduce the influence of matrix effects[73]. It can be employed by the use of a ***thermal ionization source*** (Figure 3-4B). In this kind of ion source vaporized Cs is fed into a tungsten frit, which has a higher work function than the ionization potential of the Cs. Consequently, an applied potential leads to the formation of positively charged Cs^+ ions. These sources deliver high currents. However, due to the large diameter of the frit (1-2 mm), the brightness is limited.[60] This type of ion gun is used in this work for sputtering of SiO_2 NP-containing lung tissue in chapter 6.

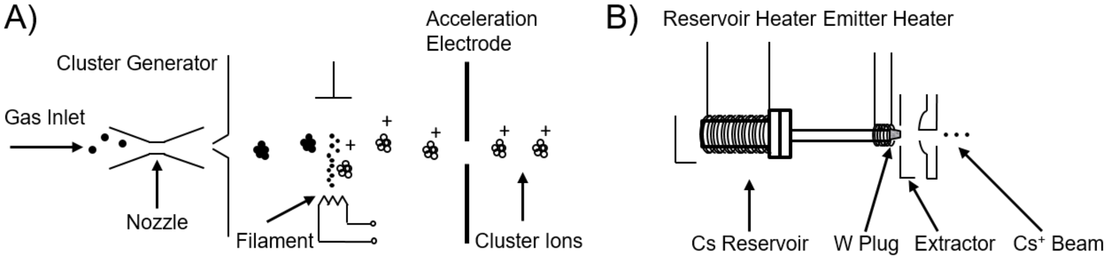

Figure 3-4: Schematic representation of two types of sputter guns. A) The gas cluster ion beam gun (GCIB) provides a gas cluster ions for organic depth profiling. (adapted from [70] with permission from John Wiley and Sons) B) The thermal ionization gun (TI) is used for sputtering with Cs to increase the yield of electronegative species (adapted from [66] with permission from the American Chemical Society).

Pulsing, Mass Separation and Bunching

The analysis primary ion beam needs to have a defined starting point for the determination of the flight time of the secondary ions in the used instruments.[60] Furthermore, the primary ion guns most often form a variety of ionic species including clusters and species with multiple charges. To ensure that only a single kind of projectile is used to excite the surface, a section (pulse) is cut out from the continuous ion beam by a pre-chopper pulsing system. The different ion species within the cut section have the same kinetic energy but different velocities and are therefore separated by their flight time while travelling down the ion column. At a second pulsing stage further down the column a chopper exclusively lets the desired ion species pass.[64]

For best mass resolution, it is mandatory to have a precisely defined starting time for all ions. Furthermore, the length of the impacting primary ion pulse should be as short as possible. However, at the same time the number of ions impinging the surface (*i.e.* ion current) should not be reduced. Thus, simply shortening of the ion pulse is not reasonable, since it would lead to longer analysis times. To overcome this challenge a relatively long ion pulse (several ns) is guided into a buncher, where a transient electric field is switched on to compress the ion pulse. The width of the ion pulse reaches the sub-nanosecond range by accelerating the rear ions and reducing the temporal expansion of the ion pulse.[74] Consequently the ions arrive at the sample in a very short time window, which defines an exact starting point and provides a very good mass resolution. Additionally, this measure ensures that a high number of primary ions (*i.e.* higher ion current) can be used for the analysis. However, the kinetic energy spread within the ion pulse is increased by the "bunching" and thus the achievable lateral resolution is limited to several micrometers[75]. The reason is the different beam deflection of ion packages with different kinetic energies within focusing lenses (chromatic aberration). One option to achieve a high mass resolution along with a high lateral resolution is the Burst analysis mode, in which the sample is bombarded with a number of successive, extremely short primary ion pulses within a single extraction cycle. Therefore, the resulting spectra show multiplets of every peak, which can be deconvoluted by the software. However, the number of primary ions per shot (primary ion current) is much lower. In consequence, the analysis times to acquire signals of sufficient intensities are much longer due to the short pulses.[76]

Alternatively, the delayed extraction mode can be used to decouple the width of the primary ion pulse and the mass resolution thereby enabling a good mass resolution at moderate primary ion currents (compare chapter 3.1.5.5).

3.1.2.2 Analyzer

The ToF-analysis consists of three steps: The extraction, the separation and the detection of the secondary ions. In brief, the secondary ions are extracted by an extractor electrode and are pulled into the drift tube. They travel through this field-free drift tube and are detected by a multi-stage (channelplate-scintillator-photomultiplier) conversion detector.

Extraction

After the secondary ions are formed, they are extracted from their emission volume by an extraction field into the field-free drift path of the analyser. The applied extraction field is typically switched on shortly before the primary ion pulse hits the surface and stays on until it is ensured that the available secondary ions of the selected polarity have left the extraction volume towards the detector (Figure 3-5). This ensures that the maximum number of available ions is extracted especially for short ion pulses (bunched ion packages) and smooth samples.[77]

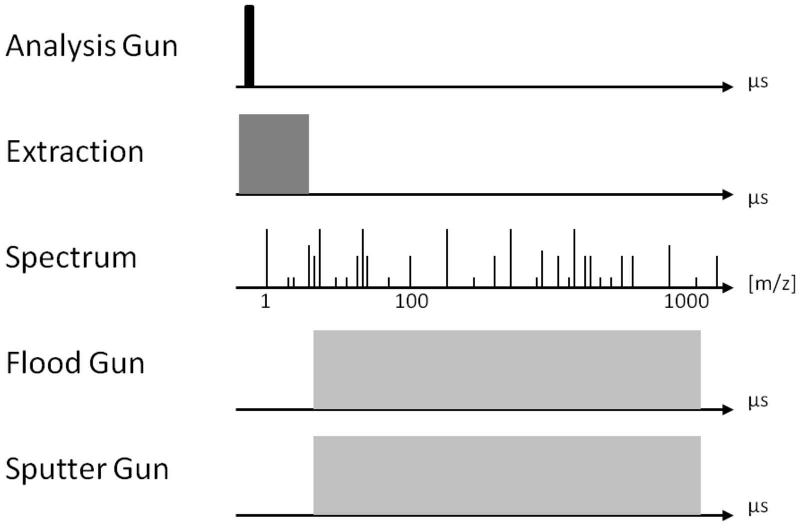

Figure 3-5: Schematic representation of the extraction timing for a depth profiling analysis using the interlaced sputtering mode. The extraction field is switched on before the primary ion pulse from the analysis gun hits the surface and stays on until the secondary ions are extracted from the sample. The spectrum is acquired starting with the first ions arriving the detector. While the secondary ions are on their way through the drift tube, the flood gun and sputter gun can be used to neutralize or erode the sample surface (adapted from[77]).

However, for imaging analysis with longer ion pulses (buncher switched off) or topographically challenging samples (*e.g.* spherical objects) a delayed extraction mode can be used to maintain a reasonable mass resolution. This mode enables a short free drift time of the formed secondary ions directly after the primary ion impact.[78] By this the width of the primary ion pulse is decoupled from the mass resolution, because all ions are pulled into the analyzer at the same time after a short delay resulting in a narrow starting time spread. This enables an analysis with good mass resolution along with high lateral resolution and reasonable ion currents. It enables a superior signal separation and a reliable identification due to its routine mass resolution of about $R = m/\Delta m = 3000$ compared to the unity mass resolution of the standard imaging modes. However, some of the low *m/z* ions might be not detected due to their initially higher kinetic energy and thereby faster disappearance from the extraction volume influencing the quantitative information.[79] Although this mode provides a good mass resolution, an unambiguous identification based solely on the mass-to-charge ratio (*m/z*) might be challenging for signals of low intensities, due to the high number of background/interfering signals. Therefore, the assignments of observed low intensity *m/z* of the desired species can be confirmed by an analysis on the same sample in a high mass resolution mode, if necessary.

Ion Separation

The ion separation takes place in a field-free drift tube. The secondary ions extracted from the surface enter the drift tube at the same time and are separated according to their velocity. An ion mirror is employed to compensate for small energy differences resulting from the energy spread in the collision cascade (improving mass resolution) and to guide the ions onto the reflector. The principle of the time-of-flight separation and the ion mirror are substantial for this thesis and are therefore explained here in more detail. Further information on the topic can be found in the literature[32, 57, 80]

Since at the extraction all secondary ions are accelerated to the same kinetic energy their flight time is governed only by their *m/z*. Thus, a separation of the ions based on their mass is achieved. The following equations describe the fundamental relation between mass, charge and flight time.

$$\boldsymbol{E_{pot} = q \cdot U = \frac{1}{2} m v^2 = E_{kin}} \qquad (4)$$

The ions with the charge q are accelerated by the electrical field U. In the field-free drift path the kinetic energy of the ions is then equal to their potential energy. The substitution of $v = \frac{s}{t}$ leads to a fundamental ToF mass spectrometry equation:

$$\boldsymbol{m = \frac{2qU}{s^2} \cdot t^2 \Rightarrow \frac{m}{q} = \frac{2U}{s^2} \cdot t^2} \qquad (5)$$

Since the acceleration field U and the flight distance s are known, after measuring the flight time, the mass-to-charge ratio of the ions can be calculated[46].

However, differences in the kinetic energy distribution of secondary ions of the same *m/z* are induced by the nature of the collision cascade (*e.g.* due different numbers of collisions within the surface prior to the emission). To counteract this energy spread and the involved flight time difference, a reflectron reducing the influence of the energy spread of ions of different energies but the same mass is employed within the flight path (Figure 3-6). The reflectron contains an electrode array with increasing potential forming an increasing electrical field of the same polarity as the ions. Therefore, ions with higher kinetic energies penetrate deeper into the reflecting field and are influenced by the field to a higher extent than ions with a lower kinetic energy. In result, the flight time distribution for ions of the same mass is narrowed down and a better mass resolution is achieved.

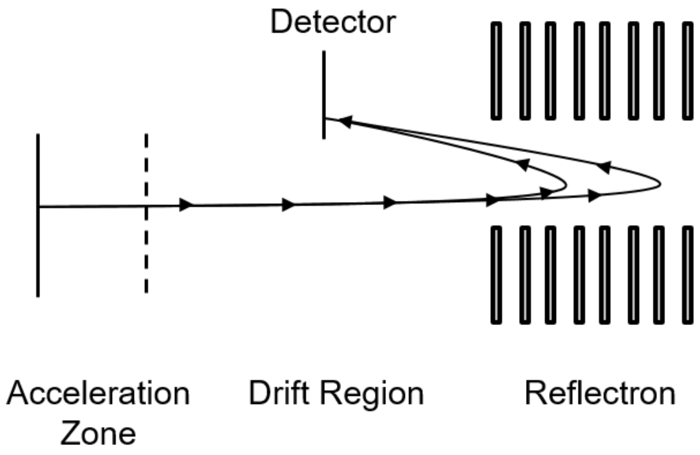

Figure 3-6: Graphical representation of the reflectron principle. Ions with higher kinetic energies travel further into the reflectron and are more influenced by the opposing electric field. Ions of the same *m/z* but slightly different kinetic energies reach the detector at the same time. (adapted from[81] with permission from John Wiley and Sons).

Detector

After leaving the reflectron the ions are directed towards the detector. The detector consists of a multistage conversion unit employing a multichannel plate (MCP), a scintillator and a photomultiplier. The secondary ions hit the MCP, thereby inducing the formation of (primary) electrons. The conversion efficiency of this process is dependent on mass, velocity and charge of the impinging species. To achieve a reliable detection especially for high mass/low velocity ions a post acceleration is applied to all ions prior to impacting the multichannel plate. Once an impacting secondary ion triggers an electron in the multichannel plate, a cascade begins to run: During the collisions of the electron with the walls the number of electrons is multiplied by a factor of 1000 (gain). The electrons reach the scintillator stage and are converted into photons. The photons exit the ultra-high vacuum (UHV) through a vacuum window and are transferred by a light guide to a photomultiplier. Due to this procedure the signal leaves the high vacuum system on the one hand as well as the high voltage system on the other hand. The photons hit the photocathode forming new electrons, which are subsequently amplified by the following dynodes. A sharp current pulse is detected at the anode and a trigger signal is generated.[43, 82] A time-to-digital converter (TDC) assigns the incoming signal with a time scale with 100 ps resolution. Mass spectra are calculated based on these assigned times of arrival. Ideally, every single ion causes a counting event. However, directly after an ion hits the detector a new counting is not possible due to the necessary time it takes the detection system to recover after a counting event (dead time). To limit the influence of this, a Poisson correction of the peak intensities of the data is automatically executed in the software to account for undetected ions where applicable.[74]

3.1.2.3 Charge Compensation

When charged ions hit the sample surface an accumulation of surface charges can occur and disturb the flight time or even inhibit the detection of the secondary ions. The impact of the primary ions leads to the emission of secondary electrons from the surface. As the resulting surface charges are usually positive, a neutralization via electrons is possible. However, these electrons have to be applied in such a manner that no further secondary electrons are emitted from the surface. This is facilitated by an electron flood gun flooding the surface with low-energy (0 - 21 eV) electrons. The low energy electrons are likely to be influenced by the electrical fields of the high voltages in the instrument and therefore an intelligent timing of the flood gun is necessary (Figure 3-5). The charge compensation is especially important for non-conductive samples and after the bombardment of a surface with high current densities (*e.g.* sputter erosion).[83]

3.1.3 Operational Modes

The variety of different modes in ToF-SIMS enables the selection of the desired analytical parameters for the respective question. This makes the ToF-SIMS one of the most versatile analytical techniques for diverse questions with a broad range of applications. The fundamental modes used in everyday analyses are spectrometry, imaging, depth profiling and 3D microarea analysis. The instrumental parameters of these modes are individually optimized with respect to the analytical question, *i.e.* with respect to the lateral resolution, the mass resolution and the depth resolution. The modes are described in the following.

3.1.3.1 Spectrometry

The spectrometry mode in its default configuration uses a bunched primary ion beam and reaches the highest mass resolution of up to $R = \frac{m}{\Delta m} = 10.000$ (compare 3.1.2.1).[84] The lateral resolution is limited to a few micrometers and the typical mass range at a cycle time of 200 µs is $m/z > 2000$ under standard conditions.

3.1.3.2 Imaging Mode

The primary ion beam is rastered across the desired surface with a defined pattern and typical fields-of-view between 10 x 10 µm² and 500 x 500 µm². The number of raster points (pixels) in the images is in the range of 1^2 to 2048^2 and is adjusted to the lateral resolution before the experiment is conducted. In this respect, lateral resolution of 100 - 300 nm are reached most often. New developments suggest lateral resolution even below 100 nm[85, 86]. For every single shot per pixel a complete mass spectrum is acquired. For high-resolution imaging, the buncher (chapter 3.1.2.1) is switched off, because it creates a higher kinetic energy spread in the ions of a single pulse, which leads to different beam deflections in the focusing lenses (chromatic aberrations). Consequently, longer ion pulses than in the spectrometry mode are used for high-resolution imaging, which allow a better focus of the primary ion beam. However, the mass resolution is limited to unit resolution due to these longer ion pulses, which makes the separation of signals based on their mass difficult (compare chapters 3.1.2.1 and 3.1.2.2). The results of the imaging mode are lateral distribution maps for all detected ions along with mass spectra at unit mass resolution for each individual pixel. The Burst mode and the delayed extraction mode offer a compromise of lateral resolution, mass resolution and analysis time (*i.e.* ion current). They can be used for imaging at high lateral resolution delivering high mass resolution at low primary ion currents or medium mass resolution at reasonable currents, respectively. These modes are explained in more detail in chapters 3.1.2.1 and 3.1.5.5.

3.1.3.3 Depth Profiling

Several possibilities exist to analyze the depth distribution of components within a sample. For ToF-SIMS on tissue slides an erosion of the surface is necessary to expose the layers below. A single ion beam can be used to analyze and sputter the sample, but the dual-beam approach with a second high current ion gun (dual-beam depth profiling) is more flexible and allows to optimize the analysis and the sputter parameters independently. The combination of a low-current analysis beam with a high-current sputter beam (compare chapter 3.1.2.1) allows the acquisition of depth profiles by alternating analysis and erosion steps. A further benefit of the dual-beam analysis approach is that depending on the nature of the sputter ion the secondary ion yield can be influenced (compare chapter 3.1.5.3). By selecting a suitable sputter ion and adequate ion energies depth resolution in the nanometer range can be achieved[87]. Ideally, the resulting data points represent subsequent layers from the surface into the depth of the sample. Consequently, the depth composition of the sample is acquired with a high mass resolution at routinely low lateral resolution. The previously mentioned compromise modes Burst or delayed extraction (chapters 3.1.2.1 and 3.1.2.2) can be used to shift the relation of lateral resolution, mass resolution and primary ion current also for depth profiling analyses.

3.1.3.4 3D Microarea Analysis

A depth profiling carried out with additional high lateral resolution is called 3D microarea analysis. This mode allows the analysis of a sample with high resolution in all three dimensions in space. However, the mass resolution suffers from the same effect as in the imaging mode. The Burst mode can be used for enhanced mass resolution, but comes along with much longer measurement times (chapter 3.1.2.1). The delayed extraction mode provides high lateral resolution, good mass resolution and suitable primary ion currents by decoupling the mass resolution from the primary pulse length (compare chapter 3.1.2.2 and 3.1.5.5).

3.1.4 Data Evaluation

All the data sets resulting from ToF-SIMS analyses have 5 dimensions consisting of the X- and Y- location, the cycle number (data point), the *m/z* ratio and the intensity. For analyses with a significant erosion (sputtering) the cycle number can be transformed into the depth information (Z-location). Depending on the analytical question different evaluation possibilities exist. These are explained in the following.

3.1.4.1 Mass Spectra

The typical ToF-SIMS mass spectra show a high number of signals of different intensities. Typically, the most intense signals are found in the lower mass regions with decreasing intensities towards the high end of the mass scale (Figure 3-7). The high number of signals is partially formed due to a primary ion beam with an energy in the keV range, which often leads to fragmentation of molecules. Low *m/z* ions down to H^+ are detectable. Compared to ESI mass spectrometry, where the desired species are mostly found in their protonated or deprotonated forms ($[M+H]^+$, $[M-H]^-$) or as a adduct ion $[M+X]^+$, $[M+X]^-$, ToF-SIMS spectra in general show a lot more molecular fragment signals, which can help assuring the identity of molecules even if the quasi-molecular ion is not observed or only of low intensity. Consequently, the use of databases often can be helpful to identify the parent molecules.

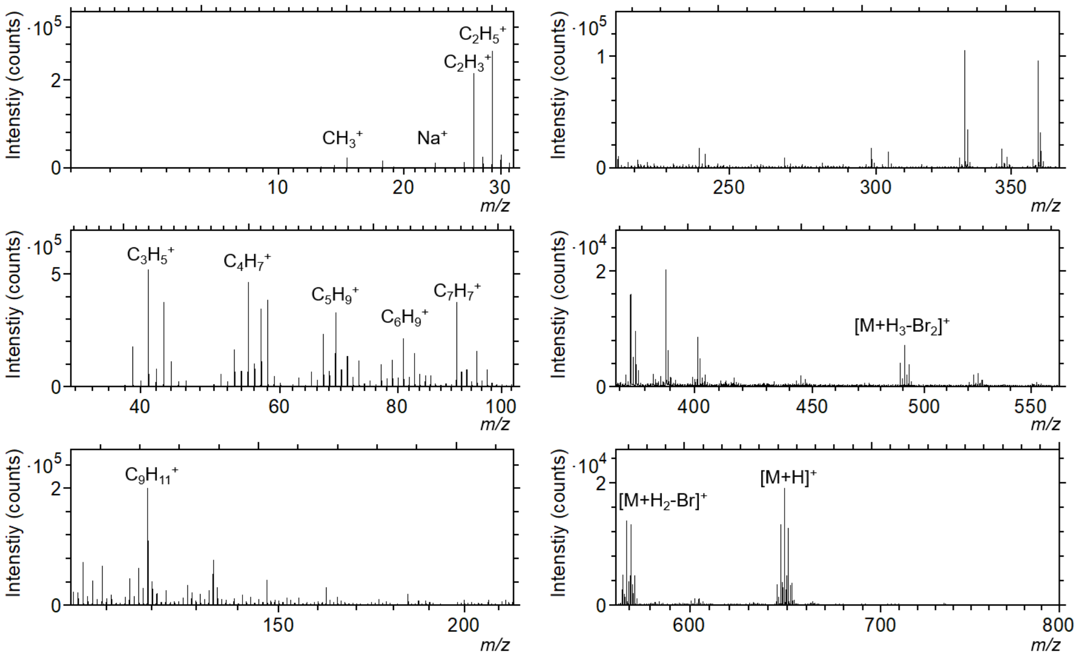

Figure 3-7: Exemplary secondary ion mass spectrum from an Eosin Y ($M = C_{20}H_8Br_4O_5$)-stained lung tissue section in the positive polarity. Most of the high intensity signals below *m/z* 100 originate from omnipresent hydrocarbon species, which are part of every spectrum. In the higher mass range lower signal intensities are observed. At *m/z* 648.63 the protonated molecular ion $[C_{20}H_8O_5{}^{79}Br_2{}^{81}Br_2+H]^+$ of Eosin Y is detected. The fragments of Eosin Y $[C_{20}H_8O_5{}^{79}Br_2{}^{81}Br+H_2]^+$ and $[C_{20}H_8O_5{}^{79}Br{}^{81}Br+H_3]^+$ are identified at *m/z* 568.73 and *m/z* 490.83 along with their respective isotopic patterns.

3.1.4.2 Images

ToF-SIMS images (XY-signal distributions) are usually displayed with a false-colour scale. In this thesis the so-called thermal colour scale is used starting with high intensities in white, lower intensities in yellow and orange to low intensities in dark brown and zero intensity in black (Figure 3-8, top row). The maximum counts per pixel (MC) and the total counts for the image (TC) are indicated. An additive colour mix (RGB overlay) of individual images displayed in red (R) Green (G) Blue (B) is used for correlation analysis *i.e.* to highlight differences or similarities between the lateral distributions of different ions (Figure 3-8, bottom).

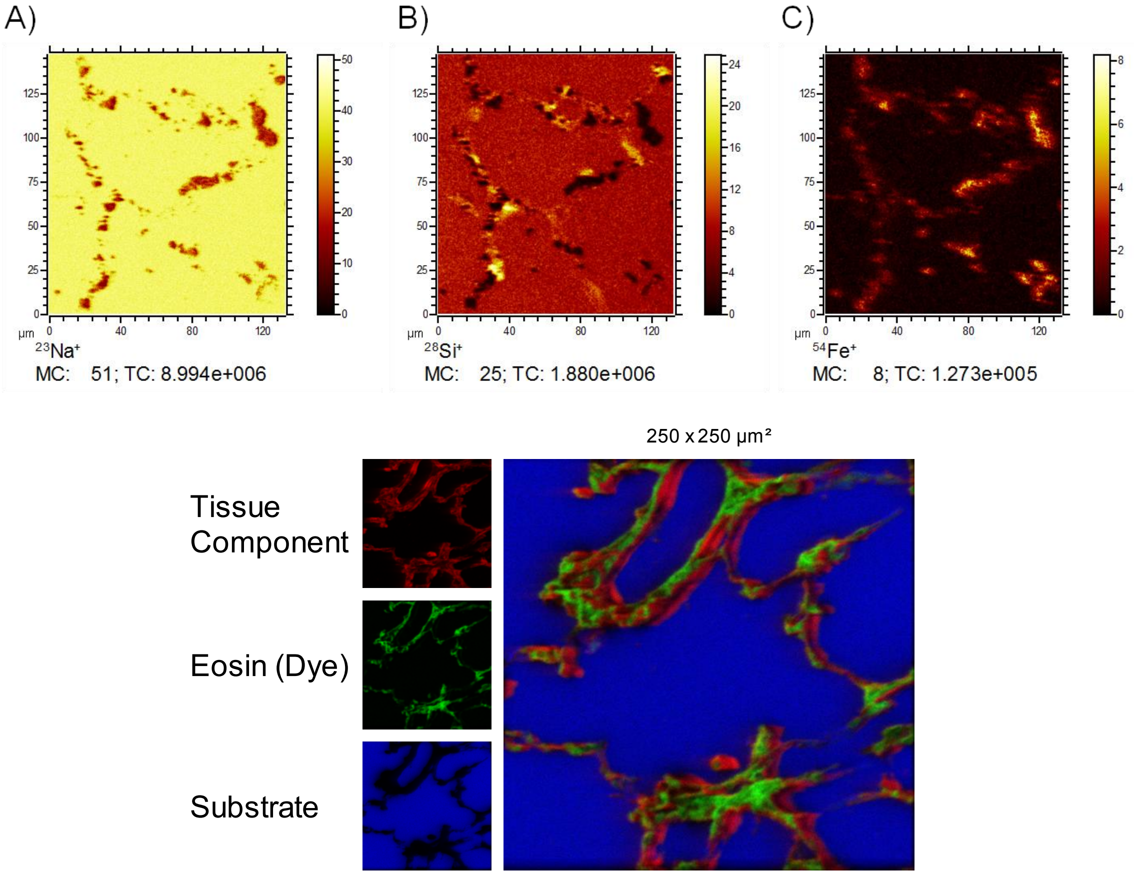

Figure 3-8: Exemplary results of imaging analyses. Top row: Secondary Ion Images of $^{23}Na^+$, $^{28}Si^+$ and $^{54}Fe^+$ from a core/shell particle study showing high intensities in light colour and low intensities in dark colour. MC indicates the maximum counts per pixel in the image, whereas TC represents the total number of counts for the complete image. Bottom row: RGB Overlay of ToF-SIMS results of an analysis of Eosin stained tissue.

3.1.4.3 Depth Profiles

Depth profiles show the course of the selected signals with increasing erosion time (*i.e.* depth) during the experiment (Figure 3-9). The sputter time is displayed on the x-axis and the signal intensity for the selected secondary ion on the y-axis. However, also the applied ion dose or the data point number, as well as the depth are also used on the x-axis. The depth can be calculated for well-known sample systems based on ion doses and sputter yields (calibration to reference samples) or needs to be determined by a measurement of the total crater depth reached (*e.g.* via in-situ profilometry). The intensity scale is most often displayed in a logarithmic scale because the changes in intensity often encompass several orders of magnitude.

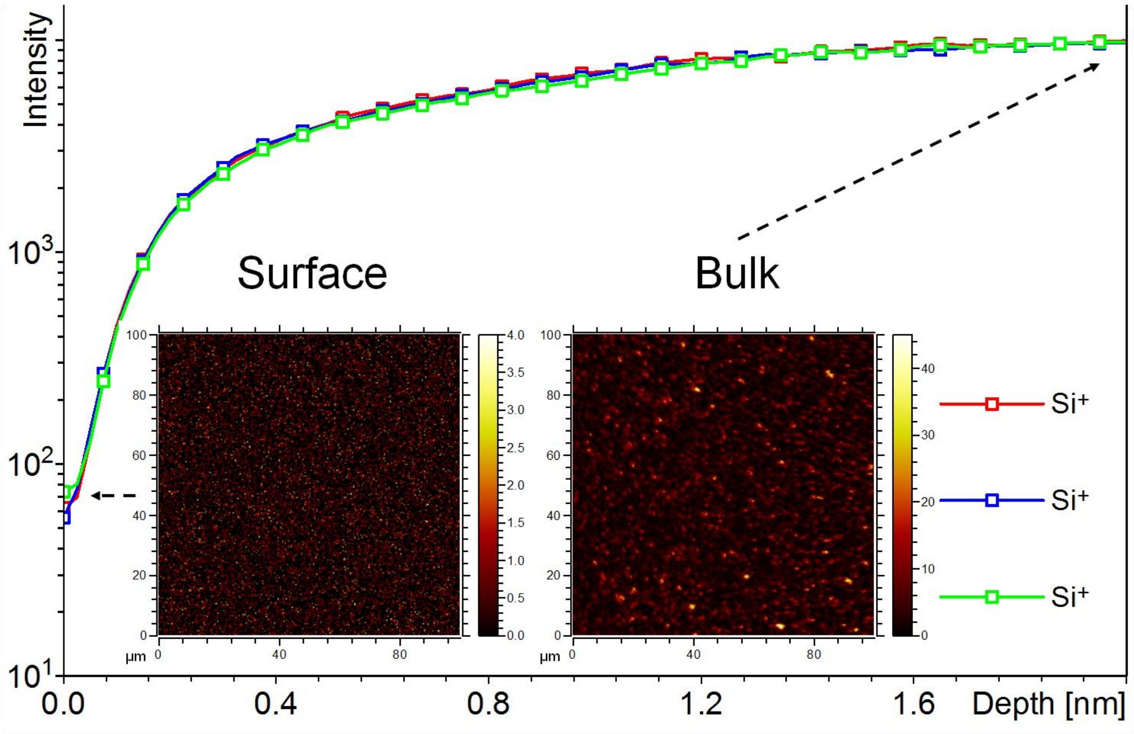

Figure 3-9: Replicate depth profiles of a SiO_2 nanoparticle-containing matrix. The lateral homogeneity of the sample is proven by analysis of neighbouring areas. The three colours (red, green, blue) represent replicate analyses, while the inserted images show the revelation of the particles in the bulk compared to the surface of the sample for one of the data sets.

3.1.4.4 3D Analysis

The 3D analysis offers several different possibilities for the data evaluation of a ToF-SIMS analysis. Among these is the possibility to display different sections (X-Z and Y-Z as well as X-Y) in retrospective analyses of the data cube (Figure 3-10). These images allow a fast assessment of the lateral and depth distribution and allow the identification of interfacing layers or subsurface structures.

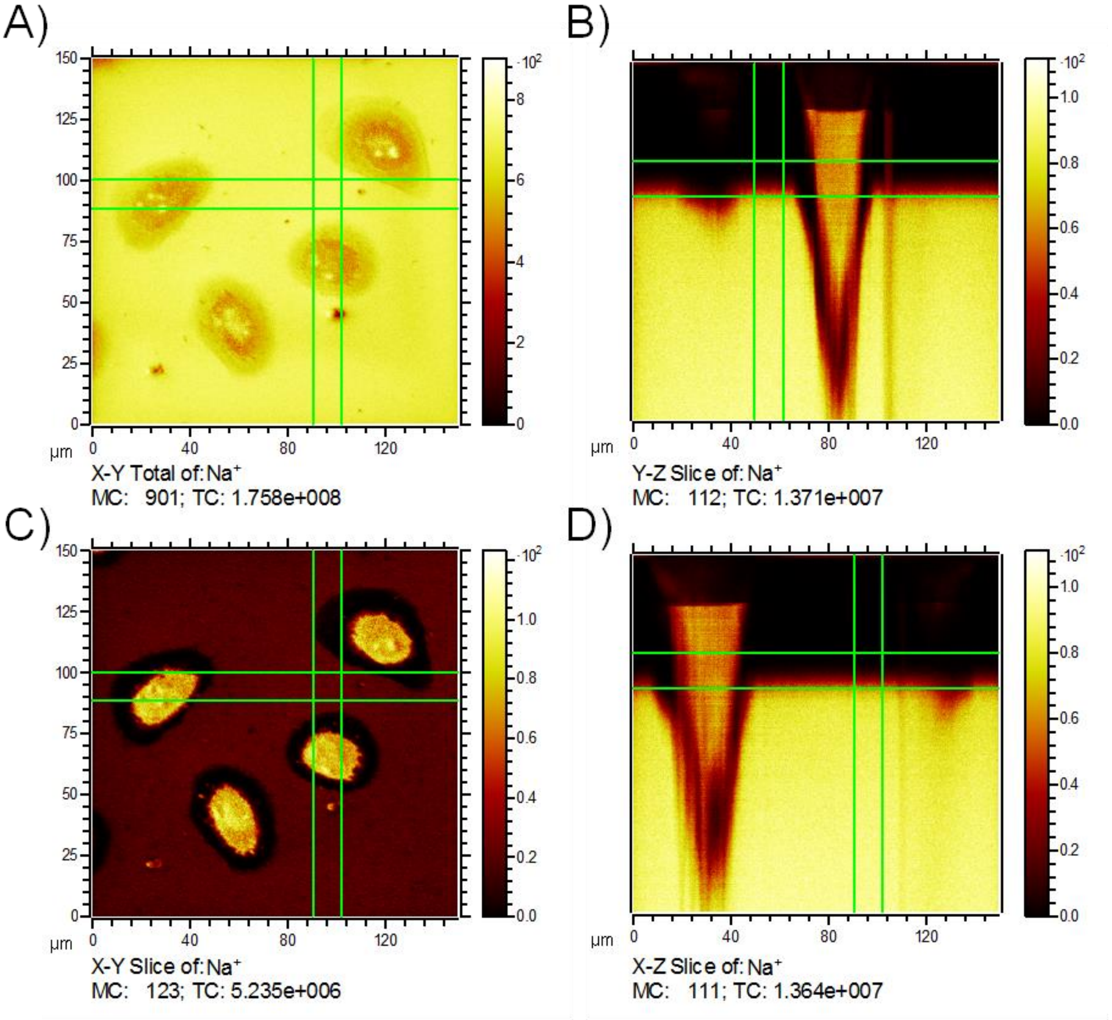

Figure 3-10: Spatial distributions of Na$^+$ in the 3D analysis of NRK cells on a glass substrate. The green lines indicate the positions of the reconstructed sections of the data cube. A) The X-Y total of Na$^+$ image shows the Na$^+$ signal summed up for the complete depth of the analysis (*i.e.* a projection of the 3D data onto a plane). Relatively high Na$^+$ signals are observed on the complete field-of-view with slightly less intensity at the positions of the cells. C) The X-Y slice shows the Na$^+$ distribution for a section of the 3D data set, where the Na$^+$ intensity from the substrate is less pronounced. A significant amount of Na$^+$ in the cells is visualized. B) and D) The X-Z and Y-Z slices reveal that Na$^+$ intensity comes from the cells and from the substrate. The cells appear stretched because the z-axis only relates to few micrometers whereas x-axis and y-axis encompass 150 µm. The substrate does not appear planar because the cells partially shield the substrate from the sputter erosion. This leads to a delayed sputtering of the substrate below the cells. As the data set is acquired from surface (top) to the bulk (bottom), the substrate surface appears rough.

3.1.5 Analytical Parameters

As described before (chapter 3.1.3), the instrumental parameters need to be optimized according to the analytical question. In this respect, the choice of the polarity, the primary ion, the sputter ion and the sputter rate as well as the experimental mode are of interest. An important aspect of the analytical strategy was to increase the sensitivity (choice of primary ion, sputter ion, sputter rate ratio) and to enable a good lateral as well as mass resolution (compare scope of this thesis, chapter 2). The analytical strategy, which was developed and optimized in this thesis is innovative especially with respect to the experimental conditions, as the delayed extraction mode is applied in ToF-SIMS experiments usually only for the reduction of topographic field effects.[78]

3.1.5.1 Polarity

In general, the positive polarity should be used for all analyses in this thesis, because all the analysed/targeted nanoparticles are based on metal oxides (Fe_2O_3/SiO_2, CeO_2, ZrO_2) or metalloid oxides (SiO_2FITC). As a result, the main components of all particles are electropositive and readily form positively charged species (compare chapters 5, 7, 8).

For the detection of the SiO_2FITC nanoparticles, however, the negative secondary ion polarity was chosen to exclude any potential influence of the widespread Si-containing polysiloxane contaminants, which had been observed on similar samples in earlier experiments (compare chapter 6). Polysiloxanes are polymer chains with [$-SiR_1R_2-O-$] repeating units and are frequently found as lubricants in a variety of products[88]. In consequence, these substances form secondary ions such as Si^+ and SiO^+, $SiOH^+$, Si_2O^+, Si_2OH^+ (and more) in the positive ion mode and Si^-, SiO^-, $SiOH^-$, SiO_2^-, SiO_2H^- (and others) in the negative ion mode.[89] All of these signal are also detected upon analysis of the silica based nanoparticles.[90] However, due its chain structure the polysiloxanes do barely form SiO_3^- ions, which are readily formed by the silica based nanoparticles, due to the close proximity of the Si to the O atoms in the crystal lattice. As a result, this ion can exclusively be detected in the negative secondary ion polarity from the silica based nanoparticles.[90]

3.1.5.2 Primary Ion Selection

The Bi LMIG previously described (chapter 3.1.2.1) was selected as the primary ion gun of choice for the experiments in this thesis, as it provides the desired combination of short pulse lengths, high lateral resolution and the sufficient ion currents. However, the selection of a suitable Bi_x^{n+} primary ion species via pre-chopper and chopper for the experiments is a necessity to achieve optimized conditions for the experiments, as it can serve as a fine adjustment of influences on the secondary ion yield, the surface damage, the penetration depth and the achievable lateral resolution. The Bi LMIG provides Bi_x^+ clusters with x = 1 - 7 at notable ion currents. Furthermore, besides singly charged species also doubly charged species are available, which have twice the kinetic energy.[84] With respect to one of the main goals of achieving a high **sensitivity**, the use of polyatomic primary ion species is a must to benefit from the non-linear effects on the secondary ion yields[91]. Additionally, the volume damaged by the primary ion impact is smaller. Bi_3^+ ions are a compromise of increased secondary ion yields and high primary ion currents, since they comprise a major fraction of the total primary ion current of the Bi LMIG.[84] In consequence, they deliver high signal intensities in relatively short measurement times. Furthermore, the secondary ion emission of larger cluster ions is favoured by cluster impact, which leads to more high mass signals (M_xO_y clusters), which can serve to prove the identity of substances. Those increased secondary ion intensities (compared to monatomic primary ions) can support the **reliability** for the identification of low abundant signals. This, in consequence, improves the identification of substances solely based on ToF-SIMS results, which brings the ultimate goal of **marker-freeness** one step closer.

The applied choice of Bi_3^+ is in line with the literature as Touboul *et al.* found Bi_3^+ and Bi_5^{2+} to be the most relevant primary ions for imaging of a tissue sample far superior to previously used gold cluster ions.[84]

3.1.5.3 Sputter Ion Selection

After sectioning of a nanoparticle-containing tissue, only few nanoparticles are expected to be accessible directly at the surface, while most of the particles are assumed to be in deeper layers of the tissue section. Primary ion currents in ToF-SIMS are not sufficiently high to erode a surface significantly. Therefore, a second primary ion beam (*i.e.* sputter ion beam) for the erosion is applied (dual beam depth profile, chapter 3.1.3.3). The sputter beam is used to expose the nanomaterials in the tissue sections, which are not present at the topmost surface. The selection of the right sputtering conditions can critically influence the outcome of the analysis. As the detection of nanomaterials in tissue is the primary goal in this thesis, the conservation of organic information throughout the analysis is not of primary importance. On the contrary, as the detection of the inorganic components is most important, the signals of organic molecules might cause interferences with the low intensity nanoparticle signals and should therefore be avoided. As a result, the analyses benefit from a relatively high sputtering energy, because the high energy of the sputter beam leads to fragmentation of large molecules and therefore limits the number of interfering signals in the higher mass range to enable a sensitive detection of the desired species (relevant in particular for Ce_xO_y-species with *m/z* > 140 in chapter 7). Consequently, predominantly small molecules or inorganic cluster signals contain information at the necessary high signal intensities to analyze their lateral distributions.

However, gas cluster primary ions can be used if information on the organic composition is desired (chapter 8). This type of sputter ion was selected to explore/demonstrate the possibilities (suitability) of simultaneous detection of organic species and nanoparticles by cluster sputtering.

With regards to **sensitivity**, O_2 sputtering was chosen as it increases the secondary ion yield for electropositive elements and favours the detection of electropositive species (chapter 5, 7, 8). Additionally, by providing excess oxygen to the surface the maximal high occupation of the M^+ and MO^+ ionization channel for the oxide species is ensured. These measures improve the secondary ion yield for the nanoparticle signals and result in low limits of detection. Furthermore, by increased intensities even of smaller signals the **reliability** of the identification is improved. Both of these effects promote the necessities for a marker-free detection of nanoparticles solely by ToF-SIMS.

Cs was selected as the sputter ion for the detection of the SiO_2-FITC nanoparticles (chapter 6), because it improves the emission of electronegative species. As the desired secondary ion SiO_3^- is rich in electronegative oxygen, a high secondary ion yield (*i.e.* high **sensitivity**) can be expected upon Cs sputtering. Furthermore, introducing excess oxygen to the surface (*e.g.* via oxygen sputtering) should be avoided to prevent changes in the expected ionisation patterns of polysiloxanes (compare chapter 3.1.5.1).

3.1.5.4 Sputter Rate Ratio

With regard to **sensitivity** the ratio between sputter erosion and analysis time was optimized to achieve a high amount of analysis time (*i. e.* high signal intensities) with only little sputter erosion (*i. e.* material lost for the analysis). As the goal in the publications (chapters 5-8) was a sensitive detection of small amount of nanomaterials for a comparison with other imaging techniques, the sputter rate ratio was not optimized to achieve 3D signal distributions, but for a projection of the 3D information onto a 2D plane.

3.1.5.5 Delayed Extraction

The detection of nanoparticle-related signals in biological tissue is challenging due to the low intensity of the signals and the high background of unknown species. Therefore, a sensitive detection at **acceptable mass resolution** is necessary to unequivocally identify the desired species. Furthermore, a **high lateral resolution** is a prerequisite to precisely localize the nanoparticles and enable a comparison with other techniques. These requirements are not fulfilled by the standard operational modes (compare chapter 3.1.3).

One option is the burst mode, which provides the desired resolution at reduced primary ion currents (chapter 3.1.2.1). However, due to the low number of primary ions this mode is in particular not suitable for the acquisition of low intensity signals (*e.g.* small amounts of nanomaterials), because of the extreme time consumption and the required instrumental stability over tens of hours.

Another option to reach the desired combination of high mass and lateral resolution is the delayed extraction mode (chapter 3.1.2.2), which additionally provides reasonable primary ion currents and shorter analysis times. These primary ion currents allow the **sensitive** detection of the nanomaterials in tissue. Consequently, this analysis mode is used in conjunction with the 3D microarea analysis mode in chapters 5-8 in this thesis to facilitate comparisons of high-resolution ToF-SIMS analyses with other techniques. The delayed extraction mode is rarely used in standard ToF-SIMS analyses, but enables a fruitful analytical strategy to analyse nanoparticle-containing tissue sections.

3.2 Reference Techniques

Several reference techniques were used to assess the ToF-SIMS results. These are described briefly in the following. Further information is provided in the respective chapters (5-0) or can be assessed from the given references. First, conventional optical light microscopy (chapter 3.2.1) and fluorescence microscopy (chapter 3.2.2), are described. Second, introductions into the X-ray technique µ-XRF (chapter 3.2.3) and the ion beam microscope (IBM) (chapter 3.2.4) are given.

3.2.1 Optical Microscopy

Optical microscopy is a widely used technique for the investigation of samples with structural characteristics not visible to the bare eye. The interaction of a specimen with a beam of electromagnetic waves (absorption, transmission, reflection) leads to modifications of the original light beam. After interaction the beam bears information on the sample, which is displayed as an image.

Optical microscopy is an extremely versatile technique and can deliver information on physical, chemical and biological attributes. As it is a relatively inexpensive technique (considering acquisition, operation conditions and maintenance) and needs minimal sample preparation, it is often used for a first assessment of the structures on a wide variety of samples. Resolving powers of about 200 nm are typically reached. However, several different microscopic modes of operation are known. Three different lighting options used in this thesis are briefly described in the following. More comprehensive information can be obtained from the indicated literature references.[92-96]

3.2.1.1 Transmission Light Microscopy

In transmission light microscopy the specimen is illuminated in such way, that the light has to pass through the sample to enter the objective. As a result, this mode is mostly used for the analysis of transparent and thin sections. As a consequence, the outcome of the analysis is mostly affected by absorption effects. Light from scattering or diffracting components might not reach the objective and therefore results in darker areas in the image.[92]

3.2.1.2 Incident Light Microscopy

Incident light microscopy (*i.e.* reflected-light microscopy) uses an illumination from above the sample and collects the light reflected into the objective. As a consequence, this mode is suited for opaque and relatively thick samples.[92]

3.2.1.3 Dark-Field Microscopy

Dark-field microscopy, in contrast to the bright-field microscopy techniques incident light microscopy and reflected-light microscopy, illuminates the specimen not within the aperture of the objective but from the outside. As a result, only scattered light reaches the objective and is observed as a bright spot on an otherwise dark background. As a consequence, this mode provides high contrast and allows an identification of angled surfaces (particles), which often are not visible in bright-field microscopy.[94] With this technique individual nanoparticles have been observed.[97, 98]

3.2.2 Fluorescence Microscopy

In fluorescence microscopy the specimen is irradiated with intense light of a short wavelength. Fluorescing substances absorb the light and re-emit light of a longer wavelength. The fluorescence microscope separates the emitted light from the excitation light and presents the fluorescent areas against a dark background. Prerequisite for fluorescence microscopy is the availability of species with inherent fluorescence features or fluorescently labelled components (markers). This technique can detect extremely small numbers of molecules such as 50 molecules per cubic micrometer and is used for organic and inorganic samples[96]. However, the presence of autofluorescence might influence the limits of detection.[92, 96] A more detailed discussion can be found elsewhere[99].

3.2.3 Micro X-ray Fluorescence Spectrometry

In this technique, an X-ray beam induces the ejection of electrons from the sample. Upon emission of such an electron from an inner orbital, another electron from a higher energetic level (*i. e.* outer orbital) will fill the vacancy in the inner orbital. The energy difference of the orbitals is emitted as a photon with the respective energy. The energy difference is specific for the element and thus allows the identification of the elemental origin of the electron. Micro X-ray fluorescence spectrometry employs the same principle, but features a focused X-ray beam at lateral resolution of down to 25 µm (for bench-top instruments) and therefore allows elemental imaging of the sample. The technique is frequently applied in geology, forensics and semiconductor industry.[100, 101] Detailed information can be found in the literature.[102]

3.2.4 Ion Beam Microscopy

The ion beam microscopy technique simultaneously comprises the particle induced x-ray emission (PIXE) and the Rutherford backscattering spectrometry (RBS) in a single experiment. For both applications the sample is typically irradiated by protons or Helium ions with MeV energies. Both approaches are briefly described in the following. IBM is capable of reaching spatial resolution of about 500 nm and ppm limits of detection.[103]

The combination of both approaches allows a quantitative determination of the concentrations of matrix elements, trace elements and nanomaterials at the single cell level.[104] The instrument used for the analyses in this thesis is the Leipzig Ion Nanoprobe LIPSION. Further information can be found elsewhere.[105-107]

3.2.4.1 Particle Induced X-ray Emission

PIXE analyses the X-ray fluorescence upon bombardment with high energy (MeV) protons. The ejection of electrons from inner orbital provoke filling of the vacancy with higher energy electrons from outer orbitals. As a result, an X-ray emission can be induced, which is analyzed for the energy and indicates the elemental origin of the electron. The PIXE allows the acquisition of distributions and concentrations of heavier elements with $Z > 12$ at sensitivities in the ppm range.

3.2.4.2 Rutherford Backscattering Spectrometry

The RBS is an ion scattering technique analyzing the energy of the backscattered protons. The energy of the backscattered protons is dependent on the impact partner and the depth of the impact. Therefore, information on the elemental composition of a sample can be derived from the proton energy. Furthermore, also the depth composition of the sample is accessible. Consequently, the in-depth distributions of nanoparticles in z-direction and information about their internalization into cells are accessible.

3.3 Nanoparticles

3.3.1 Definition and Properties

Via definition, the dimensions of nanoparticles in all three dimensions in space are below 100 nm.[1] These particles often exhibit enhanced inherent or completely new properties, due to their dimensions between atoms and bulk materials[4]. With decreasing size, the surface area and the relative number of surface atoms increases. These surface atoms provide more accessible interaction points for surrounding species compared to the bulk materials. Hence, high affinities towards surface reactions (*e.g.* oxidation of metallic nanoparticles) are observed. Furthermore, high strength, durability, conductivity, solubility and surface-to-mass ratios of selected nanomaterials are attractive features for the use in a variety of applications[17, 108]. As a consequence, the use of nanoparticles in commercial applications (*e.g.* in automotive, construction, semiconductor, food industry) is increasing.[4] However, the potential hazards of contact to nanomaterials is a matter of numerous toxicological studies[109]. Relevant physico-chemical properties of nanomaterials for toxicological studies include size, size distribution, shape, agglomeration, porosity, charge and surface chemistry[23, 110]. In consequence, the characterization these parameter of nanoparticles is a highly important topic to obtain meaningful results from toxicological studies[111, 112]. One of the most important parameters for toxicological studies is the size of the nanoparticles, because it influences their localization and biodistribution[113, 114]. A widespread technique to analyse the size is dynamic light scattering (DLS), which measures Brownian Motion in a dispersion and relates it to the hydrodynamic particle size. In consequence, the dispersion of the nanoparticles is a critical parameter for DLS. This method is less suitable for multimodal particle distributions and for non-spherical particles, because it assumes a hard sphere as a model for the NP. Therefore, significant differences in comparison to microscopic techniques, which reveal the primary particle size, are observed.[115] This particle size is relevant in particular for aerosols, because a number of nanoparticles readily form agglomerates upon contact with biological media. Since in this thesis instillation studies are the topic, the hydrodynamic diameter in the medium (*i.e.* instillation fluid) is more relevant for the distribution processes and consequently used, whenever referred to sizes and diameters.

3.3.2 Exposure to Nanomaterials

With the increasing use of the nanomaterials in consumer products, also the exposition of organisms to nanomaterials increases[116]. The exposure to nanoparticles can happen via the use of nanoparticle-containing products, such as sunscreen or cosmetics. Furthermore, the exposition also might take place via airborne nanoparticles from food additives, exhaust catalysts, fuel additives or from processing of nanoparticles-containing products.[117-120]

For mammals, the most important exposition is considered to be taking place via the skin, the gastrointestinal tract or the lung[23]. As the skin provides a relatively thick barrier of dead cells, the uptake route via the skin into the body can be assumed to be of low relevance. However, the uptake of nanoparticles via hair follicles is well known[121, 122]. The uptake of nanomaterials via the gastrointestinal tract is conceivable for food or beverages containing nanoparticles. Furthermore, nanoparticle-containing food supplements are available[116]. The uptake of inhaled particles via swallowed sputum should be limited to larger particle sizes (see chapter 3.4.1.1). The uptake of nanoparticles via the lung, however, can happen easily via airborne particles. With decreasing sizes of the nanoparticles, the penetration depth into the respiratory pathways increases. Particles larger than 5 µm in diameter mainly deposit in the mouth and throat, whereas smaller particle reach deeper levels of the lung.[17] The clearance mechanisms for particles are described in chapter 3.4.1.

3.3.3 Relevance of Nanomaterials used in this study

In this thesis, the nanomaterials Fe_2O_3/SiO_2 (core/shell), FITC/SiO_2 (core/shell), CeO_2 and ZrO_2 were selected to be studied in detail. The selection criteria and importance of these nanomaterials are outlined briefly below.

SiO_2 nanoparticles are used in a variety of applications (*e.g.* as an additive for foodstuffs[7], as a filler for composite materials[123], as an abrasive[124]). Therefore, the exposition to particles of this type upon manufacturing products or processing of composite materials is likely. Furthermore, severe effects up to formation of cancer have been observed upon inhalation of crystalline silica in rats.[119, 125] In consequence, the distribution mechanisms of silica-based nanoparticles upon inhalation into mammalian organisms are of high interest. Therefore, the localization of nanoparticles in lung tissue is analysed in chapters 5 and 6.

CeO_2 nanoparticles are used as additives to automotive fuels to reduce the fuel consumption of diesel engines[118], as catalysts for exhaust fumes by providing oxygen[126] and as one of the main ingredients for chemical-mechanical planarization in the semiconductor industry[127, 128]. CeO_2 nanoparticles could be detected in lung tissues of mammals[120] and several negative effects in environmental organisms such as earthworms,[129] nematodes[130] and zebrafish[131] were observed. The detection of these types of nanoparticles in tissues is desired as a consequence of the potential emission risk and several negative effects in environmental organisms and is shown in chapter 7.

ZrO_2 nanoparticles are used as additives for ceramic composites in structural engine parts and medical applications such as hip replacements or dental implants providing high strength and smoothness[132-134]. Due to its ionic conductivity for oxygen at high temperatures, ZrO_2 is also used in solid oxide fuel cells and in gas sensors.[135, 136] An early study on ZrO_2 dust exposition did not show differences between exposed workers and the control group[137]. However, this study only did not consider the exact particle sizes. Further experiments on animals and systematic studies were suggested. As moderate toxicities were observed for these particles on lung cells[138], further experiments seem reasonable and are the matter of chapter 8.

3.4 The Lung

3.4.1 Lung Structure

As discussed beforehand (compare chapter 3.3), the respiratory pathway is one of the main entrance pathways of nanoparticles into the mammalian body. As the mammalian lung is of special interest in this respect, it was chosen as the origin of all tissue analysed in this thesis.

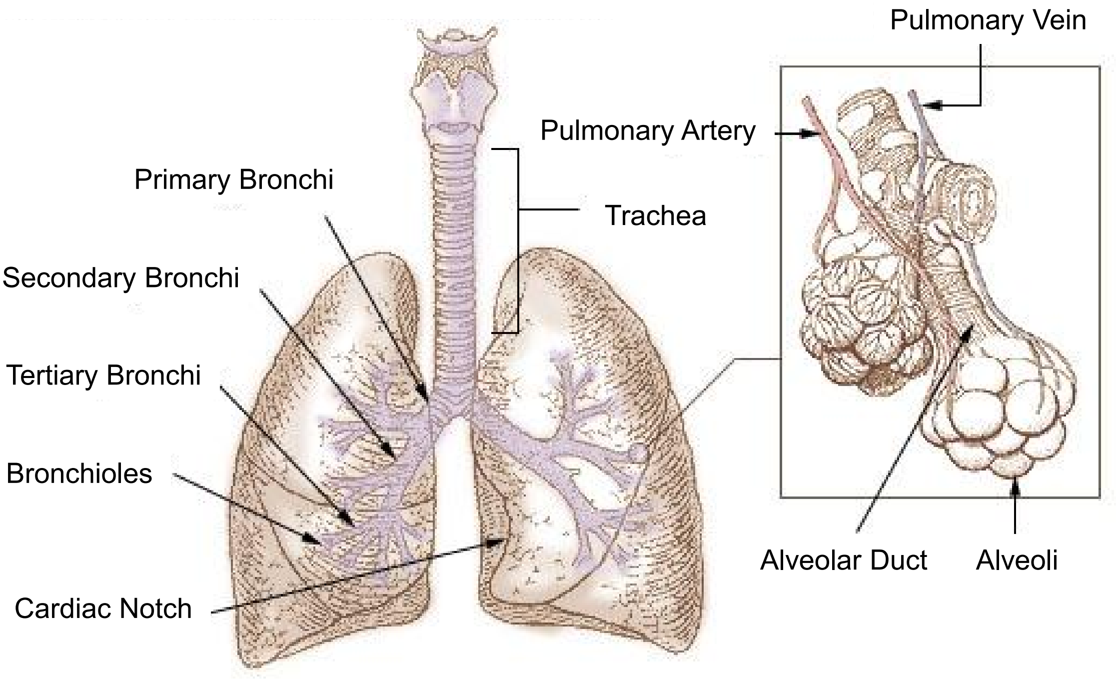

Figure 3-11: Schematic representation of the human lung. Several branchings from the trachea into primary bronchi, secondary bronchi, tertiary bronchi and bronchioles are visible. The inset shows the typical structure of the alveoli as the endpoints of the respiratory system along with the pulmonary artery and vein (adapted from public domain material[139]).

The mammalian lung facilitates the gas exchange of O_2 and CO_2 between the blood and the surrounding air. Since this process is driven by gas diffusion, the efficiency is limited by the surface area, which is in contact with the gases.[140] As a consequence, the lung needs a large surface area to maintain an efficient breathing process. The necessary large surface area is achieved by several branchings of the respiratory airways from the single trachea to the hundreds of millions alveoli (Figure 3-11) providing a surface area of about 100 m^2 for a micrometer thin diffusion barrier.[141] Here, an overview of the lung structure and the cellular structure of the alveoli is given. A detailed morphologic description is beyond the scope of this thesis and can be found elsewhere[141].

3.4.1.1 Structural Overview of the Lung

The respiratory system starts from the trachea, diverging into the two main bronchi and from there into the lobes of the lung (Figure 3-11). In the lobes several further branchings lead to the secondary and tertiary bronchi. Furthermore, these bronchi branch into the bronchioli. From the trachea to the *bronchioli terminales* all of the airways are covered by a mucous membrane with cilia-containing cells, which captures extraneous particles and removes them from the system.[141] From there the next branches, the *bronchioli respiratorii*, divide further into the alveoli. The alveoli are the endpoints of the respiratory system where the gas exchange takes place. They have a sac-like shape and form clusters of interlinked caves providing a large surface area (Figure 3-11, inset). Nanoscopic particles are able to enter these endpoints. In consequence, the alveoli are interesting targets for the analysis of the fate of the nanoparticles upon inhalation. As sections of alveoli are in the focus of interest of this study the cellular structure of the alveoli is described in the following section.

3.4.1.2 Cell Types in the Alveoli

The alveoli are the endpoints of the pulmonary branches and increase the surface area of the lung. They are hemi-spherically shaped and encompass 3 major cell types:

Type I pneumocytes form a covering layer and provide the diffusion barrier for the pulmonary capillary blood. Their cell organelles are localized closely to the nucleus. This structure allows the formation of thin (< 0.2 µm) and up to 50 µm long protuberances providing a large surface area, which covers about 95% of the total alveolar surface.[142]

Type II pneumocytes cover the remaining 5% of the alveolar surface. In contrast to the flat-shaped type I pneumocytes they have a compact cuboidal shape. These cells produce the pulmonary surfactant and distribute it into the alveolar space. The main components of the pulmonary surfactant are phospholipids, proteins and cholesterol. The surfactant reduces the surface tension in the alveoli and reduces the energy necessary for breathing.[141]

Alveolar macrophages come from the blood into the alveoli, where they can move on the blood-air-barrier. They clean the alveoli by the degradation or the removal of foreign particles.[140, 141] Thus, a localization, and, thus possible detection of nanoparticles within the lung is expected either in the alveolar room, the macrophages or the pulmonary cells.

3.4.2 Sample Preparation

In order to analyse nanoparticle-containing samples, a multi-step sample preparation process was required. Besides the instillation, extraction and sectioning the lung tissue, the selection of a suitable substrate was necessary. A brief overview of the sample preparation process and the selection of a substrate is provided here. Detailed information on the sample preparation is provided in the experimental sections of the respective chapters.

3.4.2.1 Rat Lung Tissue Preparation

Rats are a typical model organism for mammals in a variety of toxicity studies.[143-145] The main reasons are the similarities in their internal functioning to humans and the simple and inexpensive maintenance.[146] In this study, the exposition to the nanoparticles was facilitated by intratracheal instillation of rats. This included a brief anaesthesia with 5% isoflurane in air followed by the instillation of the instillation fluid via a micro-sprayer directly into the lung. The instillation fluid contained the nanoparticles freshly suspended in a buffered saline by an ultrasonication treatment. After the instillation the rats were sacrificed and the lung was inflated with a cryomatrix. All animal related experiments were part of a major toxicity study (NanoBioDetect project, grant no. 03X0146) and were performed by the cooperation partner IBE R&D Institute for Lung Health gGmbH (Münster, Germany). The experiments were ethically approved by the local authorities (LANUV, Dortmund, Germany). After resection the lung was snap frozen and cut to section with a cryomicrotome. The sections were placed onto substrates and stored at -28 °C. A number of important points have to be considered to select a suitable substrate for ToF-SIMS analysis. These are discussed in the following chapter.

3.4.2.2 Substrate for ToF-SIMS sample carrier

A number of aspects have to be considered for the choice of the substrate (sample carrier) material: In general, a flat substrate is preferred, to prevent avoidable flight time differences in the mass spectrometer, which would result in signal broadening and poorer mass resolution. Furthermore, a conductive substrate should be selected to prevent (local) charging effects induced by the bombardment with primary ions and sputter ions during

ToF-SIMS analysis.[83] At the same time, an optically transparent substrate is helpful to enable microscopic analyses. Furthermore, the use of standard-sized substrates is reasonable to ensure similar geometric alignment for all samples. The choice of the substrate is crucial when it comes to the analysis of particles consisting of elements, which could be part of the substrate composition. As an example, the discrimination of the signals for silica nanoparticles from the Si signals of the substrate on a regular glass slide is not possible. Furthermore, substrates without interfering components should be chosen according to the desired particles in the sample. Ideally, a substrate should result in secondary ions that do not disturb the analysis via intense signals close to the *m/z* of the desired species and on the other hand facilitate a straightforward mass calibration by the introduction of intense signals with a distinct isotopic pattern. In order to enable all the aspects (flatness, conductivity, transparency, composition) mentioned above, indium-tin-oxide (ITO) coated microscopic glass slides (Sigma-Aldrich, Taufkirchen, Germany) with a surface resistivity of 70-100 Ω were selected as the standard substrate of choice for the studies in this thesis. The conductive ITO surface allows a fast balancing of local charging effects. The transparency of the microscope slides allows easy microscopic analyses and thereby improves the navigation on the sample in the ToF-SIMS instrument. Due to the conventional size of the slides, usual microscopic slide equipment can be used and a fast and reproducible geometric alignment is facilitated. The composition of the ITO layers does not interfere with the frequently used nanomaterials. Another advantage is the introduction of high mass monoatomic In and Sn ions into the mass spectra. These can be used as omnipresent calibrations points in the mass spectra and can accelerate the calibration of the spectra and thereby speed up the whole interpretation process of lung tissue analyses.

Chapter 4

State-of-the-Art: Nanoparticle Detection in Tissue by ToF-SIMS

4. State-of-the-Art: Nanoparticle Detection in Tissue by ToF-SIMS

4.1 SIMS Application to Biological Samples

Initially secondary ion mass spectrometry was typically used for the analysis of inorganic materials.[147] Therefore, many early applications were performed in material science, geology and cosmochemistry.[148] However, the developments in the SIMS technology were driven by the needs of the main industrial applications in the semiconductor industry[149]. Nowadays, the use of SIMS *e.g.* in the semiconductor industry is routine for analysis and contamination control.[147]

The first ToF-SIMS instruments became commercially available in 1983.[150] With these instruments the detection of molecular species as (quasi) molecular ions was possible. Due to the simultaneous detection of organic and inorganic components, ToF-SIMS offers a particular suitability for screening analyses of samples with unknown composition. It has developed into one of the main surface analytical techniques for failure analyses and root-cause analyses in surface analysis[76, 151].

The growing use of SIMS for soft biological samples is a rather recent aspect promoted by further developments of the technique. Increased sensitivity, improved spatial resolution and the possibilities for the identification of intact molecules by the development of new instruments and ion sources were necessary breakthroughs for the application of SIMS to biological questions.[148] New developments promote the analysis of inorganic materials in organic matrices (composite materials). Especially with the upcoming relevance of nanomaterials, the applications of ToF-SIMS were extended to these new materials.

A discrimination between continuous-beam (direct current, DC) sector-field mass analyzer instruments and the ToF mass analyzer SIMS instruments is necessary, because the so-called "dynamic SIMS" sector-field instruments have fundamentally different properties compared to the pulsed Time-of-Flight mass analyzer instruments (ToF-SIMS). Dynamic SIMS instruments can be adjusted to offer a combination of mass resolution (*e.g.* 7000; sufficient to separate ^{32}S and $^{16}O_2$) and extremely high lateral resolution (<50 nm) [152-154]. However, to achieve this, the ion current and transmission are reduced[155].

The sector-field based instruments (*e.g.* NanoSIMS, Cameca, Gennevilliers Cedex, France) with lateral resolution up to 30 nm were successfully used for biological samples[156]. They usually employ continuous (DC) high-energy ion beams, which lead to extreme fragmentation of molecules when using monoatomic or small polyatomic primary ions. However, the use of large cluster ions for dynamic SIMS has been reported[157]. In the case of small primary ions only elemental or di-atomic secondary ions can be detected.

Although this thesis only deals with ToF-SIMS some aspects of the applications of sector-field mass analyzer instruments to biological samples are briefly mentioned in this chapter, since these instruments provided the basics for the application of the ToF-SIMS instruments towards the biological samples and some findings of this thesis will be discussed in the light of dynamic SIMS results. Therefore, a brief description of the aspects of both techniques is provided within separate paragraphs below.

4.1.1 Dynamic SIMS of Biological Samples

Many of the dynamic SIMS research articles in the biological field are studies based on metabolism.[156, 158-162] Due to the extensive fragmentation of molecular species, the analysis of biological pathways is often facilitated by following the distributions of molecules via bound isotopic tags (^{2}H, ^{13}C, ^{15}N, ^{18}O, *etc.*) or elements with low abundance in the tissue (*e.g.* F, I). Therefore, often a labelling step is needed. Several studies expand the metabolism investigations to micron-sized microbes making use of the impressive lateral resolution of tens of nanometres for the analysis of individual cells. In such studies, microbes are typically fed with isotope tagged substrates and the analyses show where the isotopic tags remain after metabolising.[153, 163-166] A method for quantitative imaging of cellular uptake of isotopically labelled tracers (*e.g.* ^{15}N glycine) and their distribution within cellular compartments was developed by Lechene and coworkers.[167, 168] Furthermore, high-resolution imaging analyses of solid-supported lipid membranes including quantitative information on the membrane composition were executed.[169, 170] NanoSIMS studies with cultured osteoblasts, rat thyroids, mouse lung melanoma and humans cancer cells (HeLa) show impressive ultrastructural details via elemental distributions within the cells.[171]

Due to the high lateral resolution along with high transmission and mass resolution dynamic SIMS is particularly suitable for the detection of small amounts of elements in tissues. The high amount of fragmentation and mostly elemental detection are beneficial for the localization of nanomaterials in tissues. Consequently, several studies use these benefits to accomplish nanoparticle detection even at low secondary ion yields in tissues: Kempen *et al.* were able to successfully localize Au(60nm)/SiO_2(30nm) core/shell NP in human macrophages by NanoSIMS in comparison to SEM, though at a lower lateral resolution (NanoSIMS: 50 nm, SEM: 1 nm).[26] Georgantzopoulou *et al.* investigated the influence of different silver nanoparticles (primary sizes 20 - 200 nm) on aquatic organisms by NanoSIMS and could observe Ag NP passing through epithelial barriers.[28] Wilson *et al.* used Au NP (20-100 nm) labelled antibodies (*i.e.* immunolabelling) to locate influenza hemagglutinin on cell surfaces.[172] Angelo *et al.* developed a multiplexed method using antibodies tagged with isotopically pure elemental reporters for the indirect detection of many targets at the same time at less than 200 metal atoms per antibody[173]. By sequential NanoSIMS analyses lateral distributions of 10 antibodies could be followed over an area of several square millimetres. However, it has to be kept in mind that the drawback of this study is the high total measuring time of 99 h, which makes routine use difficult. It was pointed out that larger (nanoparticle) tags should drastically reduce measurement times. However, untargeted analysis of molecular information along with localization of nanomaterials is the ultimate goal for the analytical techniques in nanotoxicological studies. Extensive fragmentation and the limited number of detection channels (up to seven) as they are typical for NanoSIMS instruments are detrimental for this goal. However, the prerequisites of a soft ionization via a pulsed primary ion beam and the simultaneous detection over the complete mass range in the ToF analyzer are fulfilled and promote the use of ToF-SIMS for biological samples as shown in the following chapter.

4.1.2 ToF-SIMS on Biological Samples

ToF-SIMS is promising for the analysis of biological samples, due to the theoretically unlimited mass range of the ToF mass analyser. As examples for the detection of molecules with high *m/z* the peptides Cyclosporin A, Gramicidin A and Melittin were detected with monoatomic ions.[57] The peptide Angiotensin was successfully detected using gas cluster ion beams and monoatomic Cs.[174, 175] However, the detection of the intact molecular ions of proteins was only shown for small proteins, such as insulin and Cytochrome C at molecular weights of 5808 and 12327 Da by the use of low energy Ar-cluster ions.[176]

Due to the screening abilities of the ToF mass analyzer more comprehensive information of the sample under analysis can be acquired by ToF-SIMS. In general, the detection of (quasi-) molecular ions is desired to simplify unambiguous identification of the origin of the signal. Although this might not always be possible in ToF-SIMS, larger fragments than in NanoSIMS can be detected and thus enable the identification of the parent molecules. Additionally, the best lateral resolution is in the range of 30 nm and thereby similar to the NanoSIMS instruments.[85] ToF-SIMS analyses should enable the acquisition of valuable information on toxicological behaviour without prior knowledge of the exact composition, in particular for biological samples, in which the influence of the nanomaterials on its surroundings is the target of the studies.

Consequently, ToF-SIMS is extensively used for the characterization of lipids and further components of membranes.[177-182] Initially applied to model membranes (*e.g.* Langmuir-Blodgett lipid monolayers[183, 184]; surfactant- and protein-containing membranes[185, 186]) ToF-SIMS has also been used for the imaging analyses of membrane components in tissue and individual cells[187, 188]. ToF-SIMS provided insights into the domain formation of unlabelled lipid membranes along with relative concentrations of the lipids by a high-resolution imaging analysis of a lipid monolayer.[183, 189] Furthermore, phase separations could be observed via ToF-SIMS between lipids in lung models membranes containing surfactant proteins as well as surfactants.[185, 186, 190] In a publication by Ostrowski *et al.* the mating behaviour of *Tetrahymena* was enlightened by ToF-SIMS indicating changes in the amounts of high and low-curvature lipids supporting the overall membrane deformation at the points of contact.[191] Discrimination of different bacteria and yeast types was facilitated by ToF-SIMS based on the surface lipid composition of the membranes.[192-194] Several direct analyses of mouse brain tissue sections by ToF-SIMS were conducted, which the distribution of important brain lipids. Among the detected species were sulfatides, inositoles, ceramides, cholesterol and peptide fragments. [195-198] Due to the important role of lipids in several diseases ToF-SIMS analyses have emerged as an exciting screening tool. A recent review summarizes the diverse capabilities of ToF-SIMS for lipidomic disease studies.[199]

4.1.2.1 3D Imaging

For 3D Imaging two main approaches are used. On the one hand, the propagation into the depth of the samples is facilitated by either sectioning of the samples prior to analysis or by using a focused ion beam (FIB) to gradually mill the sample to the desired depth before each analysis cycle. On the other hand, sputter erosion is performed in situ by the sputter beam.

Studies using the first approach utilize sectioning approaches: By sectioning of a sample via a microtome, followed by imaging analysis and recombination of the data afterwards, Fornai *et al.* demonstrated a 3D image of a rat heart composed of 40 individual sections in 2012.[200] The FIB approach uses a focused ion beam of Gallium ions with a high current to erode material and uses the ToF-SIMS for imaging of the sample. Szakal *et al.* milled the top of HeLa cells and imaged the distribution of phosphocholines, Na and several other components with sub-cellular resolution.[201]

Studies using the second approach use the depth profiling (sputter) beam for the erosion of the sample. With the emerging cluster sputter guns several studies employing C_{60} cluster ion guns for soft sputtering allowed the analysis of the 3D distribution of biomolecules within cells. Analyses of the amino acids and phospholipids distribution within normal rat kidney (NRK) cells revealed the 3D structure within the cells.[202] Another example shows the 3D-distribution of phosphocholines, and cholesterol along with further cellular substances within a frog oocyte.[203] Human cancer cells (HeLa) were analyzed for their 3D composition after incubation with a nucleus marker substance at submicron resolution.[204] Though often beneficial, cluster sputter ions are not mandatory for these analyses. Jung *et al.* used an O_2^+ sputter beam to erode plant cell walls and record the 3D distribution of lignin and cellulose.[205]

4.1.2.2 ToF-SIMS Detection of Nanomaterials in Tissues

Draude *et al.* used a combined ToF-SIMS and laser SNMS approach for the detection of peptide-coated 20 nm Ag nanoparticles and their effects in human macrophages. Silver was hardly detectable by ToF-SIMS, due to the low sensitivity to metallic silver. Instead, organic fragments of the cell membranes were detected. The much higher secondary ion yield for Laser SNMS enabled the detection of nanoparticles as well as Ag agglomerates with 3-7 µm diameters.[206] However, Kollmer *et al.* localized 50 nm Ag nanoparticles within MDCK II (Madin-Darby Canine Kidney II) cells at pixel sizes of 25 x 25 nm² by ToF-SIMS analyses.[85] Small Ag NPs (5-10 nm) were found to induce cell stress and uptake in primary human mesenchymal stem cells (MSC) and osteoblasts (OB).[207] Angerer and Fletcher analyzed the 3D distribution of TiO_2 nanoparticles in the freshwater protozoa *tetrahymena pyriformis*. They detected the nanoparticles in the food vacuoles of the organism. However, the nanoparticles exhibited a much lower sputter rate, which led to detection of nanoparticle signals even after the erosion of the cells in the top layers of the substrate.[208] Hagenhoff *et al.* detected unlabelled SiO_2 nanoparticles in NRK cells with diameters as small as 150 nm.[209] Lee *et al*. used a ToF-SIMS + CLSM (confocal laser scanning microscopy) analysis approach for toxicological studies of ZnO nanoparticles in HaCaT cells and located the ZnO inside the cytoplasm and at higher concentrations even inside the nuclei.[210]

In conclusion, only few approaches using ToF-SIMS for the detection of nanoparticles in biological tissue are known. The full potential of this promising technique for a sensitive and reliable detection without labelling was barely investigated. In particular, the application of ToF-SIMS to nanoparticle imaging in the challenging lung tissue at high lateral and mass resolution was not reported in detail before.

Chapter 5

Detection of Fe/Si Mixed Oxide – Core/Shell Nanoparticles in Lung Tissue

Based on:

L. Veith, A. Vennemann, D. Breitenstein, C. Engelhard, M. Wiemann, B. Hagenhoff, Distribution of Paramagnetic Fe_2O_3/SiO_2-Core/Shell Nanoparticles in the Rat Lung Studied by Time-of-Flight Secondary Ion Mass Spectrometry: No Indication for Rapid Lipid Adsorption, *Nanomaterials* **2018**, 8(8), 571.

5. Detection of Fe/Si Mixed Oxide - Core/Shell Nanoparticles in Lung Tissue

5.1 Introduction

Amorphous silica (SiO_2) is among the most widely used industrial nanomaterials, which can be found in products such as tires, plastics, and lacquers. It is also used as a food additive to prevent clogging or to ensure fluidity [7]. The high abundance of SiO_2 nanomaterials in everyday life products may lead to an increased exposure of humans to this type of nanomaterial. With respect to the workplace situation, the lung is a major route for a non-intentional uptake of SiO_2. In contrast to crystalline silica (quartz and cristobalite), which elicit inflammation and progressive fibrosis in the lung, effects of amorphous silica appear to be confined to a transient inflammation of the lung, even at comparably high doses [119, 211]. With respect to the mode of action, it is important that amorphous silica nanomaterials have a large specific surface of up to several hundred square meters per gram. It has been shown that the inflammatory effect of amorphous silica on the lung and also the cytotoxic effect on macrophages increases with surface size [212]. Of note, the inflammatory effect of colloidal SiO_2 can be reduced by surface coating with amino or phosponate residues [213, 214]. Since these surface coatings have no major influence on particle size or agglomeration behavior of the SiO_2 nanoparticles, it is highly likely that the inflammatory effects of SiO_2 on the lung involve an early interaction with biomolecules accessible in the lung micro-milieu. The analysis of biomolecules interacting with the surface of silica nanomaterials under in vivo conditions is, therefore, of pivotal interest.

Nanosized SiO_2 particles, which are deposited alongside the alveolar wall, most likely bind to molecules of the lipid-rich pulmonary surfactant and/or the protein containing hypophase underneath [15]. The pulmonary surfactant covers the inner surface of lung alveoli and reduces the surface tension. It is a thin layer mainly composed of (phospho-) lipids (90% by mass), with phosphatidylcholine being a major component [215]. The lung surfactant also contains specific surfactant proteins, some of which (*e.g.*, SP-A) may bind to bacteria and, therefore, contribute to the first line of defense against invading microorganisms [216]. The lung surfactant is produced by type-2 epithelial cells and are stored in lamellar bodies. Upon secretion of lamellar bodies, the surfactant spreads and self-organizes as a monolayer whose non-polar lipids chains are directed towards the alveolar space [215].

Considering the spatial organization of surfactant components and the fact that nanoparticles bathed in biological fluids such as plasma rapidly acquire a protein corona [217], it is reasonable to assume that SiO_2 nanoparticles, once deposited inside alveoli, form a corona, which, at least in vitro, can be composed of surfactant lipids and/or proteins [218]. However, because non-polar (phospho) lipid residues are facing the alveolar space, the corona of biomolecules formed around polar SiO_2 nanomaterials under in vivo conditions has not been investigated and may be different from the corona attracted by non-polar nanoobjects such as carbon nanotubes [219].

The analysis of the protein corona formed around NP inside the lung is a challenging task. However, isolation of protein-laden nanoparticles (NP) would be easier, if NP could be rapidly isolated from the broncho-alveolar lavage fluid, freed from cells and non-bound components, and eventually be analyzed for their protein corona. A tempting tool for this task is paramagnetic Fe_2O_3/SiO_2 core/shell nanoparticles (Fe-Si-NP). While their maghemite iron (Fe) core allows for a rapid magnetic isolation, their shell is composed of amorphous SiO_2, to which biomolecules can bind. In this investigation, we explored commercially available paramagnetic Fe-Si-NP for the purpose of analyzing the protein corona in vivo. The main questions were: (i) How are Fe-Si-NP distributed in the lung if they are applied via intratracheal instillation? (ii) Is the SiO_2 shell stable under the conditions of the lung? (iii) Are there any hints for a binding or accumulation of surfactant (phospho) lipids?

To answer all these questions with a single investigation, we applied Time-of-Flight secondary ion mass spectrometry (ToF-SIMS) to sections of Fe-Si-NP-laden rat lungs. ToF-SIMS is an ideal technique to detect inorganic as well as organic materials with detection limits in the femtomole range. A lateral resolution down to 30 nm may be reached and the technique has recently been shown to unambiguously detect SiO_2 nanomaterial in lung tissue [220]. Here, we detect Si, Fe and PC by mass spectrometry in a three-dimensional approach. Regions of interest were identified by light microscopic techniques such as enhanced dark-field microscopy, and incident light microscopy. The results of this study confirm our assumption that Fe-Si-NP are a useful tool to describe the early process of protein corona formation in the lung.

5.2 Experimental Section

5.2.1 Particle Characterization

The Fe-Si-NP were purchased from Kisker Biotech GmbH, Steinfurt, Germany (order No. PMSI-H.25–5). According to manufacturer, particles are composed of a maghemite Fe_2O_3 core and an amorphous SiO_2 shell and had a surface area of 50 m^2/g, according to the Brunauer–Emmet–Teller (BET) method. To further characterize particle size and shape by transmission electron microscopy (TEM), we dried 0.5 µL of the aqueous suspension, as used for intratracheal instillation (6 mg/mL H_2O), onto carbon-coated copper grids. TEM analysis was carried out with a Tecnai G2 (ThermoFisher Scientific, Waltham, MA, USA). The size distribution of these aggregates (in H_2O) was measured with a NanoSight LM10 instrument equipped with a green laser (532 nm), an Andor CCD camera, and NTA software 2.1 (Malvern Instruments GmbH, Herrenberg, Germany).

5.2.2 Sample Preparation and Animal Experiments

Fe-Si-NP were diluted with sterile distilled H_2O to a concentration of 6 mg/mL and ultrasonicated with a probe (VibraCell^{TM}, Sonics & Materials, Danbury, CT, USA) adjusted to 50 W (20 kHz) for 10 s. This suspension was used as the final instillation fluid.

Animal experiments were conducted at the animal facility of the University Clinics of Münster, Germany, and ethically approved by LANUV (Dortmund, Germany, Accession No. 84–02.04.2022.A157). Female Wistar rats (Charles River Laboratories, Sulzfeld, Germany), weighing 200–220 g, were maintained at a 12 h lights-on lights-off cycle; food and water were provided ad libitum. To administer Fe-Si-NP into the lung, animals were briefly anaesthetized with isoflurane and intratracheally instilled with 500 µL of instillation fluid containing 3 mg (*w/v*) Fe-Si-NP using a Penn Century Microsprayer. After 30 min, rats were deeply anaesthetized with ketamine/xylazine and bled via the descending aorta. A cannula was inserted into the trachea and the lung was lavaged five times with 5 mL 0.9% NaCl, to obtain lavage fluid for an accompanying investigation (data not included). Thereafter, the lung was inflated with 5 mL Cryomatrix (Thermo Shandon Ltd., Runcorn, UK), resected, snap frozen in liquid nitrogen, and stored at −80 °C for histological studies. Transverse sections were cut from the hilar region of the left lung with a cryo-microtome (HM 500, MICROM International GmbH, Walldorf, Germany). For

ToF-SIMS analysis, 7 µm thick sections were dried onto ITO-coated glass slides (Sigma Aldrich, Germany) and stored at −20 °C to investigate Fe-Si-NP. Of note, the lavage procedure as carried out here leaves a considerable number of *e.g.*, cells (>70%) within the lung parenchyma [221]. The same is true for particles attached to the alveolar walls as shown below.

5.2.3 Enhanced Dark-Field Microscopy

Enhanced dark-field microscopy (DFM) makes use of highly intense white light and allows to visualize particles and NPs in cells and tissues with strong light scattering properties down to a size of 20–30 nm. To apply the technique, air-dried cryo-sections were fixed in formaldehyde for 10 min, washed in phosphate buffer and cover-slipped using an aqueous mounting medium (Shandon Immu-Mount, Thermo Fisher Scientific, Bremen, Germany). Sections were viewed with an upright microscope (Olympus BX51) and digital bright-field images were captured using a RETIGA 2000R camera (Q Imaging, Surrey, Canada). Areas of interest were then imaged with a DFM microscope, equipped with a 40-fold UPlanApo Oil Iris objective (Olympus, Hamburg, Germany), and a CytoViva enhanced dark-field condenser. All DFM components were purchased from CytoViva, Inc. (Auburn, AL, USA).

5.2.4 Topographic Analysis

DFM imaged slides were cautiously immersed and rinsed in H2O to remove the coverslip and embedding medium, respectively. The sections were air-dried again and analyzed with an optical profiler instrument (PLu neox, Sensofar-Tech, Barcelona, Spain). A 50-fold EPI-objective (numerical aperture: 0.80) was used to acquire images with a resolution of 768 × 576 pixels for the selected area. The corresponding dimensions of a single pixel are 330 × 330 μm^2, which corresponds to a pixel density of 3.03 pixels/mm. Up to 33 consecutive images were acquired at a focal distance of 0.2 µm by an automated routine. The image stack was converted into a single sharp image with ImageJ software using the extended depth of field plugin [222] or used to generate a topographic image using SensoScan software (Version 3.5.2).

5.2.5 ToF-SIMS Analysis

To confirm the chemical identity of the nanoparticles and their Fe/Si core/shell structure a droplet of the aqueous Fe-Si-NP nanoparticle suspension was dried onto aluminum foil. ToF-SIMS spectra were acquired in the spectrometry mode at a TOF.SIMS^5 (IONTOF, Münster, Germany) for the pre-characterization of the nanoparticles. The raster size was 120 × 120 μm^2 at 128 × 128 pixels. 25 keV Bi_3 ions were applied at an ion dose of 1.5×10^8 ions and a cycle time of 200 µs. The corresponding mass range reached from 1 Da up to 1650 Da.

Measurements using O_2 sputtering were performed using Bi_3 at 25 keV with an ion dose of about 2.2×10^{10} ions applied to an analysis field-of-view of 300 × 300 μm^2 with a pixel raster of 512 × 512 pixels. O_2^+ was used as a sputter ion at an energy of 1 keV. A total sputter dose of 8.0×10^{14} ions was applied to a sputter raster size of 700 × 700 μm^2. The delayed extraction mode in combination with non-interlaced sputtering was used at a cycle time of 80 µs resulting in a mass range from 1 Da to 550 Da. Three replicate analyses were conducted to assure the validity of the obtained data.

5.2.6 Correlation Analysis

Image processing was carried out with the FIJI distribution for ImageJ (National Institute of Health, Bethesda, MD, USA) [223, 224]. The colocalization threshold plugin was used for the colocalization analysis [225]. The image registration was executed with the Turboreg [226] plugin (Biomedical Imaging Group, EPFL Lausanne, Switzerland).

5.3 Results and Discussion

5.3.1 Electron Microscopic and ToF-SIMS Characterization of Nanoparticles

TEM analysis showed that Fe-Si-NP consisted of nanoparticles with a size of ca. 10–20 nm, which mainly formed larger aggregates (Figure 5-1, inset). Fe-Si-NP dispersed in H_2O showed two maxima at 168 nm and 228 nm, as analyzed with optical tracking analysis; mean and mode values amounted to 217.5 ± 7.8 nm and 190.3 ± 19.6 nm, respectively (Figure 5-1).

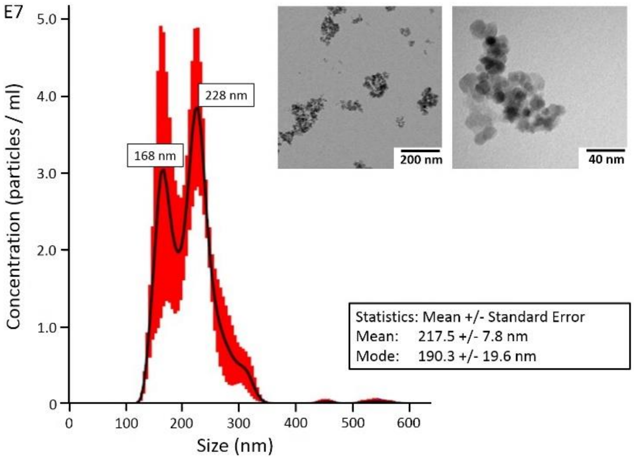

Figure 5-1: Size distribution of Fe-Si nanoparticles (Fe-Si-NP) in aqueous suspension as used for intratracheal instillation. Measurements were carried out by NanoSight optical tracking analysis. The inset shows electron microscopic images of Fe-Si-NP as typically found in the instilled suspension.

The mass spectrum, as revealed by ToF-SIMS, shows several prominent Si- and Fe-containing species (Figure 5-2), from which ^{28}Si$^+$, ^{30}Si$^+$, ^{54}Fe$^+$, ^{56}Fe$^+$ and ^{56}FeOH$^+$ were selected as relevant secondary ions for the detection of Fe-Si-NP in lung tissue sections. Besides the often detected hydrocarbons [227], B$^+$, Na$^+$ and Ca$^+$ were detected with notable intensities and these substances are most likely associated with the particle production process.

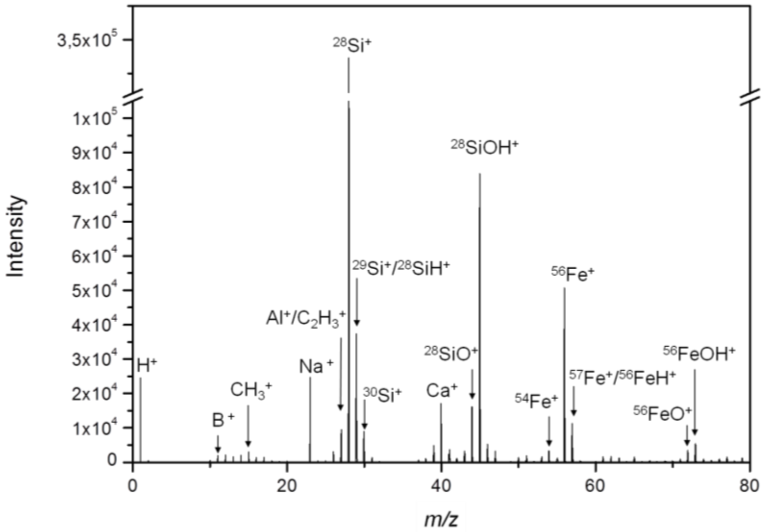

Figure 5-2: Mass spectrum of the Fe-Si-NP with a Fe/Si core/shell structure. Particles were deposited on an aluminum substrate and analyzed by ToF-SIMS. The particle components Si$_x$O$_y$H$_z$$^+$ and Fe$_x$O$_y$H$_z$$^+$ and their respective isotopes are detected along with hydrocarbons (CH$_3$$^+$ and C$_2$H$_3$$^+$), substrate components (Al$^+$), and other residues possibly linked to the production process (B$^+$, Na$^+$, and Ca$^+$).

While the findings illustrate the need for an extensive pre-characterization of nanoparticles before their use in toxicology studies, they also indicate several characteristic secondary ions ($^{28}Si^+$, $^{30}Si^+$, $^{54}Fe^+$, $^{56}Fe^+$, and $^{56}FeOH^+$) that can be used for the detection of the nanoparticles in the tissues.

The presence of Fe upon primary ion bombardment suggests that the ToF-SIMS information depth might be greater than the thickness of the Si shell. This finding can be explained by the highly energetic primary ion beam, which induces significant amounts of damage to nanoparticles and sometimes may even disrupt the particle. Sandoval et al. found an increased secondary ion yield for nanoparticles compared to bulk materials [228]. Increases in the secondary ion yield are always to be expected from nanoparticles depending on their sizes, because they have a larger surface area than bulk materials. However, the performance of the collision cascade is affected, if the size of the particles is in the same order of magnitude as the collision cascade. Obviously, this can also lead to increased intermixing of the particle components. Yang et al. observed a deformation of nanoparticles upon ion bombardment [229], which could also explain the simultaneous detection of core and shell components observed here for Fe-Si-NP. In any case, the simultaneous detection of the Si and Fe signals without the need for sputtering was beneficial for the detection of the core/shell particles in the tissue.

5.3.2 Inspection of Fe-Si-Laden Lung Tissue by Light Microscopy

Light microscopic techniques are increasingly used to detect nanoparticles in tissue sections [92]. Especially enhanced dark-field microscopy can detect light scattering particles down to a size of 20–30 nm [96]. Furthermore, metallic or metal oxidic nanoparticles often have plasmonic, reflective and diffractive properties, which allow for their differentiation against translucent tissue [230], or, in ideal cases, for identification via hyperspectral imaging [98]. Here, bright-field microscopy combined with DFM was used to localize Fe-Si-NP in the lung tissue prior to ToF-SIMS analysis.

Although the microscopic detection of SiO_2 nanomaterials in tissue sections is hampered by low optical contrast, the iron core of Fe-Si-NP caused a “rust”-like color facilitating the identification of larger agglomerates in bright-field images (Figure 5-3A–F). DFM confirmed this distribution but additionally revealed smaller yellow or blue dots in, or attached to, the hardly light scattering tissue structure (Figure 5-3C,D). Although the detection of nanoparticles in tissues by DFM is generally a straightforward approach, it is obvious that any light scattering inhomogeneity might lead to misinterpretation.

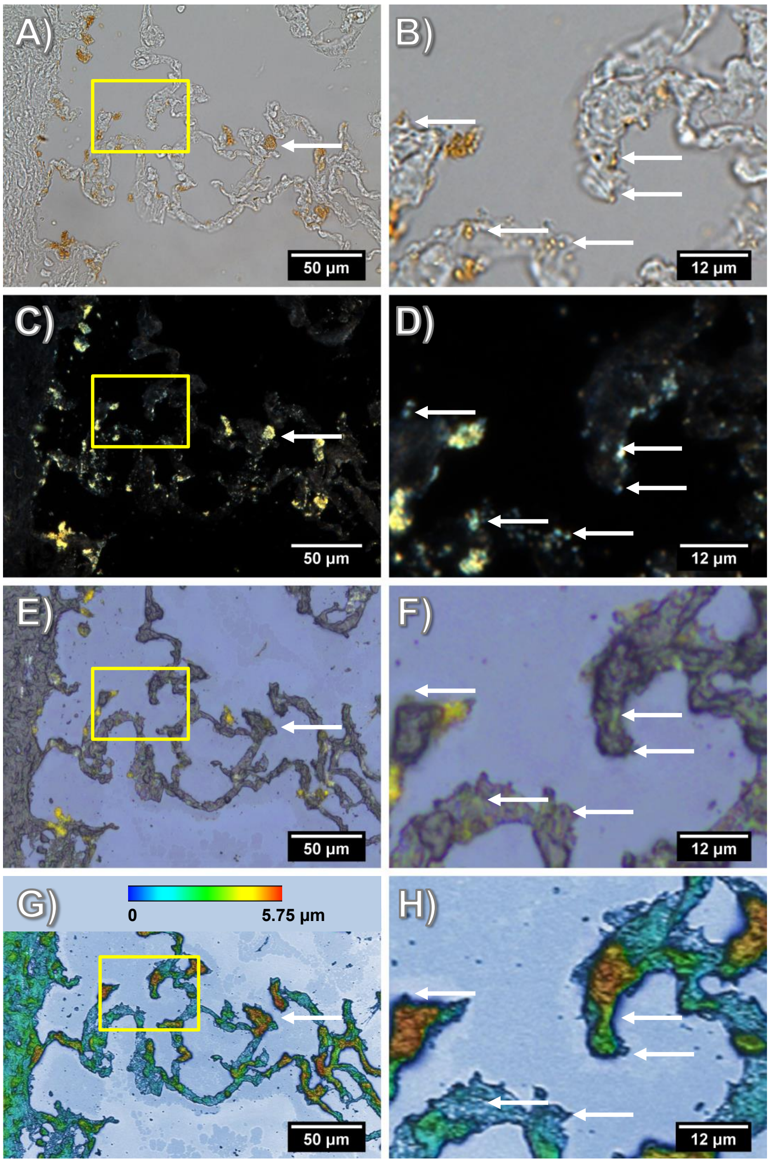

Figure 5-3: Light microscopic analyses of a Fe-Si-NP-laden cryo-section from rat lung. Overview (A,C,E,G) and detail (B,D,F,H) of the boxed area shown on the left. (A–D) Routine images of the coverslipped section taken with bright-field optics (A,B) and DFM (C,D); Fe-Si-NP agglomerates appear as brownish patches at alveolar septa or in macrophages. With DFM, additional small light-scattering particles are seen alongside alveolar septa. (E–H) Same tissue area after removal of the coverslip, rinsing and drying. (E,F) Microscopic image of the dry section without coverslip, taken with a reflective light microscope. Prominent Fe-Si-NP agglomerates are still identifiable as yellow patches. (G,H) Optical profilometry analysis showing the relief structure of the dry lung section as subjected to ToF-SIMS; the topographic map reveals an amplitude of several micrometers. Arrows in (A,C,E,G) point to a particle-laden macrophage (A,C), which became lost in the course of tissue preparation. Similarly, arrows in (B,D,F,H) point to small Fe-Si-NP (seen in B,D), which were absent after drying.

Bright-field microscopy and DFM demand that the tissue section is immersed in ringer solution, coverslipped and viewed with oil-immersion lenses. As ToF-SIMS analysis is carried out under vacuum conditions, the coverslip has to be cautiously removed and the sections needs to be dried. Mild shearing forces and washing steps are indispensable during this procedure and may influence the signals gathered from particles in the subsequent ToF-SIMS analysis. To show these effects, reflective light microscopic images were taken at the same position of the dried section.

Reflective light microscopic images have a lower optical resolution but are highly useful to visualize the structure of a section prepared for ToF-SIMS analysis. Here, it is shown that numerous large yellow spots (up to 15 µm) previously seen in the bright-field or DFM image were still in place, whereas others structures, which were interpreted as Fe-Si-NP filled macrophages, were no longer visible (Figure 5-3E,F; white arrows). Similarly, smaller particles (<3 µm), which are marked by arrows in the magnified bright-field and DFM images (Figure 5-3B,D), were not seen on reflective light microscopy images.

As ToF-SIMS analysis makes use of sputtering and ion bombardment, which is applied under a certain angle, the relief structure of the dried tissue section will unavoidably influence image resolution. Figure 5-3G,H shows the relief of the dried tissue on the indium tin oxide (ITO)-coated glass substrate, as analyzed by profilometry. The height of the formalin-fixed and afterwards dried alveolar septa on the substrate ranged 2.5–5.25 µm, which was 36–75% of the initial thickness of the cryo-section (7 µm) and may be explained by evaporation of H_2O prior to immersion fixation. Although the nature of the highest peaks remains unknown, these sites do not contain agglomerated Fe-Si-NP, which were mainly found in areas ranging in height from 2–3.5 µm.

In summary, the combination of several microscopic methods showed that Fe-Si-NP were distributed alongside the alveolar wall or were contained in macrophage-like structures. The successive observation by DFM and ToF-SIMS may lead to a loss of Fe-Si-NP containing structures and this has to be considered when both images are compared (see below).

5.3.3 ToF-SIMS Detection of Nanoparticle in Tissue – Localization

In the next step, we tested the intactness of the Fe/Si core/shell in the tissue using both the Fe- and Si-signal distributions in the ToF-SIMS analysis. A sputter erosion with 1 keV O_2^+ ions was necessary to analyze the complete depth of the sample section.

The tissue structure of the lung with all its alveolar septa, as shown in Figure 5-3, was properly reflected by the CH_4N^+ signal, which is a typical fragment of amino acids and, thus, indicates the position of fixed proteins (Figure 5-4A). Due to the relatively harsh sputtering conditions of 1 keV O_2^+ ions, only few organic molecular species were preserved. Nevertheless, the lateral distribution of the signal at *m*/*z* 184.07 could be summed up over the whole depth of the analysis. This fragment is indicative of the phosphocholine head group $C_5H_{15}NPO_4^+$ and most likely attributable to phospholipids previously located in cell membranes and/or in the pulmonary surfactant. A minor fraction of the signal was found in alveolar spaces (Figure 5-4B), suggesting that it was transferred onto the substrate during the preparation process.

With respect to Fe, several relevant signals (besides the main isotopes $^{54}Fe^+$ and $^{56}Fe^+$) were identified in the spectrum of both, the isolated and the lung-incorporated Fe-Si-NP (Figure 5-2). Of note, further iron-related species with the same lateral distribution were found, *e.g.*, $^{56}FeOH^+$, $^{54}FeOH^+$, and $^{56}Fe_2O^+$, proving that the signals were correctly assigned to all Fe species. In any case, the lateral signal distribution of the main Fe isotopes $^{54}Fe^+$ and $^{56}Fe^+$ (Figure 5-4D,E) was largely congruent with the distribution of Fe-Si-NP in the tissue (Figure 5-3C,E). This is particularly obvious for some larger areas with diameters of up to 15 µm (Figure 5-4D,E), but also for numerous smaller and less intense Fe patches. As most of these areas have a diameter larger than 200 nm, they most likely represent Fe-Si-NP agglomerates.

Colocalization with the CH4N+ signal (Figure 5-4C) shows that the majority of Fe signals (green) in the range of 3–10 µm was localized alongside the alveolar septa (red), which is in accordance with the microscopic results of Figure 5-3 and was expected due to the short incubation time of only 30 min. Some of the smaller Fe-signals (green) were colocalized with the epithelium and might be interpreted as to be incorporated by the epithelial cell. However, due to the preparation steps of the lung prior to fixation (filling with cryomatrix, freezing, sectioning, and drying) and to the relief structure of the tissue (Figure 5-3G), a precise cellular localization of particles cannot be made by light microscopy or ToF-SIMS. A study by Shon et al. carried out on air-dried unfixed macrophages laden with dimercaptosuccinic acid-coated Fe_3O_4 nanoparticles succeeded in localizing particles in the cytoplasm [231]. Phosphatidylcholine components in that study were detected as specific $C_4H_7^+$ ions only.

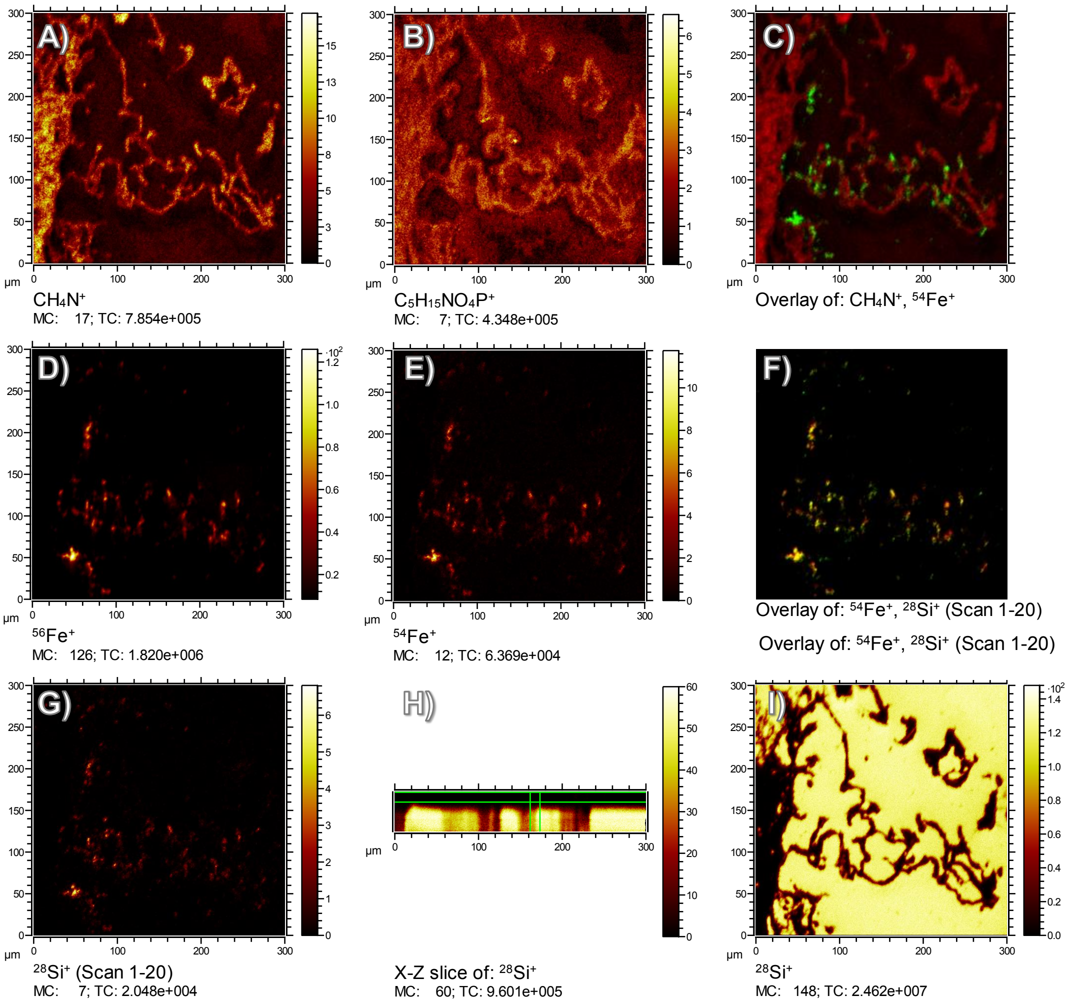

Figure 5-4:ToF-SIMS signal distributions of organic and inorganic components in a Fe/Si core/shell nanoparticle-containing lung tissue section 30 min post intratracheal instillation of particles. (A) CH_4N^+ indicative of proteins to show tissue distribution and lung structure. (B) $C_5H_{15}NPO_4^+$ is the phosphocholine (PC) head group fragment showing the distribution of lipids of lung tissue and surfactant; PC signal seen in the alveolar space is interpreted as to be artificially dislocated during filling of the lungs with cryomatrix. (C) Overlay of $^{54}Fe^+$ (green) and CH_4N^+ (red) signal showing Fe-Si-NP distribution in lung tissue. (D) $^{56}Fe^+$, and (E) $^{54}Fe^+$ distributions of Fe-Si-NP particles. Small and large agglomerates appear alongside the alveolar walls. (F) The overlay of $^{54}Fe^+$ (D, red) and $^{28}Si^+$ (G, green) reveals the colocalization of both particle-related signals. (G) ToF-SIMS signal distribution of Si species from the topmost layers as indicated by the horizontal green lines in the X-Y slice of the ToF-SIMS dataset in (H). (I) $^{28}Si^+$ signal distribution integrated for the complete depth including the indium tin oxide-coated glass slide.

5.3.4 Colocalization of Fe and Si in Lung Tissue by ToF-SIMS

With respect to the simultaneous identification of Fe and Si, isobaric interferences may occur due to the similarity of the theoretical mass of $^{56}Fe^+$ (*m*/*z* 55.934939) and $^{28}Si_2^+$ (*m*/*z* 55.953854). This hampers a reliable distinction by mass, and only an improvement of mass resolution from the current R = 1500 to R > 3000 could solve this problem. However, the $^{54}Fe^+$ signal, although relatively weak, is not influenced by any Si cluster and, therefore, allows analyzing the Fe distribution unbiased from Si signals. Thus, adopting $^{54}Fe^+$ as a reference, it turned out that $^{56}Fe^+$ signals virtually showed the same distribution as did $^{54}Fe^+$. In addition, the $^{56}Fe^+$ signal was hardly influenced by $^{28}Si_2^+$ from any non-particle source and showed a low background intensity in tissue-free areas (Figure 5-4D,G). Due to the obvious correlation of the signal distributions for the $^{54}Fe^+$ and $^{56}Fe^+$ isotopes, we decided to use the $^{56}Fe^+$ ion to measure the distribution of Fe in lung sections.

To identify Si on the paramagnetic Fe core, any Si signal from the ITO-covered glass substrate had to be avoided. Therefore, the ^{28}Si signal was reconstructed from only the first 20 sputter/analysis cycles (*i.e.*, scans). The signal distribution obtained by this was highly similar to the Fe distributions (Figure 5-4G), indicating that the ITO layer had successfully shielded the underlying glass substrate against the analysis beam. In contrast, if the signal was summed up over all 81 cycles (compare X–Z slice in Figure 5-4H), the sputter cycles had eroded the ITO layer and the apparent $^{28}Si^+$ distribution reflected the underlying substrate in tissue-free regions (Figure 5-4I). Based on selected data evaluation and an isotopic signal distribution, the presence of Si on nanoparticles could be confirmed even in the positive ion polarity upon oxygen sputtering, as opposed to earlier studies using Cs sputtering and the negative ion polarity [220]. Consequently, the identification by ToF-SIMS of pure, unlabelled SiO_2 nanoparticles in tissue sections should be possible with this protocol, provided that any contamination, *e.g.,* with the widespread polysiloxanes, can be ruled out.

Another option to identify correlating distributions of Si and Fe species is the comparison of Fe isotope distributions with ^{30}Si, as oxide clusters of this ion cannot form signals with the same mass-to-charge-ratio as the Fe isotopes in the observed mass range. However, as ^{30}Si is also a part of the ITO shielded substrate, the same limitations as for ^{28}Si apply. Of note, the reconstruction of the less abundant $^{30}Si^+$ isotope ruled out that the $^{28}Si^+$ signal merely originated from $^{56}Fe^+$ (*m*/*z* 27.967470), which would partially interfere with the

$^{28}Si^+$ (*m*/*z* 27.976927), since both, ^{28}Si and ^{30}Si show the same signal distributions (not shown here).

Based on the comparison of Figure 5-4D,E (for Fe) and Figure 5-4G (for Si), the most important result is that the $^{28}Si^+$ distribution derived from the first 20 sputter/analysis cycles was properly colocalized with the Fe distributions, as is shown by the numerous yellow spots in Figure 5-4F, which result from red ^{54}Fe pixels overlaid with green ^{28}Si pixels. This demonstrates that the Si shell of the paramagnetic Fe particles is stable under in vivo conditions.

5.3.5 Correlation and Comparison of Dark-Field Microscopy and ToF-SIMS

Enhanced dark-field microscopy (DFM) detects NP down to a size of 15 nm [232] and was, therefore, used as a sensitive tool to visualize the Fe-Si-NP in tissue sections prior to ToF-SIMS analysis. Overall, the ToF-SIMS $^{54}Fe^+$ signal and the DFM signal showed a high degree of similarity (Figure 5-5A,B). Colocalization analysis of both signals using Pearson's correlation coefficient confirmed this high degree of co-localization. As this coefficient ranges from −1 (perfect anti-correlation) to +1 (perfect correlation), a value of 0.541 confirmed that a considerable number of pixels ($^{54}Fe^+$ positive by ToF-SIMS) correlate with the bright spots in the DFM image (Figure 5-5C). Of note, this result strongly suggests that ToF-SIMS had not detected false positive signals.

However, the correlation was not perfect and differences were observed for some larger dots (marked in Figure 5-5), most likely corresponding to particle-laden macrophages, but also for smaller particles seen in DFM. As outlined above, especially inappropriately fixed material may have become lost during preparation.

Other reasons may also account for such differences: Fe-Si-NP might not have been detected by ToF-SIMS due to insufficient sample erosion (false negative ToF-SIMS signals). However, as the sputtering with O_2^+ and subsequent analysis were extended into the depth of the substrate, it appears unlikely that the soft lung tissue shielded Fe-Si-NP and prevented the accumulation of supra-threshold signal intensities in the ToF-SIMS analysis. Rather, the accessible mass (*i.e.*, particle size and/or concentration) was too small, and a low signal did not reach the limit of detection. This appears unlikely for most of the Fe-Si-NP aggregates larger than 100 nm but may account for the 10–50 nm fraction of Fe-Si-NP, which is visible by TEM (Figure 5-1) and, at least in part, should be visible by DFM.

Finally, unlike the large brown agglomerates (Figure 5-3A,B), small objects can scatter light as well and may have been erroneously designated as Fe-Si-NP by DFM. Hyperspectral microscopy may be used to further identify such questionable structures.

In summary, the ion distribution measured by ToF-SIMS explains most of the DFM signals, thereby serving as a validation technique. However, DFM images contained several signals without any ToF-SIMS equivalent. These DFM signals were most likely caused by salt residues or tissue material and indicate that it is necessary to confirm the chemical identity of nanoparticles in DFM imaging studies.

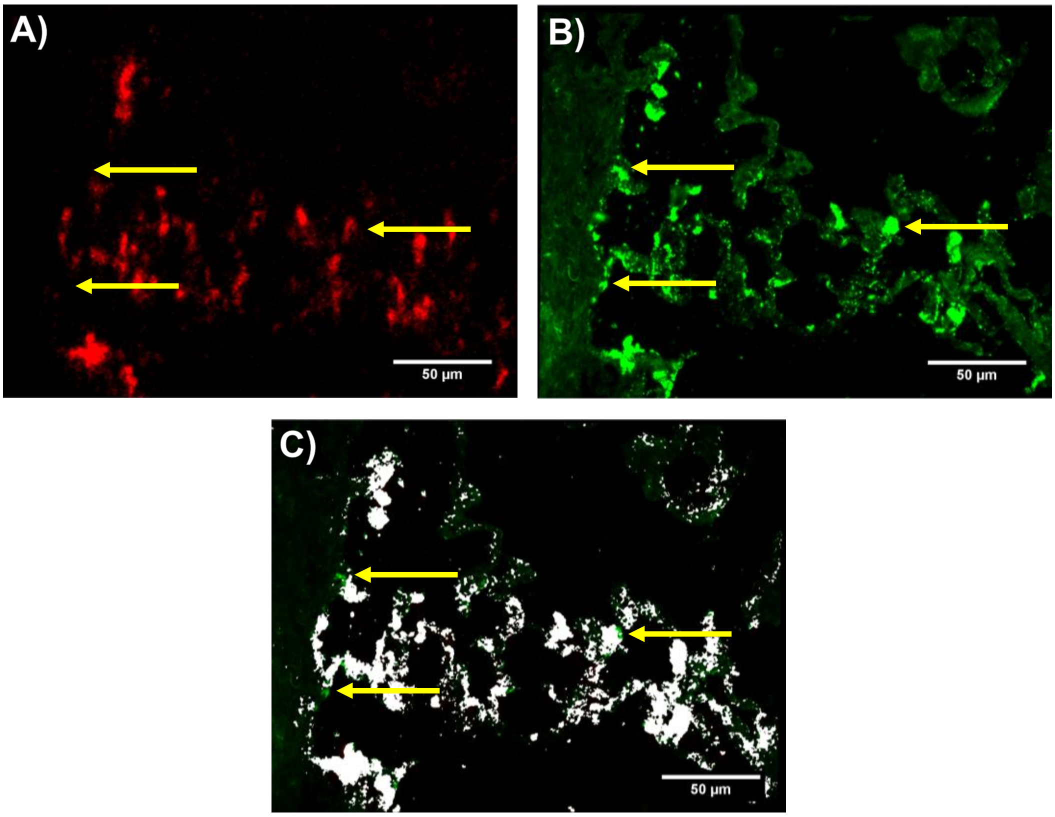

Figure 5-5: Comparison of ToF-SIMS $^{54}Fe^+$ signal distribution and dark-field microscopy (DFM) images. Image taken from Figure 5-3. (A) $^{54}Fe^+$ ToF-SIMS signal (red); (B) DFM signal (green) taken before washing and ToF-SIMS analysis; and (C) Colocalization of (A,B). A high degree of correlation is evident (white overlay). The Pearson correlation coefficient for this image was 0.541. Arrows point to green spots (B) which were detected by DFM, but not by ToF-SIMS.

5.3.6 Lack of Colocalization of Phosphatidylcholine with Fe-Si-NP and General Impact of Findings

In this study, most of the nanomaterial was found closely related to the alveolar septa by both optical and mass spectrometric techniques (Figures 5-3 and 5-4G). In addition, a partial uptake into macrophages was observed despite the relatively short incubation time of 30 min. The obviously persistent macrophage activity suggests that the intratracheal instillation of H_2O, which was used to favor the dispersion of the polar NP, has no negative impact on the micro-milieu of the lung. Nevertheless, larger agglomerates of Fe-Si-NP with diameters of several micrometers were found in the lung. These agglomerates may have formed upon contact with the lung lining fluid and/or during lymphatic retrieval of the aqueous suspension fluid. As such, an agglomeration of nanoparticles in lung instillation studies is common [233], although, *e.g.*, citrate-stabilized gold nanoparticles do not agglomerate under these conditions [234].

In any case, it appears plausible that Fe-Si-NP, which had a size of less than 200 nm (see Figure 5-1) when they were administered to the lung, may have come into direct contact with several well organized layers of biomolecules such as the lung surfactant, the hypophase, and/or the membrane of (epithelial) cells. It appears conceivable that this sequential arrangement of biomolecules and ions in the lung orchestrates the formation of the protein corona as well as agglomeration of NP. A protein corona, which can be artificially generated with different preparations of lung surfactant [218] may, therefore, differ from the native corona.

To monitor the putative binding of (phosho) lipids to silica nanoparticles in the lung, we compared the *m*/*z* 184.07 signal (representing phosphatidylcholine as the main constituent of pulmonary surfactant and cell membranes), with the distribution of Si, which forms the outer shell of the Fe-Si-NP: While the *m*/*z* 184.07 signal delineated the alveolar septal structure, and was also found on the ITO substrate at lower intensities, volumes occupied by the Si signal in the first 20 scans were completely free of PC (Figure 5-6, arrows). Although we are aware that the sensitivity of analytical methods can be improved, *e.g.*, by well-adapted sputtering methods, we conclude that there is no major accumulation of phospholipids on the polar surface of Si nanoparticles. We furthermore suggest that phospholipids, as constituents of the lung surfactant, are not involved in the formation of particle agglomerates.

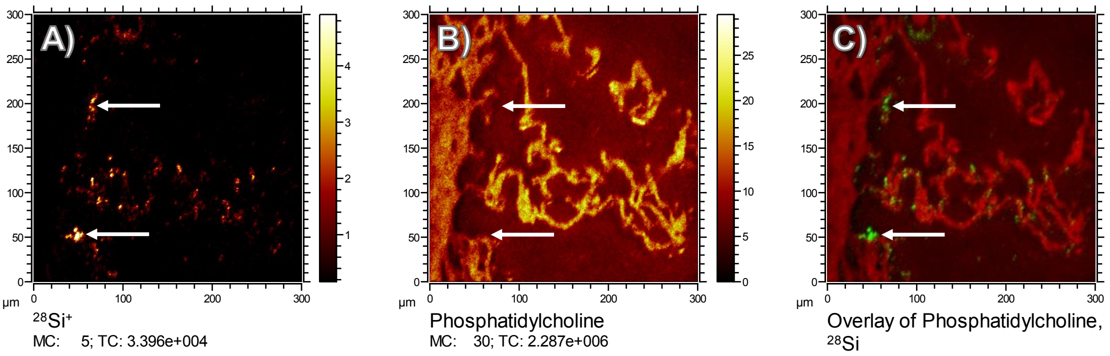

Figure 5-6: Comparison of the Si and phosphocholine distribution in a cryo-section of the rat lung 30 min post administration of Fe-Si-NP. All images contain information of the uppermost 20 scans only. (A) $^{28}Si^+$; (B) $C_5H_{15}NPO_4^+$, which is the 184.07 fragment of the phosphocholine (PC) head group showing the distribution phosphatidylcholine; and (C) the overlay of (A,B). Arrows in all images point to the position of larger agglomerates of Fe-Si-NP; note that in (B) PC is not detected at the indicated sites.

This finding seems to be in contrast to a recent investigation on lipid binding to SiO_2, ZrO_2, or AlOOH in vitro [218]. Using two different preparations of pulmonary surfactant, it was found that polar nanoparticles bind indeed to phospholipids, if the mixture (Curoserve®) contained surfactant protein A. However, the role of surfactant proteins for an in-situ opsonization of nanoparticles is still not known. As mentioned above, the incubation of nanoparticles in artificial or isolated pulmonary surfactant may be profoundly different from binding conditions in the lung. While in the lung the air–liquid interface carries non-polar lipid residues facing the gas phase, lipids in isolated lung surfactant may form micelles with their polar residues directed outwards.

The current results provide, for the first time, new and more realistic insights in the formation of the lipid/protein corona around silica nanoparticles under native conditions of the lung. Findings may be representative for pulverulent silica nanomaterials, unless they are coated, *e.g.*, by hydrophobic molecules. These findings have been achieved with high-resolution ToF-SIMS, a state-of-the-art bio-imaging method, which is universally applicable and circumvents the need to isolate particles from tissues. Future developments of the technique such as an ultra-high mass resolution detector are in sight, which may further increase the performance of the method [235]. This will allow us to obtain more detailed analyses of molecules bound to NP under in vivo conditions.

5.3.7 Methodical Considerations

It is well known that any type of tissue preparation may have an influence on bio-imaging results. As described before (5.3.2–5.3.4), tissue sections analyzed by ToF-SIMS were taken from lavaged lungs, which were filled with a cryomatrix and immediately snap-frozen in liquid nitrogen. Although filling with a cryomatrix preserves the tissue architecture of the lung, the compound does not fix subcellular structures, such that a reliable distinction between cell-attached and intracellular NP cannot be made. Furthermore, sections were cut, dried onto ITO slides, stored in a frozen state, and eventually fixed with formalin on the slide. We are aware that this procedure cannot prevent a partial loss of NP, especially if they are not in contact with fixable tissue components. However, numerous particles and agglomerates proved to be firmly attached, because even the withdrawal of the coverslip prior to ToF-SIMS analysis left the majority of particles in place, as shown in Figure 5-5.

There may also be a partial loss or wash-out of lipids, as these molecules are not fixable with formalin. However, neither ethanol nor other organic solvents were used, such that PC molecules remained highly abundant in all tissue structures. Nevertheless, there was a low background signal of PC in alveolar areas, which may be interpreted as an artificial displacement of PC. However, as levels of PC were low in the vicinity of the alveolar septa (Figure 5-6B), we assume that PC found within alveoli was not displaced from cellular structures. Rather, it may reflect a mixture of lung surfactant and liquid cryomatrix, which dried onto the ITO carrier. Considering all these facts, we cannot completely rule out that the lack of PC on Fe-Si-NP was partially artificial, but the complete absence of PC over all Si signals (see Figure 5-6C) makes this interpretation highly unlikely.

Finally, the lack of PC on Fe-Si-NP might also hint at an inappropriate sensitivity of the ToF-SIMS method. However, in a previous investigation on the composition of Langmuir–Blodgett films, PC and other phospholipids were successfully identified in a lung surfactant-like monolayer[186].

Thus, although some artificial displacement of particles and/or a loss of PC cannot completely be ruled out, we suggest that the absence of PC on the silica surface of the Fe-Si-NP in the lung, as measured by the highly sensitive ToF-SIMS method, is not an artefact and, therefore, of biological significance.

5.4 Conclusion

In this study on paramagnetic silica nanoparticles (Fe-Si-NP) administered to the lung via intratracheal instillation for 30 min, we show that particles were attached to alveolar walls and only marginally internalized by cells such as alveolar macrophages. Due to the successful colocalization of Fe and Si signals by ToF-SIMS analysis of lung cryo-sections, we conclude that the core/shell structure of the Fe-Si-NP remains intact under these conditions, such that Fe-Si-NP may now be used to study the early protein adsorption to a nanosized silica surface in the lung. Finally, the analysis of the phosphocholine head group, as a representative of phosphatidylcholine (PC), which is a major lipid of the pulmonary surfactant, revealed no augmented PC binding to Fe-Si-NP. This is an important finding as previous in vitro studies suggested that, *e.g.*, surfactant protein A could mediate the binding of phospholipids to the polar silica surface. In this respect, ToF-SIMS proved to be a valuable technique with high spatial resolution and appropriate limits of detection, which made it possible to analyze nanoparticles together with bound organic molecules within their cellular environment.

Chapter 6

Detection of Fluorescently Labelled Silica Nanoparticles in Lung Tissue

Based on:

L. Veith, A. Vennemann, D. Breitenstein, C. Engelhard, M. Wiemann, B. Hagenhoff, Detection of SiO_2 Nanoparticles in Lung Tissue by ToF-SIMS Imaging and Fluorescence Microscopy, *Analyst*, **2017**, 142, 2631-2639.

6. Detection of Fluorescently Labelled Silica Nanoparticles in Lung Tissue

6.1 Introduction

The increasing use of specially designed nanomaterials in consumer products and applications such as sunscreens (TiO_2) or food additives (SiO_2) in everyday life offers many advantages.[7, 8] However, a spread of nanoparticles into the surroundings during use of nanomaterial-containing products cannot always be avoided as it is the case from CeO_2 in diesel fuel or automotive catalysts.[236, 237] The lung has been recognized as one major entrance port for nanoparticles (NP) into the body. In particular, small nanoparticles, albeit at a low degree, may travel to remote organs and be redistributed to certain cell types.[16, 238, 239] A precise description of the distribution of nanoparticles in tissues with cellular resolution is therefore mandatory to fully explore the potential hazard or health risk of nanoparticles.[213]

Thin sections, mostly of paraffin embedded tissue, are widespread in histopathology studies and may be used for a wide range of microscopic examinations on the cellular or even sub-cellular level. For the detection and identification of nanoparticles in tissue sections several analytical techniques are available. Laser ablation inductively coupled plasma mass spectrometry (LA-ICP-MS) has the potential to detect low amounts of various elements and offers quantification via matrix-matched standards. Although a single particle detection mode may be applied for dilute samples, the methods' spatial resolution is currently limited to 1 µm.[25] Most elements can be detected but since speciation analysis is not possible its use for particles consisting of ubiquitous elements is limited. Ion beam microscopy (IBM) is a highly sophisticated method to achieve both, a high resolution and quantification of low amounts of nanoparticles in cells, but often needs special, or well-adapted sample preparation techniques and extensive instrumental efforts.[105] Scanning electron microscopy combined with energy dispersive X-ray spectroscopy (SEM-EDX) offers excellent lateral resolution in microscopy mode and features the possibility to identify materials via EDX but this mode usually suffers from a lower lateral resolution and a relatively low sensitivity. Conventional fluorescence microscopy (FM) or confocal scanning microscopy offer the opportunity to detect fluorescent nanoparticles along with other biological labels such as DNA-intercalating stains and/or antibody staining.[27] However, industrially relevant nanoparticles are rarely fluorescent and a post-hoc surface-labelling via a protein corona may alter their properties.[240] Raman microspectroscopy can differentiate some cellular components based on their functional groups, but has limitations in detecting unknown molecular compounds and identifying inorganic materials.[241] Secondary ion mass spectrometry based on a sector-field mass analyser (NanoSIMS) was successfully used for the detection of gold and silver nanoparticles in tissues due to its high lateral and mass resolution. However, the limited number of detection channels restricts the use for the detection of unexpected species as well as screening of unknown samples.[26, 28] All these techniques have in common that they hardly provide complementary information on the chemical composition of the cellular environment, especially in conjunction with the nanoparticle.

Preferably, a technique to detect the distribution of nanoparticles (composition not limited to a certain element) and associated compounds in tissue with high lateral resolution and high sensitivity (single nanoparticle level) should be available.

Time-of-Flight secondary ion mass spectrometry (ToF-SIMS) is still rarely used in the field of nanotoxicology, although it offers a great potential for these kinds of analyses due to its unique features. The possibility to distinguish between different chemical species via characteristic ions at a mass resolution of up to $R = 10{,}000$ along with the simultaneous detection of element and molecule ions over a wide mass range via the ToF analyzer offers a more complete analytical information of the area under investigation. This parallel mass detection in combination with a high sensitivity make ToF-SIMS especially suitable for the analyses of various different biological systems, *e.g.* for lipid analysis of brain sections, tissue studies, implant surface analysis, analysis of cholesterol distributions, and single cell analyses as recently reviewed.[32, 242] Besides surface spectrometry and high lateral resolution imaging (<100 nm), the operational modes include depth profiling and high-resolution 3D microanalysis modes.[188] A promising approach that allows to correlate ToF-SIMS images of small structures with microscopy techniques was recently published.[243] However, so far very few publications have dealt with the detection of nanoparticles in tissue sections by ToF-SIMS due to the limited availability of the technique and the required measurement times.[207-210, 243, 244]

In this study, we explore the usefulness of the ToF-SIMS technique as an analytical tool for the direct detection of nanomaterials in tissue sections. SiO_2 nanoparticles applied to rat lungs within a toxicity study were localized by ToF-SIMS at an early stage. SiO_2 nanoparticles are toxicologically relevant as they induce considerable inflammatory reactions in the lungs upon intratracheal instillation or inhalation.[119, 214] Most SiO_2 NP have a large surface area and a high binding capacity for biomolecules, which might be relevant for the interaction with the inner lung surface.[245] This makes their monitoring by surface sensitive ToF-SIMS studies worthwhile. Therefore, we started into such investigations by validating the ToF-SIMS localization of fluorescent SiO_2 nanoparticles by light microscopy. Results prove the usefulness of ToF-SIMS for direct nanoparticle detection and offer an enhanced reliability for the evaluation of future nanoparticle analyses in tissues.

6.2 Experimental Section

6.2.1 Nanoparticles

SiO_2 FITC nanoparticles, which had been prepared according to a modified Stöber method and characterized beforehand, were used in this study.[246, 247] The characterization resulted in mean particle sizes as measured by TEM and analytical ultracentrifugation of $d_{50} = 25$ nm and $d_{90} = 28$ nm. The BET surface was 178 m^2/g. The surface analysis by X-ray Photoelectron Spectroscopy resulted in a composition of $O_{63}:Si_{29}:C_8$. The isoelectric point in H_2O was 3.5 and the zeta-potential at pH 7.4 amounted to -39 mV. There was no indication for agglomeration and/or precipitation in a 9+1 mixture of 0.9% NaCl and phosphate-buffered-saline, which was used as the instillation fluid (IF). The SiO_2 FITC nanoparticles are considered to be very similar to pristine SiO_2 nanoparticles regarding their physicochemical properties (size, BET surface, zeta-potential, surface composition)[248] as well as their toxicological behaviour and, therefore, are used here as surrogates for SiO_2 nanoparticles[214].

6.2.2 Animal Experiments and Lung Tissue Preparation

All animal experiments were carried out in the animal facility at the University Clinics of Essen, Germany, and were ethically approved by local authorities (LANUV, Dortmund, Germany). Young female rats weighing 200-250 g (Wistar strain WU) were purchased from Charles River Laboratories (Sulzfeld, Germany) and maintained with a 12 h lights-on lights-off cycle. Food and water were provided *ad libitum.* SiO_2 fluorescein isothiocyanate (FITC) nanoparticles (2.4 mg/ml) were freshly suspended in the instillation fluid (see above) by a 10 s lasting ultrasonication treatment using a 3 mm sonifier probe (VibraCell, Sonics & Materials, Newtown, CT, USA) operated at 50 W. Animals were briefly anaesthetized with 5% isoflurane in air and a total of 1.2 mg (w/v) SiO_2 FITC in 500 µl IF was intratracheally instilled under visual control. To increase the even distribution inside the lung a microsprayer (PennCentury, Wyndmoor, PA, USA) was used. Rats were deeply anaesthetized 3 h post instillation with a mixture of Ketamine and Xylazine and bleeded via the *Aorta descendens*. A cannula was inserted into the trachea and the lung was inflated with 5 ml cryomatrix (Thermo Shandon Ltd., Runcorn, UK). The left lung was immediately resected, snap frozen in liquid nitrogen and stored at -80°C until further processing. Transverse sections from the hilar region (7 µm) were cut with a HM 500 cryomicrotome (Microm Intl. GmbH, Walldorf, Germany), and dried onto indium-tinoxide (ITO)-coated slides (Sigma-Aldrich, Taufkirchen, Germany) with a surface resistivity of 70-100 Ω. Sections were stored at -28 °C and transferred in the frozen state into the loadlock of the ToF-SIMS instrument. After evacuation to 0.2 mPa for about 30 min the samples were analyzed.

6.2.3 Analysis by Bright-Field and Fluorescence Microscopy

Sections were viewed with an inverted fluorescence microscope IX51 (Olympus, Tokyo, Japan), equipped with a 20x objective and conventional filter sets appropriate for FITC. Regions of interest bearing considerable quantities of fluorescent nanomaterials were identified and fluorescent images were taken with a DVC CCD camera, which was part of a Nikon Lucia system. Regions of interest were macroscopically labelled with copper grids on the backside of the slide fixed to the stage of light microscope and transferred to the ToF-SIMS instrument. Digital fluorescent images were enhanced in contrast and a green background value observed in tissue-free alveolar spaces was subtracted. By this procedure, the weak green autofluorescence of the tissue upon illumination with 490 nm light was maintained.

6.2.4 Influence of Vacuum Drying on the Sample

An important requirement for ToF-SIMS samples is that they remain stable under vacuum conditions. Often fixatives such as paraformaldehyde or glutardialdehyde are used to cross link proteins and preserve tissue structure for ToF-SIMS analyses.[249, 250] However, neither of them were applied here to the whole organ nor to tissue sections as they strongly enhance the autofluorescence of the tissue and may cause some loss of particulate matter from sections.[251] Instead, the lung was cryo-sectioned and dried in the vacuum of the instrument. The influence of this vacuum drying on this sample type was found to be low: comparing the nanoparticle signal distribution of a similar sample by optical means before and after pump-down revealed only a moderate shrinking in z-direction; changes of the lung septal structure appeared negligible also in x- and y-positions, but could not be ruled out completely.

6.2.5 ToF-SIMS Analysis

Analyses were performed using a TOF.SIMS[5] instrument (IONTOF, Münster, Germany) in the dual-beam 3D analysis mode. A pulsed 25 keV Bi_3^+ primary ion beam with a target current of 0.3 pA (cycle time 70 µs) and a field of view of 150 x 150 μm^2 was used. Analysis was performed in random rastering mode with 512 x 512 pixels (dose density: 9.9 x 10^{14} ions/cm^{-2}). A 500 eV Cs sputter beam with a current of 55 nA on an area of 500 x 500 μm^2 was used for depth profiling, applying a dose density of 2.54 x 10^{17} ions/cm^2. Profiling was carried out in the non-interlaced mode. The delayed extraction mode was used to provide high lateral resolution, high mass resolution, and useful ion currents simultaneously. Three replicate analyses on different positions on the same sample were performed in order to check the reproducibility of the data.

6.2.6 Image Processing and Correlation Analysis

Reconstruction of the data sets for the relevant ions and correlation analysis of the ToF-SIMS images were carried out with IONTOF Surface Lab 6.6 evaluation software (Münster, Germany). The respective signal intensities were summed up for the complete depth of the analysis unless stated otherwise to resemble the information depth of the microscopic techniques. Image registration and correlation analysis of microscopic and ToF-SIMS images was done with the Fiji distribution of ImageJ with the StackReg registration plugin and the colocalization threshold plugin.[223, 224, 226] In addition to colocalization pixel maps, which are a graphical representation of colocalization, the Pearson correlation coefficient, a numerical value for the colocalization of images, was calculated. The range of the Pearson correlation coefficient has a range from -1 (perfect anticorrelation) to +1 (perfect correlation). This approach allows the reader to assess the correlation of two images based on a single number and is a frequently used way to compare fluorescence microscopy images.[225, 252]

6.3 Results and Discussion

6.3.1 Detection of Nanoparticles by Fluorescence Microscopy

The phase contrast micrograph shows the typical structure of lung tissue sections with bright alveolar structures and some erythrocyte-filled blood vessels (Figure 6-1 A). The alveolar spaces are filled with the cryomatrix, which does not exhibit a signal in phase contrast microscopy. Numerous discrete fluorescent patches reflect prominent agglomerates of the SiO_2-FITC nanoparticles mostly associated with the alveolar septa (Figure 6-1 B+C). Typically, the intratracheal instillation of a nano-suspension, carried out with a spraying device, leads to a deposition of nanoparticles in central regions of the lung parenchyma. At this point in time the fluorescent nanoparticles were expected to be distributed alongside alveolar septa, and/or to be already partly engulfed by alveolar macrophages. It is assumed that the pattern of these irregular-shaped agglomerates reflects their distribution at the time of sacrifice, *i.e.* when lungs were filled with a protective cryomatrix 3 h post application of nanoparticles. As the SiO_2-FITC nanoparticles were properly suspended in the instillation fluid during instillation it may be speculated that agglomerates form rapidly at the air/liquid interface while nanoparticles are contacting the lung surfactant and/or the lung lining fluid. The description of the nanoparticle distribution is important to understand the toxicological impact of nanoparticles on the lung. Importantly, all the images analysed gave no indication for an uptake of fluorescent material by epithelial cells, which form the alveolar septa and are the major components of the air-liquid interface of the lung.

However, a noticeable amount of autofluorescence can be observed. Magnification (Figure 6-2 A-C) shows that fluorescent patches especially of small agglomerates cannot be reliably distinguished from background fluorescence of the septal tissue components.

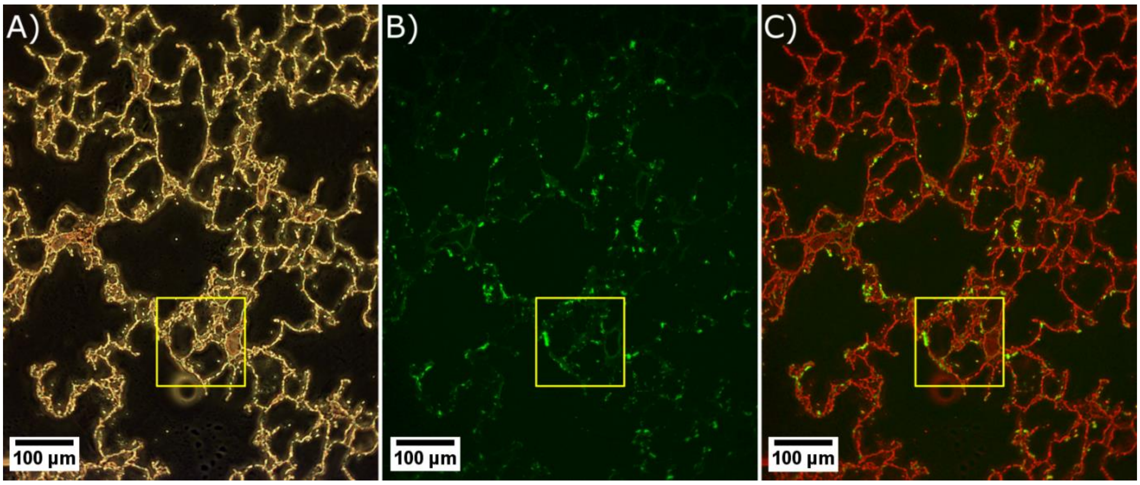

Figure 6-1: Cross section of a rat lung 3 h after intratracheal instillation of SiO_2 FITC nanoparticles (1.2 mg/lung). (A) Phase contrast micrograph showing typical alveolar septa (bright structures) inflated with cryomatrix (not visible) and some erythrocyte-filled blood vessels. (B) Fluorescent image of the same section showing fluorescent patches. (C) Pixels from A were coloured in red and overlaid with image B. Note that fluorescent patches apparently line the alveolar septa. Field of view: 650 x 830 μm^2. The yellow square indicates the ToF-SIMS analysis position (150 x 150 μm^2).

6.3.2 ToF-SIMS Imaging

High-resolution ToF-SIMS 3D analysis is still a time consuming method and mostly restricted to small sampling areas. Therefore, in a first step, a region of interest (ROI) has to be carefully pre-selected and documented. Starting with a structure typical for the lung parenchyma a ROI was selected, in which alveolar septa encompass several medium-sized alveoli in the neighbourhood of a blood vessel, and in which alveoli were decorated with numerous small and large fluorescent agglomerates (Figure 6-1, yellow selection). The copper grid on the backside of the slide was used as an approximate guide for the ToF-SIMS instrument. Final adjustments on the ROI were achieved by comparing the microscopic images to those taken with the internal microscope of the ToF-SIMS instrument. After ToF-SIMS was completed the next step required the identification of secondary ions useful for correlating the ToF-SIMS images with the microscopic image. To this end several correlation analyses were performed and the results will be described and discussed considering some promising technical developments for ToF-SIMS detection of nanoparticles.

6.3.3 Correlation of ToF-SIMS and Microscopic Information

First of all, a secondary ion suitable for the imaging of biologic structures was selected to correlate SIMS imaging results with the light microscopic image. Mainly small molecules are expected due to the molecular fragmentation induced by the harsh Cs^+ sputtering. In this respect, the lateral distribution for the CN^- signal (*m/z* 26.00) was found to provide a structure largely congruent with the bright alveolar septa on phase contrast images (Figure 6-2 D) and is in agreement with earlier studies.[253] Noteworthy, nearly identical signal distributions were found for further ions (*e.g.* CNO^-, C_2HN^-, C_3N^-).

The CN^- ToF-SIMS signal can be used as a pseudo-optical image of protein rich structures and enables the alignment of the distribution of further mass spectrometric signals to the microscopic images. The extent of consistent cellular structures can be assessed from a colocalization pixel map (Figure 6-2 G). This presents the pixels of overlapping structures in white and exclusively microscopic or ToF-SIMS information in green or red, respectively. Contrast stretching was performed on the image to enhance the visibility of the differences. The colocalization pixel map demonstrates that both techniques show the same area of the tissue with minor differences, probably due to sample treatment.

The Pearson correlation coefficient was found to be $R = 0.494$ indicating a substantial amount of positive colocalization.

As ToF-SIMS and microscopic images are differentially influenced, *e.g.* by the 3D structure of the sample, it appears reasonable that minor differences between both images cannot be avoided. In summary, the navigation to and analysis of major structural components related to a light microscopic image is possible using ToF-SIMS images.

6.3.4 Cell Related ToF-SIMS Phosphate Distribution

The ToF-SIMS data set allows to visualize the distribution of elements and small molecules in all 3 dimensions in space via selectable regions of interests. A data reconstruction from a selected volume revealed another striking distribution within the tissue area besides the protein-related distribution of the CN^- signal. The PO_3^- signal (*m/z* 78.96) from sub surface layers of the section shows a heterogeneous distribution with several hotspots within the alveolar septa (Figure 6-2 I). Due to the distribution pattern, which spares the nuclear region, it could most likely be ascribed to phospholipids (phosphatidylcholine) concentrated in type 2 cells, which generate the lung surfactant.

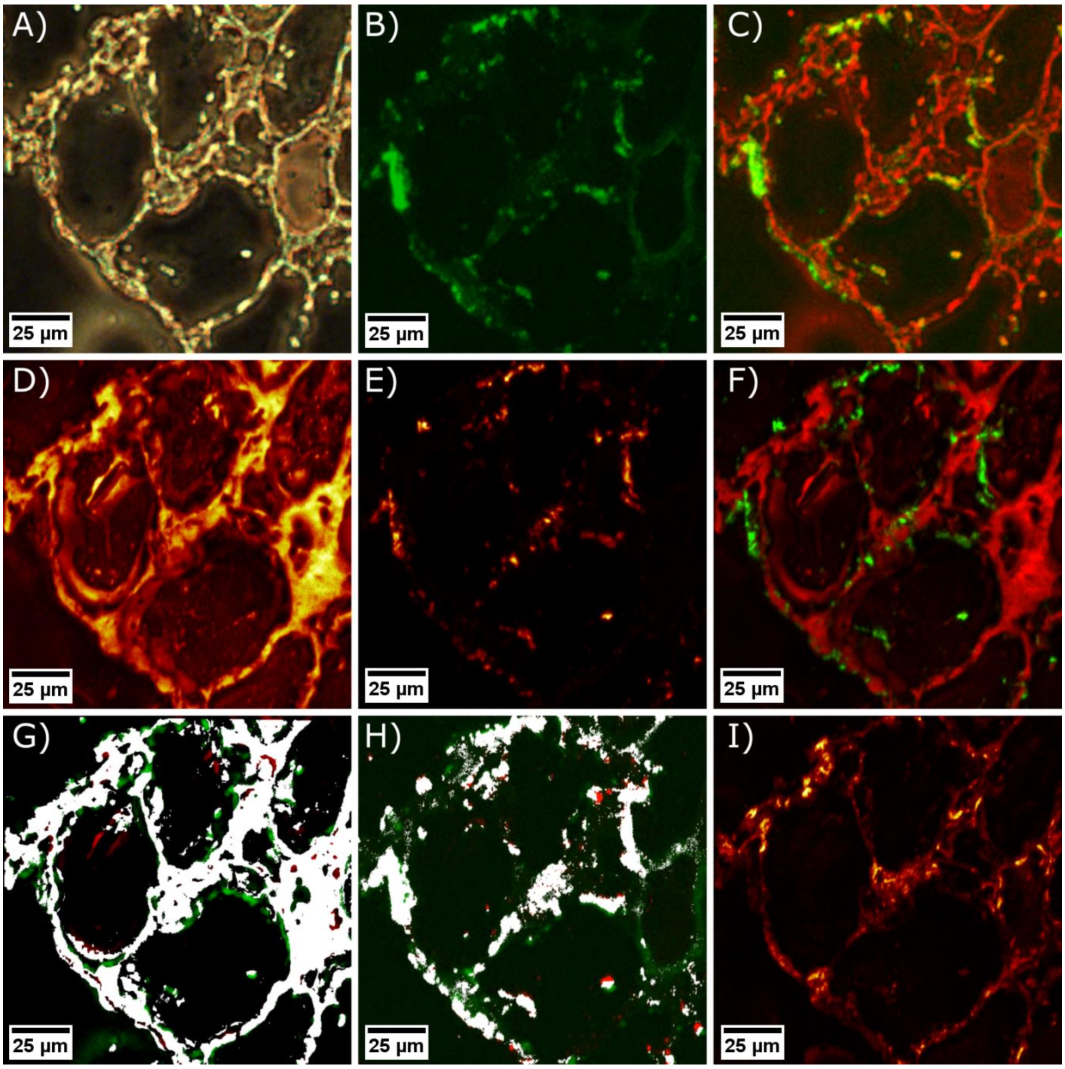

Figure 6-2: Results of fluorescence microscopy, ToF-SIMS, and correlation analyses compared. A) Magnification of the microscopic phase contrast image of the ROI showing bright alveolar septa and darker erythrocyte filled blood vessels. B) Fluorescent image of the selected ROI shows fluorescent patches of various sizes. C) Overlaid phase contrast and fluorescent image (Figure 6-2 A+B) allows the localization of the fluorescent patches within the tissue section. D) The lateral distribution of the ToF-SIMS CN^- signal shows the alveolar structures of the tissue section. E) The lateral distribution of the SiO_3^- ToF-SIMS signal indicates areas of high SiO_2 nanoparticle concentrations. F) Overlay of the ToF-SIMS CN^- (red) and SiO_3^- (green) images (Figure 6-2 D+E) illustrates the position of the SiO_2 nanoparticle within the tissue. G) Contrast-stretched colocalization pixel map of the phase contrast image and the ToF-SIMS CN^- distribution (Figure 6-2 A+D) reveals the congruency of the CN^- signal with septal structures, which are needed for orientation (colocalized features are displayed in white and features exclusive to microscopy or ToF-SIMS (CN^-) are shown in green or red, respectively). H) Contrast-stretched colocalization pixel map for fluorescence signal and ToF-SIMS SiO_3^- lateral distribution (Figure 6-2 B+E) showing colocalized areas in white and exclusively SiO_3^- or fluorescence areas in red or green, respectively. Field of view: 150 x 150 µm². I) Lateral distribution for the PO_3^- ToF-SIMS signal in the deeper layers of the section indicate that the signal is derived from phospholipids-producing type 2 cells.

6.3.5 Detection of Nanoparticle Signals by ToF-SIMS Imaging

The detection of nanoparticle-related signals by ToF-SIMS requires suitable secondary ion species with high secondary ion yield. Usually, the number of secondary ions generated from a single nanoparticle is too low to unambiguously detect individual nanoparticles in a spatially resolved fashion. In this respect, the delayed extraction analysis mode of the instrument was optimized to achieve reliable detection via the combination of a high lateral resolution and high mass resolution at sufficient signal intensities. To optimise the analysis, the number of mass interferences should be low and a correlation with the respective isotopes or higher oxidic clusters (*e.g.* $M_xO_y^-$) is necessary. Especially for nanoparticles made from ubiquitous elements such as silicon it is important to select the appropriate secondary ion species to prevent the detection of false positive signals. Here, the analysis of the SiO_2-containing lung tissue section yielded several potential reporter ions with significant signal intensities for Si^-, SiO^-, SiO_2^-, SiO_3^- and their respective isotopic species, all of which showed correlated lateral distributions. Specifically, both Si^- and SiO^- yielded very low intensities with weak contrast although their lateral signal distribution was similar to those of the much more intense signals of SiO_2^- and SiO_3^-. Although SiO_2^- and SiO_3^- both showed very similar lateral distributions, the SiO_2^- signal was found to slightly interfere with both the CO_3^- and the C_5^- signal and, therefore, was found to be not suited as a SiO_2-nanoparticle indicator ion. Furthermore, Si^-, SiO^-, and SiO_2^- could be fragments that originate from polysiloxane (a frequent contamination typically found by ToF-SIMS analyses). Therefore, the intense SiO_3^- signal (*m/z* 75.96) is best suited as an indicator ion and was used to identify the SiO_2-nanoparticle distribution in the lung tissue.

The lateral distribution of the SiO_3^- signal reveals a non-homogenous but distinctly localized distribution of the nanoparticles (Figure 6-2 E). No significant signal response was detected in areas without cellular structures on the sample target. This is an indication of a successful sample preparation (without contamination/smearing effects).

The superposition of the SiO_3^- signal on the tissue indicator ion CN^- (Figure 6-2 D) in a red-green overlay (Figure 6-2 F) reveals that the majority of the nanoparticle-related signals are associated with the alveolar walls. However, this association is not evenly distributed along the complete alveolar walls. A localized accumulation of the nanoparticles can be observed. However, in the lower right corner only very little SiO_3^- intensity is detected, probably because these areas were less accessible during the instillation.

6.3.6 Nanoparticle Distributions: ToF-SIMS *vs.* Fluorescence Microscopy

The ToF-SIMS images and the fluorescence microscopic images for the nanoparticle related signals both revealed highly localized areas of significant intensities in close proximity to the alveolar walls. Assuming that both signals are derived from the same nanoparticles, a comparison of both images should lead to the same lateral distribution.

A visual comparison of the fluorescence and the mass spectrometric SiO_3^- signal distribution (Figure 6-2 B+E) already reveals a high degree of correlation for the larger structures. The overlays (Figure 6-2 C+F), however, confirm the correlation but also indicate minor differences. A comparison of the images without adequate scaling of the image intensities is challenging, since both techniques are inherently different and involve completely different analyte signal and background levels. Therefore, a calculation of the Pearson correlation coefficient and an image analysis based on a colocalization pixel map were conducted to obtain objective results for the colocalization.

With respect to the analysis by the Pearson coefficient, a correlation coefficient of $R = 0.583$ was determined. This indicates a high amount of colocalization between the results of fluorescence microscopy and SIMS. Compared to the correlation coefficient of $R = 0.494$ for the phase contrast micrograph and the ToF-SIMS CN^- signal, a higher degree of colocalization was found here.

The colocalization pixel map graphically shows similarities and differences between the results of both techniques by a distinct colouring. The pixels for colocalized areas are displayed in white, whereas those areas with a signal exclusive to ToF-SIMS SiO_3^- signals or fluorescence intensity are coloured in red or green, respectively (Figure 6-2 H). A contrast stretching was performed in order to improve the visibility of the differences (colours) in the images. The white areas cover a significant part of the total high intensity signal area for both techniques and indicate a high degree of colocalization. However, minor areas of red or green coloured areas are observed, these are discussed below.

Some areas, which show exclusively a ToF-SIMS SiO_3^- signal but no fluorescent signal, appear red in the colocalization pixel map. The reason for this could either be related to an absence of fluorescence signal (false negative) or to the presence of SIMS signals, which do not originate from the nanoparticles (false positives). Explanations for false positive signals are on the one hand side other sources for the SiO_3^- signal (*e.g.* contaminations) or on the other hand unlabelled nanoparticles. However, SiO_2 containing contaminations were not observed in the spectra and for unlabelled nanoparticles a less localized lateral distribution would be expected. Much more likely is the false negative case with missing fluorescence signals due to small displacements during the measurements or minor difficulties in the image registration. Clearly, image registration and overlaying of the results based on two inherently different kinds of information (fluorescence and secondary ion intensity) might easily result in small differences. The presence of the small red patches only in close proximity to white areas confirms this assumption.

Exclusive green (fluorescence) signals are visible mainly along the alveolar septa. The absence of SIMS signal (false negative) or the presence of a non-FITC based fluorescence signal (false positive) can be considered as possibilities to explain the observations. A matrix effect suppressing the ion formation of the SiO_3^- ion or a concentration below the ToF-SIMS limits of detection are explanations for the false negative case. Signals in fluorescence microscopy might be arising from very small or very few nanoparticles (single fluorophores are detectable[99]). However, both explanations are not likely since the fluorescence signal distribution suggests a high level of autofluorescence throughout the complete material of the section with several hotspots in the dense tissue (false positive). The detection of autofluorescence can be observed especially well in the connective tissue around the blood vessel close to the right border of the image.

Because signals of both techniques are influenced by different sample properties (*e.g.* tissue volumes, density, composition) minor differences between both techniques' results cannot be avoided. In summary, ToF-SIMS and fluorescence microscopy show consistent nanoparticle signals for the large, intense agglomerates and less colocalization for small, less intense fluorescent signals. These are most probably influenced by autofluorescence and image registration inaccuracies. ToF-SIMS is less influenced by interfering signals and is able to detect the SiO_2 nanomaterial as good as fluorescence microscopy. Importantly, in conjunction with the latter it can help to identify the localization of this type of nanomaterial in tissue, which is hardly detectable with other microscopic techniques.

6.4 Discussion: Advantages and Disadvantages of the Techniques

ToF-SIMS was successfully used for the direct detection of a SiO_2 nanomaterial in biological tissue. The thereby found equivalent nanoparticle signal distribution of ToF-SIMS and fluorescence microscopy proves that labels are not mandatory to detect nanomaterials in tissues. This is a prerequisite to eliminate the often prevalent uncertainty on the influence of labels for future toxicological studies. The direct detection approach (without possible influences of labelling reagents on the interaction with tissue components) is attractive for nanotoxicology studies. The complete labelling procedure with time consuming reactions, purification steps, and the determination of labelling efficiencies can potentially be omitted and observed effects can be directly connected to the nanoparticles themselves. Clearly, the detection without a fluorescence label in fluorescence microscopy is only possible if the searched analyte species fluoresce (*e.g.* quantum dots of a certain size).

A very important aspect is the wealth of chemical information, which can be gathered during a single analysis. Not only a selected element/epitope is detected but ions (elemental and compounds) from the whole selected mass range are recorded for every single pixel and layer. The direct detection of several NP species in a single analysis is possible. The comprehensive data sets enable the analysis of signal distributions in all 3 directions in space even for single cells.[188]

The parallel mass detection in ToF-SIMS enables the multiplexed detection of a high number of nanoparticle markers species (*e.g.* via isotopically labelled antibodies), as shown in a recent study from Nolan *et al.* for a sector-field SIMS instrument, offering even more information on the organic sample composition.[173] The use of selected gas cluster ion beams with reactive gas ions improves the detection efficiencies for organic and inorganic species in ToF-SIMS analyses.[254-256] Innovative approaches to use the ToF analyzer in combination with a high-resolution Orbitrap mass spectrometer result in significant improvements in mass resolution and therefore more identified/discriminated species.[257] Furthermore, commercially available MS/MS fragmentation capabilities for the unambiguous detection of high mass ions enhance the importance of ToF-SIMS in the biosciences.[258, 259] In contrast, fluorescence microscopy is limited to the information of the fluorescent species. Multiplexing is possible, though the simultaneous use of only a low number of fluorescence labels (depending on the emission and absorption spectra of the fluorophores) is feasible. Furthermore, the autofluorescence of tissues remains as a problem even for multiplexed analyses. Although a detection of single fluorophores has been shown before, the high level of autofluorescence can disturb the detection of small, labelled nanoparticles substantially.

Recent developments in ToF-SIMS claim achievable lateral resolution in the order of about 50 nm providing a lot of details.[85] Furthermore, improvements in the lateral resolution with simultaneous improvements in ion transmission will increase the level of detail on the single cell level.[86] Due to the physical minimum of the area of the ion formation process (collision cascade with diameters of a few tens of nanometers) and the limited amount of material in small nanoparticles the identification of single nanoparticles with ToF-SIMS remains a challenge. However, the detection of nanoparticles agglomerates within biological tissues works as good as fluorescence detection within the limits set by the preparation technique and the nanoparticle stability themselves. Although several more advanced fluorescence microscopy techniques reach even higher lateral resolution down to the low nanometer range, these techniques also include more complex and expensive setups and significantly reduce the simplicity and ease-of-use as the main benefits for the fluorescence microscopic detection.[260]

Besides the limitations for vacuum stability of the samples, which had been addressed before,[249] a major challenge in ToF-SIMS analysis is quantification. A general approach to quantification is unknown due to the matrix affecting the ionization behaviour. However, strategies for a quantification of nanoparticles in organic matrices are a goal in current research. Quantification in fluorescence microscopy for nanoparticles in biological tissue is also difficult due to varying amounts of autofluorescence from the tissue components.

The possibility to use retrospective analysis enables screening analyses without dedication to a certain ion and offers the possibility to re-evaluate data if new questions arise even a long time after the analysis was done. These features render the higher destructiveness of the ToF-SIMS (complete sample consumption *vs.* laser induced damage in fluorescence microscopy) a far less severe drawback since the complete data set for the selected parameters is already recorded during the first analysis.

Although a ToF-SIMS 3D microanalysis is more time consuming and complex than a simple fluorescence microscopic analysis, it can be a valuable tool complementing and/or extending the analysis of nanoparticle-containing biological tissue with detailed chemical compositions and their lateral and depth distributions.

6.5 Conclusion

The detection and imaging of nanoparticle species after up-take in the biological environment of a rat lung was successfully shown by ToF-SIMS and confirmed by fluorescence microscopy. This combined approach proved the suitability of ToF-SIMS for the direct detection of nanoparticles and/or nanoparticle agglomerates in tissue sections.

These experiments underline the role of ToF-SIMS as a valuable tool for the analysis of biological specimen and the distribution of indicator signals. The possibility to screen the sample for further valuable information, *e.g.* the distribution of other relevant signals, is considered very useful especially for biological questions. Parallel mass detection at high spatial resolution (in three dimensions) delivers comprehensive chemical data.

It is expected that the capabilities of ToF-SIMS for nanoparticle detection and mass-spectral imaging will further improve with the new instrumental developments and optimized systems. Our current interest lays on the optimization of analysis conditions to enable the detection of additional organic ions. Also, the assessment of quantitative data from nanoparticle doped tissue sections by ToF-SIMS analysis was not feasible in the frame of this study but is planned in the near future.

Chapter 7

Marker-free Detection of Ceria Nanoparticles in Lung Tissue Sections

Based on:

L. Veith, D. Dietrich, A. Vennemann, D. Breitenstein, C. Engelhard, U. Karst, M. Sperling, M. Wiemann, B. Hagenhoff, Combination of Micro X-Ray Fluorescence Spectroscopy and Time-of-Flight Secondary Ion Mass Spectrometry Imaging for the Marker-free Detection of NM 212 CeO_2 Nanoparticles in Tissue Sections, *J. Anal. At. Spectrom.* **2018**, *33(3)*, 491-501.

7. Marker-free Detection of Ceria Nanoparticles in Lung Tissue Sections

7.1 Introduction

The use of nanomaterials in everyday life is increasing.[5, 6] This may lead to a pronounced exposition of biological organisms to nanomaterials.[261, 262] Consequently, there is a demand to reliably estimate potential health risks, which is reflected by numerous current research projects in nanotoxicology.[263] Especially airborne particles are of concern, since the lung has been identified as a major entrance port of nanoparticle species into the human body.[14, 15, 239, 264]

With respect to human exposition, a number of nanomaterials is of particular interest such as SiO_2 from food additives or TiO_2 from sunscreens.[120, 265, 266] For lung toxicology, especially the exposition to CeO_2 nanoparticles (NPs) is of high interest as they are used as fuel additives and in automotive catalysts and, therefore, may be present in the ambient air especially close to busy streets.[118] As effects of CeO_2 nanoparticles on the mammalian body are not yet fully explored, a 2-year-lasting chronic inhalation study with low doses of the standard material CeO_2 NM212[267] has been launched from which first results are published[268]. In order to better understand the interaction of NP with the tissue, their lateral distribution, chemical environment, translocation, and agglomeration behaviour in the mammalian bodies have to be revealed. Consequently, the experimental effort to detect and describe the properties also of small amounts of these nanomaterials is increasing. Techniques like laser ablation inductively coupled plasma mass spectrometry (LA-ICP-MS) and Nuclear Microprobe are currently used for the analysis of biological samples[269-272]. Recently it was demonstrated that Time-of-Flight secondary ion mass spectrometry (ToF-SIMS) is a suitable technique for the localisation and identification of selected nanomaterials (SiO_2) within complex lung tissue.[220] This technique allows a marker-free 3D analysis with sub-µm resolution and simultaneous mass spectrometric detection of organic and inorganic species. However, the detailed high-resolution analyses most often are complex and time-consuming. Therefore, a reliable selection of a suitable region-of-interest (ROI) before ToF-SIMS analysis via a non-destructive and marker-free technique is required.

This need for a non-destructive pre-analysis along with the necessity of creating an overview image limits the eligible techniques to those without notable sample damaging. The detection of *e.g.* CeO_2 nanoparticles by dark-field and/or hyperspectral microscopy in organic matter appears as an alternative[273, 274] but, as we learned from our own but unpublished studies, the method is limited to nanoparticles (or agglomerates thereof), that scatter light sufficiently. The related spectra need to be identified in a spectral library obtained from the material in question. Thus, while the identification of particles from different elements and sizes with hyperspectral imaging techniques demands further research, the approach is not yet fully sufficient for a reliable pre-analysis of samples for ToF-SIMS analyses[273, 274]. Sophisticated fluorescence microscopy approaches often provide remarkable lateral resolution but are limited to the use for fluorescing particles or fluorescent molecules which highlight the desired particle species.[220] Infrared and Raman imaging spectroscopy allow an assessment of compounds in biological tissue by the analysis of vibrational states of functional groups[275]. The identification of inorganic vibrational states exhibited from nanomaterials could be useful for the selection of notable areas on a tissue section[276]. However, since the composition of the materials is not directly accessible and the sampling area is also limited, the use of these techniques for an analysis prior to ToF-SIMS 3D analysis seems inappropriate if highly distributed particles need to be detected. X-Ray photoelectron spectroscopy provides a higher confidence for the identification of the materials along with a good lateral resolution in the micrometer range and the possibilities for quantification. However, the instruments are much more complex and the information depth is limited to less than 10 nm[277]. This low information depth disqualifies the technique for pre-analysis prior to ToF-SIMS 3D imaging. Consequently, none of these non-destructive techniques fulfils all criteria required for a reliable pre-analysis of tissue sections.

In contrast, the marker-free and fast micro X-ray fluorescence spectroscopy (µ-XRF) allows the mapping of elemental distributions on large samples by analyzing the emitted radiation (X-ray fluorescence) from previously excited states of elements and is, therefore, a promising technique for ToF-SIMS pre-analysis. Micro-XRF features parallel detection of elements of higher mass than sodium ($Z > 11$). Although tabletop µ-XRF has a lower spatial resolution and sensitivity than synchrotron based XRF, its availability and high sample throughput make it a versatile technique[278, 279]. To assess whether this technique is suitable as a pre-analysis technique for ToF-SIMS 3D imaging analysis, we compared the lateral signal distributions of CeO_2 NP containing lung tissue sections from a nanotoxicological study.

This paper describes the alignment of µ-XRF and ToF-SIMS 3D signals from cryo-sections of rat lungs, which were intratracheally instilled with well-dispersed CeO_2 nanoparticles, to study the NPs tissue distribution and uptake. To this end sample sections were pre-analysed by µ-XRF and the resulting elemental distribution was combined with a microscopic reference image. The resulting low-resolution overview image served to select representative regions-of-interest (ROIs) for ToF-SIMS 3D imaging. Results suggest that the non-destructive µ-XRF is well suited and a versatile pre-analysis technique to select ROIs for ToF-SIMS 3D analyses in large tissue sections.

7.2 Experimental Section

7.2.1 Particle Characterization and Dispersion

Well characterized CeO_2 NM212 nanoparticles provided by the Joint Research Center (JRC, Ispra, Italy) were used in this study.[267] In brief, the primary size of the polyhedral particles with irregular morphology, as revealed by transmission electron microscopy (TEM), was 10 to 200 nm. The particle surface amounted to 27.2 m^2/g (BET) and was composed of 42% O, 26% Ce and 32% C, as analysed by XPS. The zeta potential in deionised water was found to be 33 mV.

For intratracheal instillation we dispersed 1.2 mg CeO_2 NM212 NP per mL sterile double distilled H_2O. Extended ultrasonication was carried out with a Branson 450D Sonifier operated at 10% amplitude for 16 min. H_2O as a diluent was found superior over *e.g.* saline as nanoparticles remained stably suspended for extended periods. The resulting particle size distribution was determined by optical tracking analysis using a NanoSight LM10 instrument equipped with a green laser (532 nm), an Andor CCD camera, and NTA software 3.0 (Malvern Instruments GmbH, Herrenberg, Germany) and revealed small agglomerates ranging between 70 and 300 nm (Figure 7-1). Particles were also embedded in Epon 812, thin sectioned, and viewed with a Tecnai electron microscope operated at 120 kV. Images confirmed the size and shape of single and agglomerated NP (Figure 7-1).

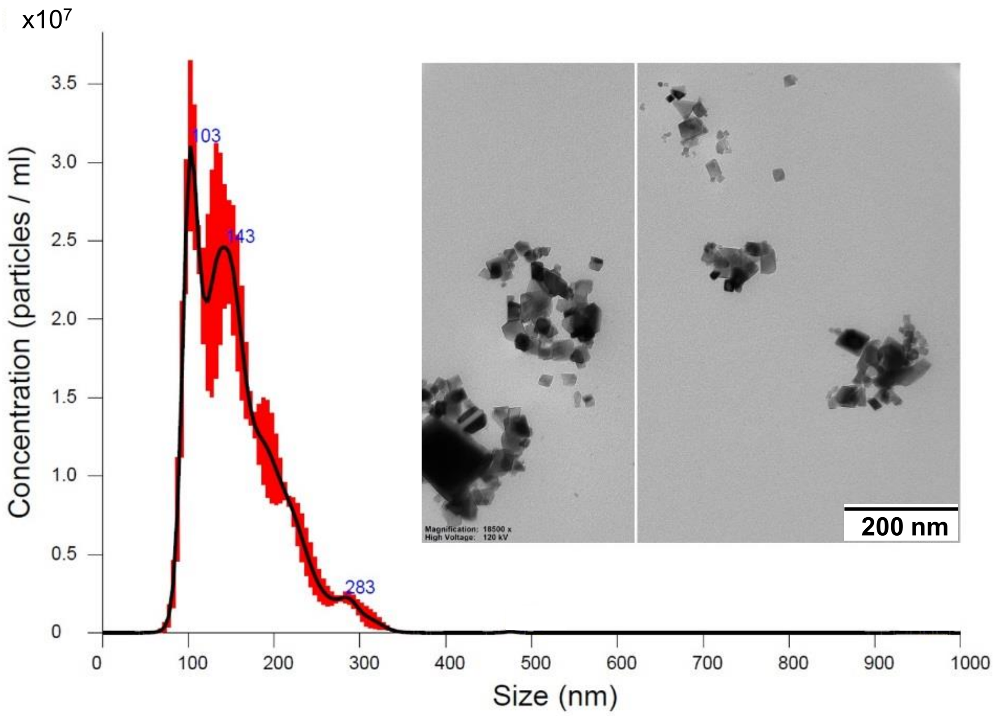

Figure 7-1: Size distribution of CeO_2 NM212 nanoparticles in aqueous suspension as used for intratracheal instillation. Measurements was carried out by NanoSight optical tracking analysis. The inset shows electron microscopic images of CeO_2 NM212 nanoparticles as typically found in the instilled suspension.

7.2.2 Animal Experiments and Lung Tissue Preparation

All animal experiments were carried out in the animal facility of the University Clinics of Münster, Germany, and were ethically approved by local authorities (LANUV, Dortmund, Germany) under the accession no. 84-02.04.2022.A157. Young female rats (Wistar strain WU) weighing 200-250 g were purchased from Charles River Laboratories (Sulzfeld, Germany) and maintained with a 12 h lights-on lights-off cycle. Food and water were provided ad libitum. Animals were briefly anaesthetized with 5% isoflurane in air and 500 µl of the instillation fluid containing 0.6 mg (w/v) CeO_2 was intratracheally instilled with a Penn Century Microsprayer under visual control. After 3 h rats were deeply anaesthetized with a mixture of ketamine and xylazine and bleeded via the aorta descendens. A cannula was inserted into the trachea and the left lung was inflated with 3 ml Cryomatrix (Thermo Shandon Ltd., Runcorn, UK), while the right bronchus was ligated and prepared for other analyses (not shown). The left lung was immediately resected, cut into 5 portions with a razor blade, each of which was snap frozen in liquid nitrogen and stored at -80°C until further processing. Transverse sections (7 µm) were cut from the hilar region with a cryo-microtome (Microm HM 500), and dried onto indium-tinoxide

(ITO)-coated slides (Sigma-Aldrich, Taufkirchen, Germany) with a surface resistivity 70-100 Ω. Sections were stored at -28°C.

7.2.3 Micro X-ray Fluorescence Analysis

The tissue section was analyzed by means of non-destructive µ-XRF performed with a TORNADO M4 X-ray fluorescence spectrometer (Bruker Nano GmbH, Berlin, Germany). The system was equipped with a rhodium-anode X-ray tube working at a voltage of 50 kV and an anode current of 600 µA. Polycapillary optics focus the X-ray beam to a spot size of approximately 25 µm in diameter for Mo-Kα. Detection of the X-ray fluorescence was achieved with a silicon drift detector (SDD, XFlash® 5030, Bruker Nano GmbH). Additional measurements were carried out in a evacuated sample chamber (20 mbar) and a filter (100 µm aluminium) was used to decrease background levels. The thin cross sections were mapped with a step size of 25 µm and an acquisition time of 10 ms for each spot. Ten runs of an area of 16.1 × 10.6 mm2 were performed within about 7.5 h. Data evaluation was carried out using the software ESPRIT HyperMap (Bruker Corporation, Germany) and ImageJ (National Institute of Health, Bethesda, MD, USA) was used for image generation.

Due to a high background signal for the Ce signals, the non-local means denoising algorithm plugin for ImageJ was used to remove the statistically distributed background signals and the brightness and contrast of the images were adjusted to improve the visibility of the signals.

7.2.4 Microscopic Analysis

Microscopic images were acquired by reflected-light microscopy after µ-XRF imaging and were used for the alignment of further analytical results. An optical profiler instrument PLu neox (Sensofar-Tech, Barcelona, Spain) was used in the Bright Field Extended Image Measurement Mode. Levelling of the sample stage was done manually, whereas focus and lighting were adjusted by the automated functions. A 5x EPI-objective was used to acquire a high-resolution image of the whole section (total resolution: 4914 x 3684 pixels, pixel size: 3.3 x 3.3 µm, pixel density: 300 Pixel/mm).

7.2.5 ToF-SIMS 3D Imaging Analysis

ToF-SIMS analysis was conducted after evacuation of the sample chamber (to 1×10^{-6} mbar) at ambient temperature. Analyses were performed using a TOF.SIMS[5] instrument (IONTOF, Münster, Germany) in the dual-beam 3D analysis mode. The primary ion beam was Bi_3^+ with a target current of 0.3 pA, and a field of view of 300 x 300 µm² or 100 x 100 µm². Analysis was performed in random rastering mode with 512 x 512 pixels. (Dose density: 1.1 - 6.7 x 10^{13} cm^{-2}). A 1000 eV O_2 sputter beam with a current of 170 nA on an area of 300 x 300 µm² or 500 x 500 µm² was used for depth profiling, respectively. The applied ion-dose density was 1.8 x 10^{17} ions/cm². Profiling was carried out in the non-interlaced mode with a cycle time of 70 µs. The delayed extraction mode was used to provide high lateral resolution, good mass resolution, and useful ion currents simultaneously. The reproducibility of the data was studied by replicate analyses (three replicates of Ce-rich and three replicates of Ce-poor areas) on the same sample performed in the same manner (compare appendix, chapter 10, Figure 10-1). Data evaluation for the ToF-SIMS 3D imaging data sets was done with the IONTOF Surface Lab 6.7 evaluation software (Münster, Germany).

7.2.6 Image Overlay and Alignment

Overlaying and alignment of images was done with the Fiji distribution of ImageJ[223, 224]. Alignment of the µ-XRF results with the microscopic images was performed by first aligning the K distribution to the microscopic image and afterwards fitting the Ce distribution (with identical dimensions) to the previously aligned K-distribution on the image. In this way, the influence of slight differences in the viewing angle of the microscope and the signal collection angle could be excluded. ToF-SIMS results were compared to the µ-XRF results via an alignment of a tissue indicating ToF-SIMS signal distribution with the pre-aligned microscopic image.

7.3 Results and Discussion

7.3.1 Micro X-Ray Fluorescence Results – Elemental Maps for K and Ce

To achieve a fast analysis of the whole tissue section we confined the spatial µ-XRF analysis to the signals of potassium (K) and Ce (Figure 7-2).

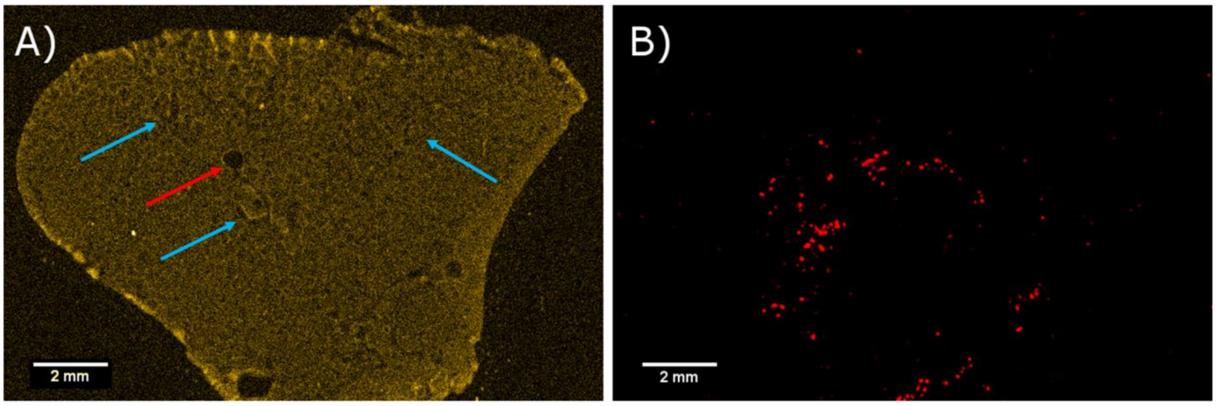

Figure 7-2: Potassium and Cerium µ-XRF signal distribution in cryo-section of the rat lung. A) The K distribution shows notable lung structures. Arrows point to major bronchi and blood vessels, which are seen in the microscopic image of Figure 3A. B) The Ce signals are predominantly localised in the central regions of the lung.

Comparison of Figure 7-2A and Figure 7-3A shows that the K distribution reflects the shape of the complete lung section. As bronchi and air space of the lung was inflated with a structure-preserving cryomatrix, which contains potassium formate, most structures appear at a low contrast. However, major blood vessels and bronchi (red and blue arrows, respectively, in Figure 7-2A and Figure 7-3A) and also areas with the typical alveolar structures are visible. While the intensity of the homogeneous K signal sharply declines toward the ITO coated slide, parts of the outer rim showed an enhanced K signal, which was most likely caused by evaporation and tissue shrinking during sectioning.

In contrast to the K signal, there was a largely inhomogeneous lateral distribution of the Ce µ-XRF signal (**Figure 7-2**B). Areas of distinct patches were centred around the large bronchi and only few Ce signals appeared in peripheral areas of the lung parenchyma. Since Ce is not normally detected in control lungs, the Ce signals imaged with µ-XRF reflect the intratracheally instilled nanoparticles. Notably the observed Ce pattern is typical for an early stage distribution of nanoparticles applied with a micro sprayer device[280]. As the µXRF method is fast, non-destructive, and applicable to many other elements, it appears suitable for a first localisation of nanomaterials in biological tissue. However, as the lateral resolution is limited, we aligned µ-XRF images with tissue structures, which were visualized by reflected light microscopy, as is described in the following section.

7.3.2 Microscopic Alignment and Structural Conservation

A microscopic overview image of the tissue section was taken with reflected-light microscopy to allocate results of the elemental maps from the μ-XRF analysis to the tissue structure. Figure 7-3A shows the main structural features of a typical lung tissue section such as alveolar septa (blue arrows), bronchioles and major blood vessels (red arrows) at high contrast. Some needle-like structures (yellow arrows) are observed in the magnified image (Figure 7-3B). These occur mostly on top of the alveolar spaces and are regarded as crystallised salt stemming from the viscous cryomatrix, because they contain K (Figure 7-6C). Filling of the alveolar space with the cryomatrix is further indicated by a concentric optical interference pattern seen in most alveoli, suggesting that the dried cryomatrix has formed a meniscus-like structure within the alveoli. Thus, the microscopic analysis shows that, in the absence of chemical fixation, fine elements of the lung tissue structure such as alveolar septa were successfully preserved.

In the next step we aligned the microscopic image with the μ-XRF results (Figure 7-3C) using the K signal distribution where major blood vessels and bronchioles along with the outer rim were used as contrasting structures. The overlay shows that the K signal is detected throughout the lung parenchyma but also in large bronchi, suggesting that both the tissue and the cryomatrix are sources of potassium.

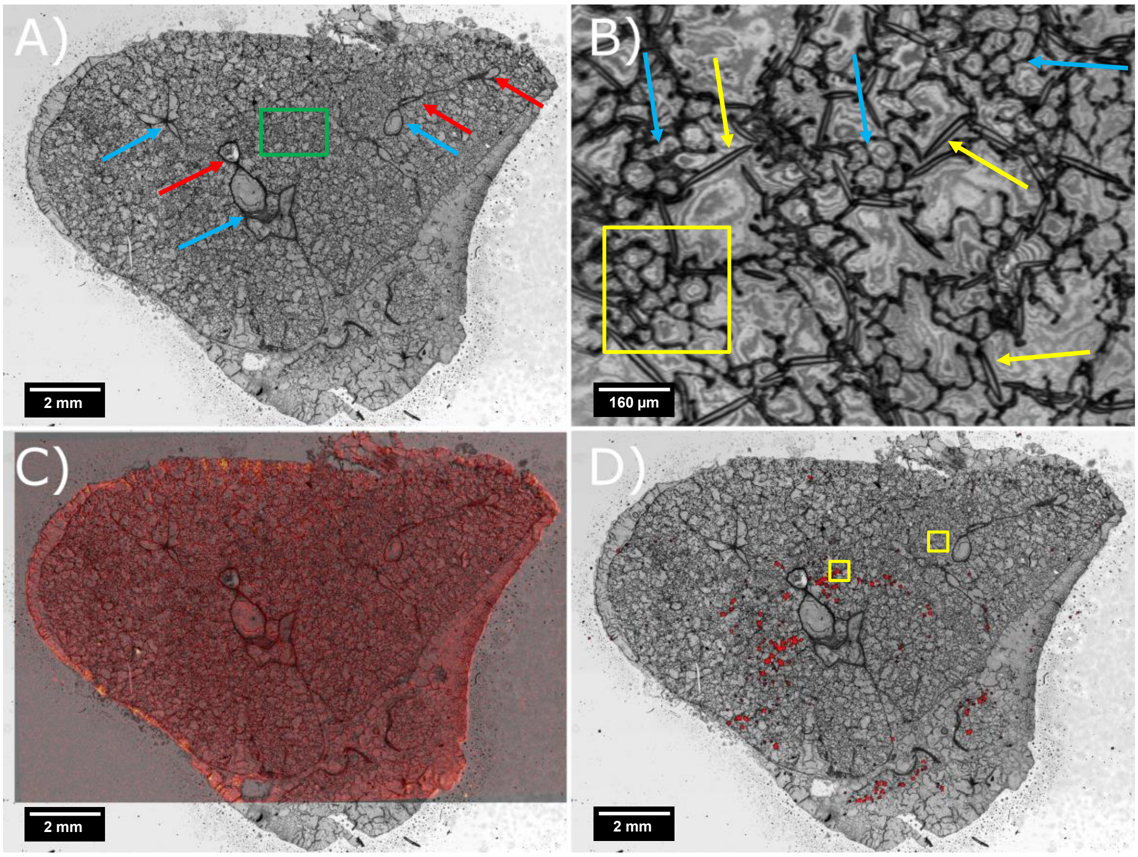

Figure 7-3: Colocalization of the lung microstructure with K and Ce distribution from µ-XRF. A) Reflected light micrograph of the lung tissue section showing major elements of the microstructure. Major bronchioles and blood vessels are marked by blue and red arrows, respectively. B) Magnified boxed area from (A) showing the typical preserved structure formed by alveolar septa (blue arrows); some needle-like structures are seen on top the lung structures (yellow arrows). C) Overlay of the microscopic image with the K-signal distribution from Figure 7-2A is used to precisely align further µ-XRF results. D) Overlay of the microscopic image with the Ce-signal distribution from Figure 7-2B. This overlay image was used to select ROIs for ToF-SIMS 3D Imaging analysis. Yellow squares in (B) and (D) demarcate the regions chosen for ToF-SIMS analyses of a central and peripheral lung area, respectively.

Correlation of the Ce distribution data from µ-XRF data with tissue histology (Figure 7-3D) showed that a high Ce intensity mostly appeared in central regions of the section close to the region of end terminal bronchiole, whereas low amounts of material are scattered with low frequency throughout peripheral areas. For inhaled particles there is a size-dependent sorting of particles while they pass the upper airways and particles smaller than 2.5 µm and especially nano-sized objects can easily reach the lung parenchyma[281]. These small particles will primarily attach to alveolar walls from where they are taken up by alveolar macrophages, or might enter or even permeate the lung epithelium. The intratracheal instillation of a nano-suspension via a spraying device, as used here, circumvents the upper airways. The size distribution of the applied particles was measured in the instillation fluid by nanoparticle tracking analysis and amounted to a mean sizes of ca. 70-300 nm (Figure 7-1). However, secondary processes may lead to larger agglomerates especially in central areas: While the instillation fluid is rapidly retrieved from the airspace via lymph and blood vessels, nanoparticles may be concentrated at the alveolar walls. Although not yet directly proven, nanoparticles may further agglomerate upon contact with the lung surface which is covered by lung surfactant and the underlying lung lining surface. From an analytical point-of-view it was therefore important to investigate and compare central and peripheral regions with high and low Ce concentration, respectively. As shown in Figure 7-3D such regions were selected by the analyst for ToF-SIMS 3D imaging analysis by combining the Ce signal from µ-XRF with microscopic images.

7.3.3 ToF-SIMS 3D Imaging

Based on the overlay of structural information (microscopy) and the elemental Ce distribution found by µXRF, two ROIs were selected from replicate measurements to present ToF-SIMS analyses in detail (Figure 7-3D). One is representative for a total of five central ROIs with high Ce signals, and the other one represents four peripheral ROIs without Ce signals.

During ToF-SIMS 3D imaging analysis, the rastering of the sample is combined with a sample erosion by a sputter beam. In contrast to µ-XRF spectrometry, the sample is completely consumed in the course of the analysis. The analytical result is a five-dimensional dataset (x-, y- and z- position, mass-to-charge ratio, signal intensity) that can be evaluated in various ways. In this study, the lateral signal distributions, *i.e.* secondary ion images, were of interest. Such images can be reconstructed for all detected signals that add up to several hundreds in the chosen “delayed extraction mode”. Information from z-levels containing analytical information from the tissue were evaluated and combined into a two-dimensional projection. Information from z-layers after complete sputtering of the tissue (*i.e.* from the tissue subjacent ITO-layer) was not included into this projection. For the scientific problem addressed in this study, the following information is of interest: On the one hand, an ion species allowing the detection of structural features (“tissue marker”) of the sample is needed. On the other hand, the detection of Ce containing species is the goal of the analysis. Finally, other secondary ion species may provide further information on the sample.

7.3.3.1 Tissue Marker Selection

To facilitate a comparison between ToF-SIMS images and other imaging techniques, a secondary ion showing the tissue contrast of the biologic structures is needed to precisely align the data sets. The distribution of the K_2CN^+ for the inner analysis area (Figure 7-4A) shows a highly compartmentalized structure of high intensity with nearly no interruptions for both analysis positions. Within the compartments, only minor signal intensities are observed. The distinct distribution of K_2CN^+ closely resembles the typical tissue structure of the lung. For the negative secondary ion polarity, typically CN^- or CNO^- are used to follow the tissue structure, since they mainly resemble the structure of the protein-rich alveolar septa with minor deviations.[253] Likewise, in the positive secondary ion polarity, the K adducts of CN^- and CNO^- are suited to obtain a pseudo-optical image of the alveolar structures on K rich samples. However, this might be limited to samples with a high salt content.

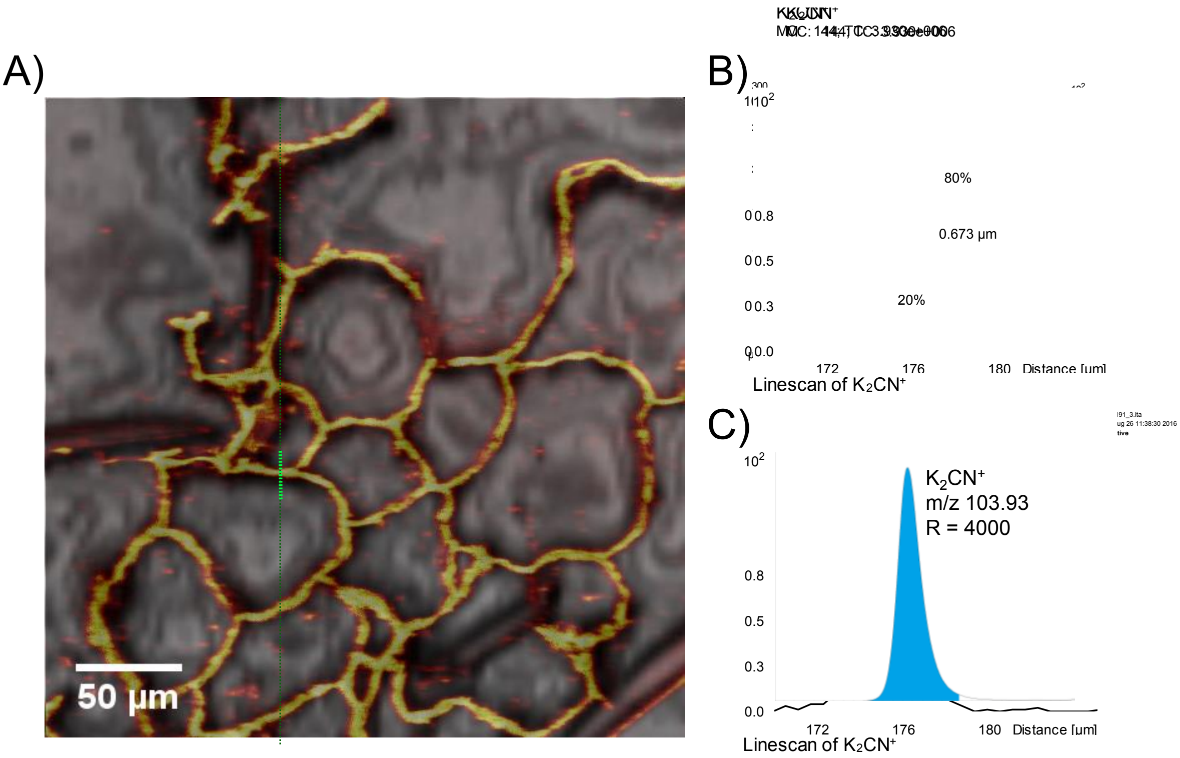

Figure 7-4: Comparison of microscopic and ToF-SIMS-derived lung tissue structure. A) Overlay of the K_2CN^+ signal distribution (brown-yellow colour scale, translucent) and the micrograph (grey scale, opaque) showing the identity of the analysed position. The solid green indicates the position for the determination of the lateral resolution of the analysis. B) The linescan at the indicated position reveals the lateral resolution of about 670 nm according to the 80%/20% intensity difference definition. C) The mass resolution for the K_2CN^+ signal is determined to R=4000 according to the Full-width at Half-maximum (FWHM) definition.

Via the K_2CN^+ signal distributions, the mass spectrometric information can be aligned with the microscopic image and thereby with the µ-XRF images. Although minor differences might be observed due to the different influences of the 3D structures on the techniques (*e.g.* regarding the apparent thickness of the alveolar septa), it is obvious that the techniques´ results relate to the same area (Figure 7-4). This alignment procedure based on notable contrasts allows an alignment with high confidence and serves as a cross-validation confirming the analysis of the correct region.

Additionally, the alveolar structures can be used to estimate the lateral resolution and mass resolution for this ToF-SIMS analysis. The solid green line in Figure 7-4A indicates a central alveolar structure selected to demonstrate the lateral resolution obtained in this analysis. Via the 80%/20% signal intensity difference definition (common for ToF-SIMS) a lateral resolution of about 670 nm is achieved (Figure 7-4B). The mass resolution was determined according to the full-width at half maximum (FWHM) definition and resulted for the K_2CN^+ signal at *m/z* 103.93 in a mass resolution of R = 4000.

7.3.3.2 Detection and Identification of NP-related Ce Signals

Out of all the $Ce_xO_y^+$ signals, the $^{140}CeO^+$ ion yielded the most intense secondary ion signal without any significant interferences and was selected as the most useful nanoparticle marker ion for this study. The necessity of a secondary ion species with a high secondary ion yield for the detection of small particles with low signal intensities limits the number of available species. For the Ce isotopes (^{136}Ce, ^{138}Ce, ^{140}Ce and ^{142}Ce at natural abundance ratios of 0.19 : 0.25 : 88.48 : 11.08) notable intensities are only detected for the most abundant ^{140}Ce and ^{142}Ce isotopes in tissue sections. Although the presence of both isotopes along with their intensity ratios most often is sufficient for an identification based on the isotopic fingerprint, a correlation of the lateral distributions of the intense Ce isotopes and its Ce_xO_y clusters was facilitated to assign the signals with optimal confidence. Thus, a successful colocalization of the lateral distributions for $^{140}Ce^+$, $^{140}CeO^+$, $^{142}CeO^+$, $^{140}Ce_2O_2^+$, $^{140}Ce_2O_3$, $^{142}CeO_2^+$ and $^{142}Ce_2O_3^+$ was used to confirm the presence of the CeO_2 nanoparticles (compare appendix, chapter 10, Figure 10-2).

7.3.3.3 Ce Distribution in Central and Peripheral Areas

Analyses from ToF-SIMS 3D datasets are shown as two-dimensional projections in Figure 7-5. The distribution of CeO^+ (representative for the colocalized Ce_xO_y species) in the central ROI shows several intense areas (Figure 7-5C) 3 h post instillation. While the original thickness of the section was approximately 7 µm, size of the (projected) single CeO^+ spots was up to 10 µm. These signals were predominantly found close to alveolar walls or, to a lesser extent, freely in the alveolar space. In rare cases small punctuate CeO^+ signals were co-localized with alveolar septa, and this may reflect a rare penetration of nanoparticles or small agglomerates into the epithelium. However, as the tissue sections were not chemically fixed an artificial localization especially of small structures cannot be excluded. Importantly, ToF-SIMS analyses gave no hints for a considerable permeation of CeO_2 NP into the lung epithelium even if nanoparticles were instilled into the lung under low ionic strength conditions.

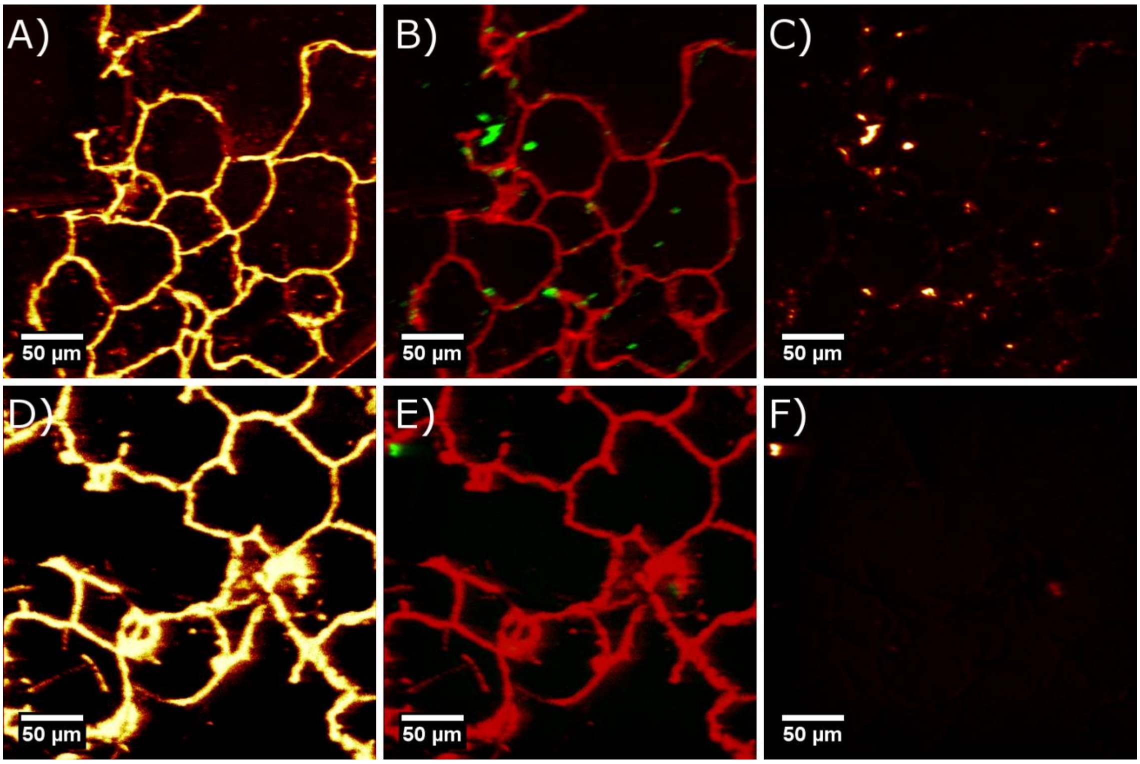

Figure 7-5: ToF-SIMS analyses of CeO_2 nanoparticle laden lung tissue areas. Images show two-dimensional projections of the signals obtained with ToF-SIMS 3D imaging. Top row: Central area, A) K_2CN^+ signal distribution showing the tissue structures of the lung. B) Overlay image showing tissue components from (A) in red and the CeO^+ signal in green. C) CeO^+ signal distribution. Bottom row: Peripheral area. D), E) and F are equivalent to A), B) and C)

Figure 7-5D-F show the CeO^+ and K_2CN^+ signal distribution for a peripheral area and an overlay of both. Although no Ce signal was detected by µ-XRF, ToF-SIMS analysis clearly revealed two CeO^+ positive spots with a size of 5-10 µm (Figure 7-5F). While one was located close to an alveolar wall (top left corner) the other one (right from centre) was partly enclosed by K_2CN-positive tissue material which suggests the presence of or uptake by a macrophage.

Importantly, all Ce signals were likely caused by agglomerated CeO_2 nanoparticles. Evidence for this comes from the fact that CeO^+ spots observed 3 h post instillation were fairly larger than the originally instilled particles (see Figure 7-1), and that signals were cell-free, *i.e.* they were not colocalized with or surrounded by K_2CN^+ signal (except for one case in Figure 7-3F). We therefore hypothesize that agglomerates of CeO_2 NP form after application of the aqueous suspension. Concerning the mechanism, it is conceivable that the progressive adsorption of the diluent (H_2O) increases local particle concentration, enforces the contact of nanoparticles with components of the lung surfactant and/or the lung lining fluid, and leads to increased ionic strength. Eventually this would lead to a drop in zeta-potential of CeO_2 nanoparticles[245] and might have caused agglomeration. As the bio-kinetic behaviour of nanoparticles depends on their size in the body, the observation of an early formation of CeO_2 NP agglomerates from aqueous instillation fluids is of relevance.

7.3.4 Comparison of the Ce Lateral Distributions from µ-XRF and ToF-SIMS 3D Imaging

The alignment of the microscopic images with the µ-XRF Ce intensity enables a comparison of the X-ray fluorescence signal distribution with the ToF-SIMS lateral distribution. The comparison of the lateral distributions of the intense signals in general shows a similar distribution for both techniques. For the ToF-SIMS analysis, a medium resolution (pixel size 600 nm) was chosen to facilitate a relatively fast imaging of a large area with sufficient lateral resolution. Due to the lower lateral resolution of the µ-XRF analysis (pixel size 25 µm), the Ce intensity is less spatially defined than the secondary ion intensity distribution. The lateral resolution differs by a factor of 42, which makes a direct comparison of the data difficult. Exemplarily, lateral resolution of the ToF-SIMS data was reduced to approximately 25 µm by binning (by summing up 42 x 42 pixels to form a single (super) pixel in a new image), which helped the comparability of features in obtained images of both techniques. Figure 7-6A presents the summed up ToF-SIMS image revealing some intense pixels along with a lot of less intense pixels. Figure 7-6B shows the µ-XRF intensity distribution in the same area. Considering the vastly different lateral resolutions and the superimposition of three different techniques, a notable similarity for high intensity Ce signals can be observed. The ToF-SIMS imaging and µ-XRF lateral distributions all in all confirm each other. However, some differences remain, which can be attributed to the lower lateral resolution and the high background of the Ce signal in the µ-XRF, which does not allow the discrimination of small particles from the background. The comparability of the results ensures a straightforward selection of promising ROIs with high Ce concentrations for high resolution ToF-SIMS 3D imaging analysis. The similarities in the signal distributions are an important factor assuring the validity of the results for the localization of the nanomaterials within the tissue.

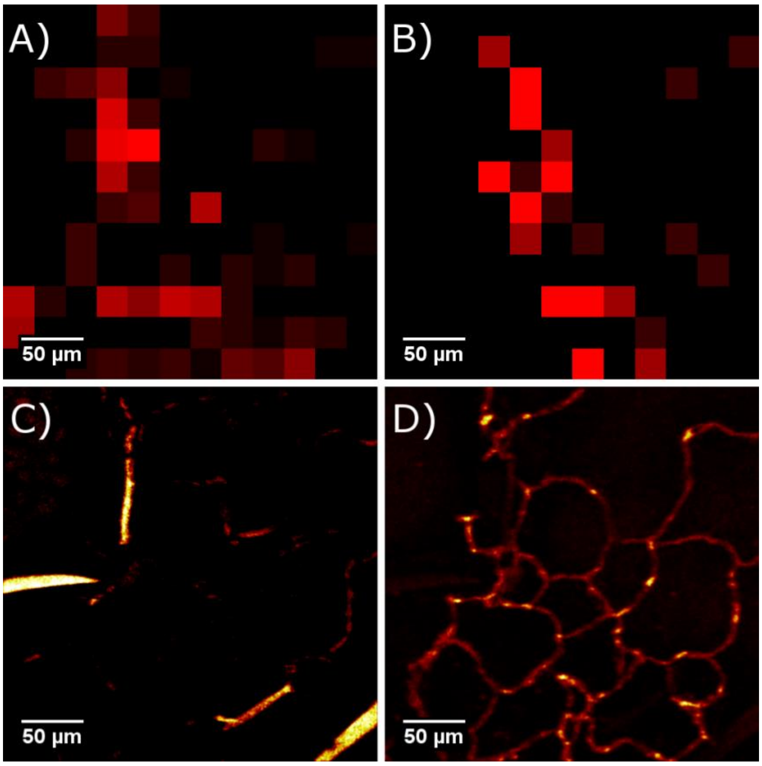

Figure 7-6: Comparison of analytical information derived from µ-XRF and ToF-SIMS. All images were taken from the same site. A) Lateral distributions of the ToF-SIMS CeO^+ signal. 42x42 Pixels were summed up to adjust the resolution to 25 µm/Pixel. B) Ce signal distribution as detected by µ-XRF analysis of the same area as the ToF-SIMS analysis. C) Lateral distribution of the $K_3Cl_2^+$ signal showing needle-like structures similar to the microscopic image (Figure 7-3B). D) The $K_4PO_3^+$ signal distribution resembles the tissue structure with additional hotspots of K_4PO_3 signals within the tissue material.

Furthermore, µ-XRF allows for screening samples with unknown compositions to select the best analysis parameters (*e.g.* polarity, primary ion, sputter ion etc.) for follow-up analyses by ToF-SIMS 3D imaging depending on the nature of the expected materials.

Due to its non-destructiveness, multiple analysis runs with different parameters are possible without altering the sample integrity. The use of a table top µXRF instrument in the laboratory is a convenient way of finding ROIs also for other analytical techniques like laser ablation-inductively-coupled plasma-mass spectrometry (LA-ICP-MS).[282]

Moreover, the combination of the techniques supports the development of particle distribution scenarios: The µ-XRF results allow a fast assessment of the coarse distribution of particles within the tissue section. This information can be utilized to develop a particle distribution model, depending on the nature of the particles, size, coating, agglomeration states, *etc*. for the complete lung: *e.g.,* particles agglomerating close to major bronchioles directly after instillation or distributing into the fine alveoli at the outer areas of the lung. High-resolution ToF-SIMS 3D imaging analyses can now help to elucidate distributions of particle accumulations at cellular components or the penetration into cells. Recent technical developments in ToF-SIMS with lateral resolutions below 50 nm are promising for the detection of individual nanoparticles within their surrounding materials in the future. However, these ultimate resolutions are obtained in the analysis of test structures like the BAM L200 under ideal experimental conditions.[85]

7.3.4.1 Added Values: Crystal Composition and Localization of Nuclei

The high number of signals observed in the ToF-SIMS data set contains further valuable information on the sample. Two examples are mentioned briefly to illustrate the versatility of the analytical approach. Due to the parallel mass detection and the retrospective analysis capabilities of ToF-SIMS, the composition of the previously observed needle-like structures (crystals) is easily elucidated. The lateral distribution of the $K_3Cl_2^+$ signal shows highly localized needle-like structures (Figure 7-6C) similar to those observed above in the microscopic image (Figure 7-3B). These were used as a template to select a ROI for a retrospective analysis of the ToF-SIMS data relating exclusively to the crystal containing areas. Their main composition was found to be Na, K and Cl. The origin of the salt forming species is obvious, considering that the instillation fluid contained NaCl and the cutting matrix contained K. Moreover, the $K_4PO_3^+$ distribution basically resembles the tissue structures but includes several highly intense signals within the tissue (Figure 7-6D). Considering the omnipresence of the K part of the signal, the origin of these spots is most likely predominantly influenced by the availability of the PO_3. Therefore, it is likely that this signal is evoked by high concentrations of DNA/RNA with its phosphate backbone in the nuclei of cells or by phospholipids-producing the type 2 lung cells. The use of gas cluster ion sources for sample erosion in future studies might elucidate this and other questions by reducing the amount of fragmentation of organic species. This new development might be especially relevant for substances adsorbed onto the nanomaterials as well as their direct surroundings (*e.g.* detection of inflammation markers), since these might explain the origin of toxicological effects.

Furthermore, the (parallel) detection of further nanoparticle species in different tissues is planned to develop guidelines for the optimal selection of analysis parameters for nanoparticle detection by ToF-SIMS 3D imaging.

7.3.4.2 Limit of Detection

The analysis of the peripheral analysis position, where the µ-XRF showed no signal, allows a comparative assessment of the limits of detection for both techniques. The µ-XRF signal distribution does not show any notable intensity in the image of the outer analysis position. The ToF-SIMS image however, shows some Ce signals in the outer area. In general, if no µ-XRF Ce signals are detected, lower intensities are found in the ToF-SIMS analysis compared to areas of µ-XRF Ce detection. This states a higher sensitivity for ToF-SIMS resulting in a lower limit of detection on a qualitative level.

This indicates a limited applicability for µ-XRF for low concentrations of particles. The comparatively low signal-to-noise ratio limits the detection to large particles/agglomerates of CeO_2. This, however, restricts the applicability of µ-XRF as a pre-analysis technique to samples with comparably high NP concentrations. Improved limits of detection could be expected via prolonged measurements, but extended measurement times for pre-analysis would be resulting and should be avoided where possible.

Although the limit of detection for the µ-XRF is not sufficient to detect small or very few particles, the identification of areas with higher particle content can also be a valuable information. Due to the wealth of signals in ToF-SIMS spectra originating from different low abundance molecules and their fragments, the mass resolution (in this case R = 4000 at *m/z* 103.93 (K_2CN^+) often is not sufficient to efficiently discriminate low-intensity particle signals in the mass range >100 u for biological samples. Therefore, the selection of signals is mostly limited to particle signals of higher abundance. However, by analysing an area with a high particle content by ToF-SIMS, selected according to the results of a previous µ-XRF analysis, the selection of suitable ion species can be reviewed and improved for further analyses. This provides a greater confidence on the assignment of particle signals and can help identifying signals without interferences for faster data evaluation. Furthermore, summing up of the particle signals from different ionization channels and isotopes can lead to a higher overall signal and a lower limit of detection.

Due to the high number of influencing factors a comparison of the limits of detection of µ-XRF to literature values is challenging. Limits of detection are highly affected by the element itself, matrix composition, density, and thickness of the sample. Therefore, the sample thickness of only 7 µm used in this work has a great effect on the limit of detection and makes the results hard to compare to values found in literature for pressed pellets or other dense material, where it was calculated to be in the lower µg/g range for bench-top µ-XRF.[283] Moreover, the cerium detection was limited to analysing the fluorescence radiation of the L-line, which is another drawback. Limits of detection for similarly heavy metals like Mo and W on polycarbonate for ToF-SIMS were found by Schnieders et al. of about $5x10^{10}$ atoms/cm² (at a minimum signal-to-noise ratio of 3) under static conditions.[284] Assuming a full monolayer coverage at $1x10^{15}$ atoms/cm² this literature value could be converted to a detection limit of about 50 ppm. These experiments clearly indicate a much lower limit of detection for ToF-SIMS 3D imaging analysis than for the µ-XRF analysis in this particular case (CeO_2 NP in lung tissue). Considering the different experimental setups from this and the literature study (Ar^+ primary ion beam for static spectrometry analysis *vs.* Bi_3^+ ion beam with O_2^+ sputtering for a 3D microanalysis), obviously the limits of detection are hardly comparable. However, the exact determination of limits of detection was outside the scope of this study and is a part of future studies along with the fabrication of reference samples for quantitative determination of nanomaterials.

7.3.4.3 Information Depth

The information depth for µ-XRF analysis is dependent on the sample composition but usually on the order of hundreds of micrometers[285]. On the one hand this means that especially for thin or porous samples like lung tissues the substrate is always analyzed together with the sample itself, which can potentially lead to interfering background signals. On the other hand, it can be safely assumed that signals from deeper layers of the sample are still detected. In contrast, ToF-SIMS provides excellent information depth of only the topmost monolayers of a material and information from deeper layers can only be obtained after a time-consuming sputtering process. This is one of the main reasons, why a pre-analysis method is necessary to select the appropriate area for ToF-SIMS analysis.

7.3.4.4 Time Requirements

Pre-analysis techniques are important to appropriately select promising regions of interest for the detection of nanoparticles in tissues. This helps to reduce the analysis time and cost for high-resolution ToF-SIMS 3D analysis. A pre-analysis by µ-XRF and microscopy provides an optical representation and elemental contrast without altering the sample and can improve the speed for ToF-SIMS 3D imaging analyses by excluding non-relevant areas from a selection. For example, the analysis time in this case for a 150 mm^2 area by µ-XRF was approximately 7.5 hours for 10 runs. Compared to a typical analysis time of a ToF-SIMS 3D imaging depth profile on 0.09 mm^2, which takes about 8 h, the additional time for an µ-XRF pre-analysis for the selection of a suitable area appears reasonable. This is particularly valid when considering the fact that a single µ-XRF analysis can be used as a pre-analysis for a complete tissue section, which allows several ToF-SIMS 3D imaging analyses on its area. Furthermore, by accelerating the navigation with the help of highly detailed microscopic images, especially for challenging samples with a high self-similarity, the overall time requirements get lower and the price per analysis drops. Both effects can lead to an increased relevance for ToF-SIMS 3D imaging analyses in the field of nanotoxicology.

7.4 Conclusion

The combination of pre-analyses by µ-XRF and microscopy prior to ToF-SIMS 3D Imaging was successfully shown for a CeO_2 NP containing lung tissue section. The results for the lateral distributions obtained by µ-XRF and ToF-SIMS 3D imaging are in good agreement with each other, proving the overall validity of this approach and enabling the sound selection of nanomaterial containing areas. Besides nanoparticle distribution further ToF-SIMS signal distributions (K_2CN^+, $K_3Cl_2^+$, $K_4PO_3^+$) elucidated the sample composition.

The combination of µ-XRF and ToF-SIMS allows to use the complimentary benefits of both powerful techniques. On the one hand, relatively fast µ-XRF pre-analysis allows the sensible selection of suitable regions of interest for ToF-SIMS 3D imaging analyses and allows a validation of the ToF-SIMS 3D imaging results. On the other hand, ToF-SIMS 3D imaging facilitates a somewhat slower, but more detailed high-resolution lateral analysis with superior limits of detection. The combined analysis approach appears to be suited especially for the analysis of heterogeneous nanoparticle-containing biological specimen, as exemplified here for the detection of CeO_2 NM212, a nanomaterial of high environmental relevance.

Future studies will include the determination of the limit of detection for both nanoparticle concentration and size to assess the performance of this approach.

Chapter 8

Detection of Zirconia Nanoparticles in Tissues by ToF-SIMS and Ion Beam Microscopy

Based on:

L. Veith, A. Vennemann, J. Böttner, D. Breitenstein, C. Engelhard, I. Estrela-Lopis, M. Wiemann, B. Hagenhoff, Detection of ZrO_2 Nanoparticles in Tissues by ToF-SIMS and Ion Beam Microscopy, *Nanomaterials Special Issue: Nanoparticles in Vivo and in Vitro Studies: A Collection of Parallel Approaches*, *Nanomaterials,* **2018**, *8(1)*, 44.

8. Detection of Zirconia Nanoparticles in Tissues by ToF-SIMS and Ion Beam Microscopy

8.1 Introduction

The detection of nanoparticles (NP) in tissue sections is an important prerequisite to determine potential risks for human health upon nanoparticle exposition. Due to their small sizes and low quantities the unambiguous detection and localization of NP is a demanding task. Time-of-Flight Secondary Ion Mass Spectrometry (ToF-SIMS) shows a high potential to detect a great variety of NP composed of inorganic materials along with the organic and inorganic composition of tissue thin sections. However, due to small masses of NP signal intensities are low and an unambiguous identification is challenging. Low signal-to-noise ratios complicate the recognition of isotopic patterns of the nanomaterial's elements. Furthermore, the size of a NP is smaller than a single pixel in the imaging analyses. Therefore, a second high resolution technique validating the identification and signal distribution of the ToF-SIMS results is desirable to prove the correct interpretation of the ToF-SIMS results at this stage of ToF-SIMS method development.

With a lateral resolution of the applied ToF-SIMS method of approximately 600 nm, we were able to identify fluorescent SiO_2 NP in lung tissue sections[220], and this localization was validated by fluorescence microscopy. However, for the vast majority of NP not carrying a fluorescent label or not showing plasmonic resonance, other high resolution techniques need to be explored if one aims to validate ToF-SIMS results. In this respect, ion beam microscopy (IBM) appears to be a well-suited technology, because its lateral resolution of ca. 1 µm is similar to the one of ToF-SIMS. The IBM technique combines the analysis of the particle-induced X-ray emission (PIXE) and the analysis of the energy of the backscattered particles, referred to as Rutherford backscattering spectrometry (RBS). This setup provides a high lateral resolution, undoubted element identification and their quantification [104, 105, 286]. As the technique is primarily non-destructive, successive analyses of tissue samples with IBM and ToF-SIMS should allow the detection of NP along with components of the biological matrix. ToF-SIMS detects molecules with a theoretically unlimited mass range. It allows the detection of organic as well as inorganic species, whereby molecular fragments are gathered from the surface which can be sputtered to obtain signals from deeper layers. IBM provides laterally resolved information on all element concentrations which, in contrast to ToF-SIMS, are always gathered from the whole sample depth. Thus, besides the benchmarking of the nanoparticle distribution complementary quantitative information should be accessible.

The aim of this study was to compare the results of ToF-SIMS and IBM analyses side-by-side using a 9–10 nm sized zirconium oxide (ZrO_2) NP distributed in lung tissue. Several reasons prompted us to choose this particular preparation: Firstly, own pilot experiments have shown that ZrO_2 NP gives rise to high signal intensities with both techniques, which is an important prerequisite for a comparative study. Secondly, ToF-SIMS and IBM should be compared with respect to their ability to detect small ZrO_2 NP in tissue, and to derive further information on the distribution of tissue components, such as the minor and trace elements by IBM, and elements and organic fragments by ToF-SIMS. Ideally, comparative analyses should be performed at exactly the same spot of the sample. Thirdly, the study, which is part of the special issue on “Nanoparticles in Vivo and in Vitro Studies: a Collection of Parallel Approaches”, shall also contribute to our understanding of the toxicological relevance of ZrO_2 NP in the lung, which acts as the main entry port for airborne nanomaterials into the body. ZrO_2 NP are used in coatings of self-cleaning stoves, in dental filler material, or implant materials[247], and the toxic effects of differentially coated ZrO_2 NP on alveolar macrophages and on rat and allergic mouse lung have been described in an accompanying publication[287]. Of note, ZrO_2 NP administered to the lung has been previously located mainly within alveolar macrophages by Raman microspectroscopy, hyperspectral microscopy, and immunocytochemistry[240, 287]. The present study comparing IBM and ToF-SIMS analyses of ZrO_2 NP distribution was carried out on rat lung tissue from this previous study [287].

8.2 Experimental Section

8.2.1 ZrO_2 Nanoparticles

ZrO_2 nanoparticles investigated in this study had a primary size of 9–10 nm according to electron microscopy, a surface area of 117 m^2/g, and were surface-coated with either tetraoxadecanoic acid or acrylate. A detailed characterization has been published previously[247].

8.2.2 Animal Experiments and Lung Tissue Preparation

Preparation of NP suspensions for instillation and instillation experiments were described before[287]. In brief, tetraoxadecanoic acid or acrylate-coated ZrO_2 NP were suspended in sterile H_2O, coated with rat serum albumin to prevent agglomeration, and further diluted in the instillation fluid (25 mM sodium bicarbonate gassed with 5% CO_2 to pH 7.4–7.8); 0.5 ml of this fluid containing 1.2 or 2.4 mg of either ZrO_2 NP was intratracheally instilled under isoflurane anaesthesia. Particle size in the instillation fluid as measured by optical tracking methods was 71–80 nm[287]. Animals used in this study were deeply anaesthetized with ketamine and xylazine, and bled via the Aorta descendens three days post-instillation. The left lung was inflated with 3 mL Cryomatrix (Thermo Shandon Ltd., Runcorn, UK), snap frozen in liquid nitrogen, and stored at −80 °C. Seven µm-thick cryo-sections were cut from the hilar region of the left lung. Sections investigated by ToF-SIMS were from rat lungs laden with 2.4 mg acrylate-coated ZrO_2 (see Figures 2–4), were mounted onto room tempered indium tin oxide-coated slides. After drying, sections were kept frozen and transferred to the pre-cooled chamber of the ToF-SIMS instrument, where they were dried completely under vacuum (pressure $< 1 \times 10^{-6}$ mbar). Sections used for IBM or for the comparison of IBM and ToF-SIMS were from rat lungs laden with 1.2 mg tetraoxadecanoic acid-coated ZrO_2 (see Figures 1 and 5–8). Sections were mounted onto a room temperature polypropylene foil fixed in custom made metal frames fitting into the IBM sample chamber. After drying, sections were transported on dry ice, immersed in cold methanol for 10 min, and dried prior to IBM investigation.

8.2.3 ToF-SIMS Analysis - Sputter Conditions

Measurements using O_2 sputtering were performed at a TOF-SIMS[5] (ION-TOF, Münster, Germany). An ion dose of Bi_3 at 25 keV of about 1.3×10^{11} ions was applied to an analysis raster of 200 × 200 µm² or rather 300 × 300 µm² with a pixel raster of 512 × 512 pixels. O_2 was used as a sputter ion at an energy of 1 keV. A total sputter dose of $2.2–4.7 \times 10^{15}$ ions was applied to a sputter raster size of 600 × 600 µm² or rather 900 × 900 µm². The delayed extraction mode in combination with non-interlaced sputtering at a cycle time of 70 µs resulting in a mass range up to 350 Da was used. The calibration of the mass spectra was facilitated by the use of Na^+, K^+, Na_2CN^+, Na_2CNO^+, and K_2OH^+. Mass resolutions ($R = m/\Delta m$) between 2000 and 7000 were achieved.

Measurements using Ar-cluster sputtering were performed at an upgraded TOF-SIMS[4] instrument (ION-TOF, Münster, Germany). An ion dose of Bi_3 at 25 keV of 1.67×10^9 ions was applied to an analysis raster of 300 × 300 μm^2 with a pixel raster of 256 × 256 pixels. Ar_{1000} clusters were used as sputter ions at an energy of 10 keV. A total sputter dose of 1.13×10^{13} ions was applied to a sputter raster size of 500 × 500 μm^2. The non-interlaced sputtering mode was used at a cycle time of 200 µs resulting in a mass range up to 1500 Da was used. The calibration of the spectra was facilitated by the use of the small organic ions (CH_3^+, $C_2H_5^+$, $C_3H_7^+$, and $C_4H_9^+$). Mass resolutions ($R = m/\Delta m$) between 3100 and 9000 were achieved.

The resulting 3D distributions of the signals were projected onto a 2D plane to enable a simple comparison of the signals.

8.2.4 Ion Beam Microscope Analysis

Ion beam measurements were conducted at the Leipzig Ion Nanoprobe LIPSION (Leipzig, Germany) of the Felix-Bloch-Institute for Solid State Physics. The measurements were executed with a proton beam of an energy of 2.25 MeV with a beam current of about 1 nA under vacuum conditions of 5.0×10^{-3} - 1.0×10^{-5} Pa. The spatial resolution was set to approximately 1 µm.

The PIXE spectroscopy employed a Canberra PIXE detector (Meriden, CT, USA) consisting of a high purity Germanium crystal (95 mm^2 active area) additionally covered with a 60 µm polyethylene layer, in order to avoid the penetration of backscattered protons.

For the RBS spectrometry measurements, the backscattered protons were detected using a passivated implanted planar silicon (PIPS)-detector from Canberra (Meriden, CT, USA). Rutherford backscattering spectrometry was applied to determine accumulated charge, atom density ($atoms/cm^2$) and element matrix composition (C, N, and O). These data were used as input parameters to calculate the concentration of ZrO_2 in ng/cm^2 from the integral intensity of the Zr K-line from the PIXE spectrum[105, 288, 289].

The data was collected using the MpSys Software (MARC Group of Prof Jamieson, Melbourne, Australia). The charge, density and element concentration were determined by fitting the experimental RBS and PIXE data in SIMNRA 6.0 (Mayer, M., Garching, Germany) and GeoPIXE5.1b software (CSIRSO, Melbourne, Australia).

8.3 Results and Discussion

The first part (2.1) will describe the detection of zirconium (Zr), phosphorous (P), and sulfur (S) within a ZrO_2 NP laden lung by IBM. Similarly, the subsequent parts (2.2 and 2.3) will describe a ToF-SIMS analysis together with inorganic and organic components. The last chapter (2.4) is devoted to the comparison of both techniques applied consecutively to the same position of a ZrO_2 containing tissue section. Representative examples showing the microscopic structure of cryo-sections as used here are shown in an accompanying paper of this special issues[240].

8.3.1 Typical IBM Results for an Individual Position

IBM analysis typically consists of two components. Particle-induced X-ray emission (PIXE) yields a signal distribution of elements by analyzing the X-ray emission upon proton bombardment. The Rutherford backscattering spectrometry (RBS) analyzes the energy of backscattered protons and provides information on the elemental composition, depth profile, the accumulated charge, and the thickness of a sample.

PIXE images of a ZrO_2 containing tissue section three days post-instillation are shown in Figure 8-1a where the signal distribution of phosphorus, sulfur, and zirconium is presented. The grey area indicates a region-of-interest (ROI) comprising the network of alveolar septa, which are main constituents of the lung parenchyma. The phosphorus image showed numerous elliptical structures of high intensity, with diameters up to 20 µm. While frequency, distribution, and size of the smaller structures most likely represented phosphate groups of the nuclear DNA within cell nuclei, larger spots may have been caused by type-2 pneumocytes, which contain phospholipid-rich lamellar bodies as lung surfactant precursors, or alveolar macrophages, which also may engulf portions of lung surfactant. Furthermore, it had to be taken into account that the K line from phosphorus and L line from zirconium coincided with each other. Therefore the phosphor distribution was partially influenced by the Lα emission from the Zr signal. The sulfur distribution showed an overall medium intensity in alveolar septa with higher intensity areas in P-rich (nuclear) regions. The sulfur distribution reflected sulfur-containing amino acids in proteins, and the highest intensity should be found where the local protein concentration is high. Again, nuclear structures bearing DNA-histone complexes may underlie this phenomenon. The zirconium distribution showed some intense areas all of which are associated with P- and S-rich regions. This, and the fact that the diameters of these patches were mostly below 10 µm, suggested a significant concentration of nanoparticles and/or small agglomerates in single cells, like alveolar macrophages and other cells of the alveolar septa. The concentration of NPs in different patches detected in various PIXE images was calculated. The PIXE and RBS spectra were extracted from the eight ROIs which mark the NP spots by the green circles (Figure 8-1a). After fitting the spectra, the obtained concentration of Zr elements was recalculated in terms of NP number per µm^2 assuming a density of ZrO_2 of 5680 kg/m^3 per NP with a mean size of 9 nm. Figure 8-1b shows the histogram of the NP loading across an evaluated lung section. The ROIs revealing a low NP loading of about 4000 NPs/µm^2 were associated with the alveolar septa, composed of type-1 and type-2 pneumocytes. A Higher NP loading of up to 40,000 NPs/µm^2 was found in ROIs 1 and 2 (Figure 8-1b). It may be suggested that the high loading of NPs occurs in alveolar macrophages, which were in the close vicinity of alveolar septum.

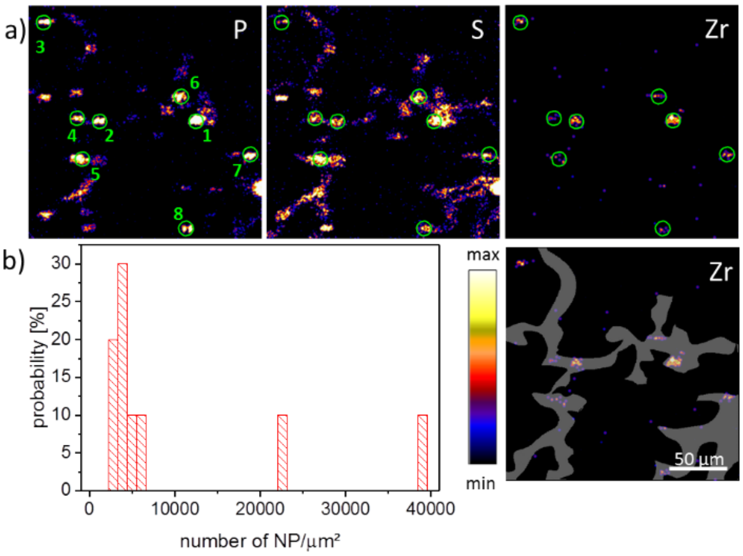

Figure 8-1: Particle-induced X-ray emission (PIXE) images of an air-dried lung section three days post instillation of ZrO_2 nanoparticles. (a) Signal distributions for P, S, and Zr, and Zr with superimposed region-of-interest (ROI, grey area). P and S are assumed to be cellular components found within the tissue at elevated levels. The Zr signals resemble accumulations of nanoparticles; (b) Histogram of nanoparticle (NP) loading across a population of cells indicated by the green ROIs 1-8.

8.3.2 Individual Position SIMS Analysis: Inorganic Depth Profiling

In the first step, three-dimensional ToF-SIMS analyses (3D ToF-SIMS) were carried out using O_2^+ sputtering, as this lowers the detection limit for the nanoparticles compared to Ar-cluster sputtering. O_2^+ sputtering ensures a high oxidation state of the Zr in the samples as it provides excess oxygen and fosters the secondary ion yield of the electropositive Zr for 3D ToF-SIMS analyses. Furthermore, due to the availability of O_2 during the analysis, the maximum ionization yield of the Zr specific ZrO^+ signal should be reached, which optimizes the signal-to-noise ratio for this channel.

ToF-SIMS analysis of a ZrO_2 NP-containing lung tissue section three days post NP administration is presented in Figure 8-2. The 3D data set was projected onto a 2D plane to enable a simple comparison of signal distributions. Typically, the K_2CN^+ signal (*m/z* 103.95, Figure 8-2a) is encountered in tissue material and used as a marker ion, if ToF-SIMS analysis of biomaterials is conducted with O_2^+ sputtering. The $K_4PO_3^+$ signal (*m/z* 234.91, Figure 8-2b) can be used as an indication for the phosphate distribution in K-rich tissue samples. In lung cells, this signal is therefore, mostly but not exclusively indicative of nuclear structures, and often surrounded by K_2CN^+, as shown in Figure 8-2d. The highest intensities of $K_4PO_3^+$ were found in alveolar edges, where phosphate-rich type-2 pneumocytes are quite often located. Thus, the $K_4PO_3^+$ distribution resembled the distribution of phosphate-rich areas as revealed by IBM and most likely represents phospholipids (*i.e.* type-2 pneumocytes) or nucleic acids (*i.e.* nuclei).

The ZrO^+ image (*m/z* 105.86, Figure 8-2c) presents the distribution of the nanoparticles. The diameters of ZrO^+ containing areas ranged from about 400 nm (corresponding to the size of a single pixel) up to 10 µm. As the primary particle size was 9 nm and the mean size of agglomerates within the instillation fluid amounted to 80 nm, the occurrence of more than one coherent ZrO^+-positive pixel suggests the presence of accumulated nanoparticle agglomerates. These agglomerations might have formed in the absence of cells, *i.e.* secondary to the instillation process when instillation fluid is resorbed and particles contact the lung surfactant or lung lining fluid.

A correlation analysis overlaying the different components in different colors was performed (Figure 8-2d). The correlation analysis presents the tissue material marker ion K_2CN^+ in red, the ZrO^+ signal in green, and the $K_4PO_3^+$ in blue. $K_4PO_3^+$ was predominantly found within the tissue at intense K_2CN^+ signals. This indicated a correlation with dense tissue and related most likely to compartments rich in nucleic acids or phospholipids. The ZrO_2 nanoparticles were likely to have accumulated alongside alveolar walls or were taken up by macrophage-like cells (Figure 8-2d, white arrow) typical sizes[290]. Some smaller signals appeared to be in the alveolar spaces. It cannot be excluded that some nanoparticles may have been displaced during the sectioning process. However, most of these were still associated with tissue material of lower signal intensity.

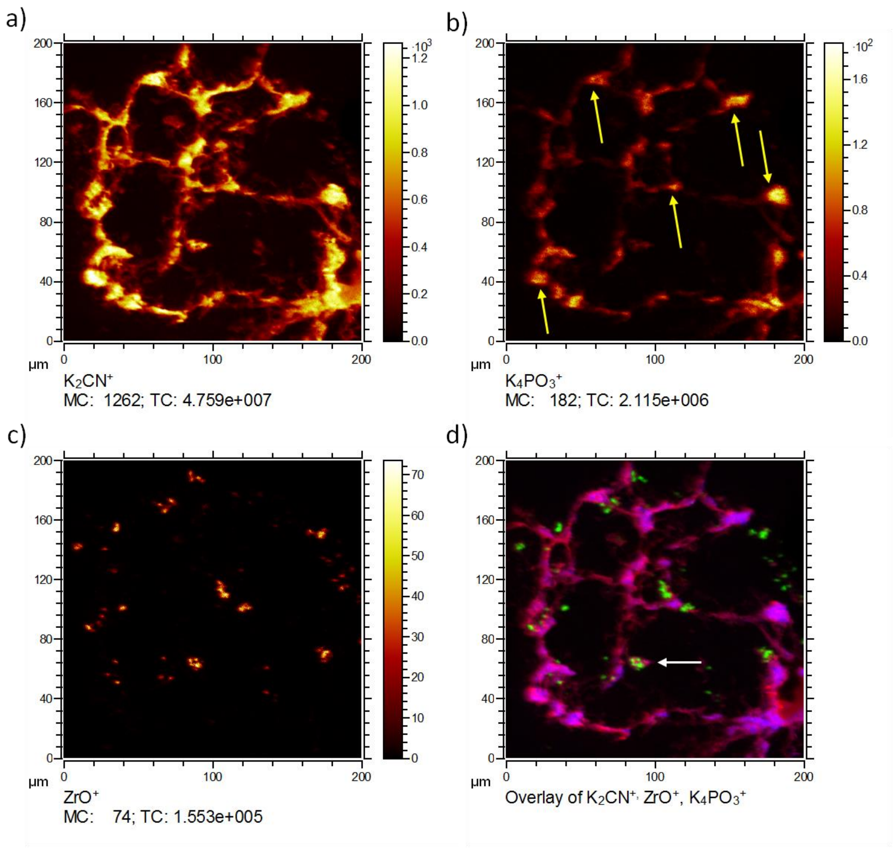

Figure 8-2: Time-of-flight Secondary Ion Mass Spectrometry (ToF-SIMS) three-dimensional (3D) analysis of an air-dried lung section three days post instillation of ZrO_2 nanoparticles. Lateral distributions of three secondary ions K_2CN^+, $K_4PO_3^+$, and ZrO^+ are shown upon O_2^+ sputtering. (a) K_2CN^+ shows the typical alveolar structure of a lung section; (b) $K_4PO_3^+$ is found as patches within the tissue and with high intensity in alveolar edges (yellow arrows); (c) ZrO^+ is concentrated in single patches attached to alveolar walls; the accumulations within the alveolar space most likely represent alveolar macrophages (white arrow); (d) A correlation analysis of all ions with K_2CN^+ in red, ZrO^+ in green, and $K_4PO_3^+$ in blue reveals the respective lateral signal distribution. The white arrow points to a macrophage-like cell. (MC: maximum counts per pixel, TC: total counts for the image).

8.3.3 Individual Position: Organic Depth Profiling

While the ToF-SIMS approach using O_2^+ sputtering results in excellent resolution and low detection thresholds, the extensive amount of fragmentation induced by the highly energetic O_2^+ primary ions on organic molecules is less ideal for the detection of organic molecules. In particular, large biomolecules are prone to fragmentation. However, studying the distribution of these molecules may contain valuable information on the effects of nanoparticles in tissues. Although it is expected to result in a higher detection limit, *e.g.* for Zr secondary ions, sputtering with large gas clusters leads to a much better yield for larger molecules and larger fragments[291, 292]. In particular, Ar-Cluster sputtering leads to less fragmentation along with higher sputter yields per ion compared to smaller clusters. In the next chapter, Ar_{1000}^+ cluster sputtering is carried out and results will be compared to those of O_2^+ sputtering.

Figure 8-3 shows the distribution of the typical signals of the same lung tissue section. Besides the tissue marker ion K_2CN^+ (a) and the NP-related ZrO^+(c), the distribution of the phosphatidylcholine head group $C_5H_{15}NPO_4^+$ (b) is shown as an example for larger organic molecular species, which are not extensively fragmented but detected intact. $C_5H_{15}NPO_4^+$ is a typical fragment of the important membrane lipid phosphatidylcholine. Consequently, the lateral distribution reveals the presence of this signal predominantly on the tissue material as expected for a membrane lipid. Several small patches of high intensity are visible. These most likely indicate the presence of pneumocyte type-2 cells, which produce the lung surfactant whose major phospholipid is phosphatidylcholine[140, 141]. Of note, $C_5H_{15}NPO_4^+$ was not associated with accumulated ZrO^+ (d), suggesting that (1.) these NP, despite their large BET surface do not extensively bind lung surfactant, and (2.) are not incorporated by type-2 pneumocytes.

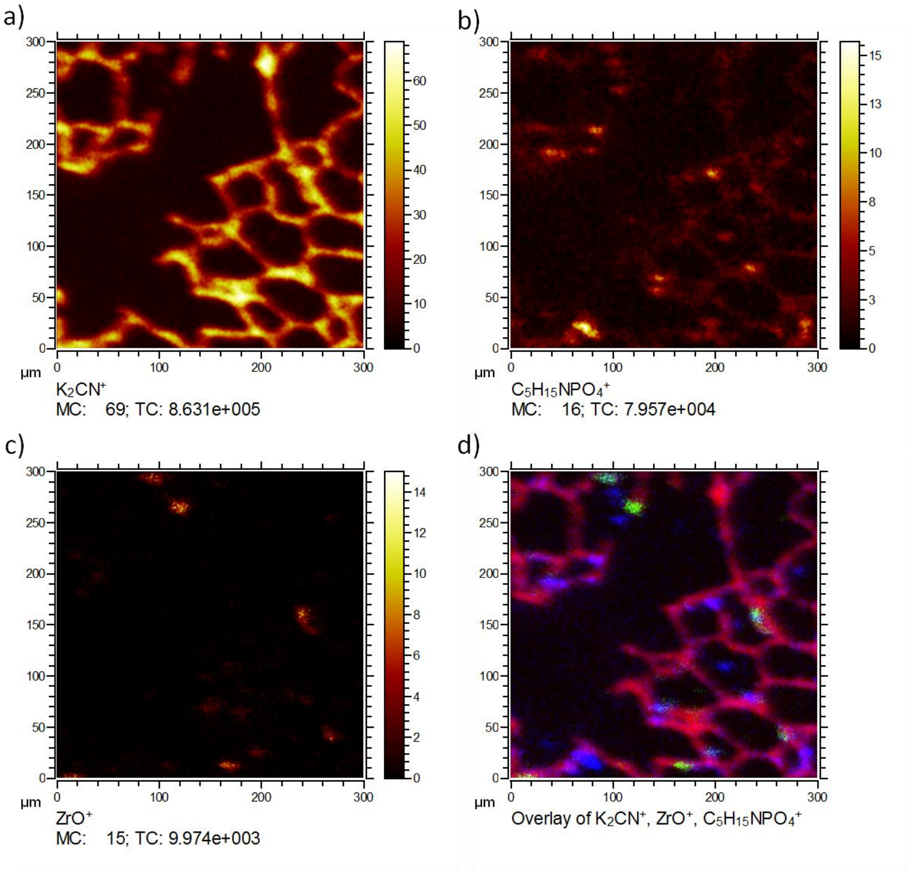

Figure 8-3: ToF-SIMS 3D analysis of an air-dried lung section three days post instillation of ZrO_2 nanoparticles. Lateral distributions of three secondary ions (a) K_2CN^+; (b) $C_5H_{15}NPO_4^+$ (m/z 184.09), and (c) ZrO^+ is shown upon Ar-cluster sputtering. A correlation analysis of all ions is shown in (d), with K_2CN^+ in red, the $C_5H_{15}NPO_4^+$ in blue and the ZrO^+ in green. The lateral distribution of K_2CN^+ shows the typical lung tissue structure. The phosphocholine fragment $C_5H_{15}NPO_4^+$ occurs in intense patches embedded in the septal structure (resembling the distribution of type-2 cells). The ZrO^+ signals occurs in discrete intense areas sized 10–20 µm, which appear attached to the septal structure 10 µm. (MC: maximum counts per pixel, TC: total counts for the image)

Figure 8-4 shows the distributions of signals most likely related to fragments of amino acids or other tissue molecules. While no distinct localization patterns were obtained for $C_2H_6N^+$ (*m/z* 44.05, Figure 8-4), most likely due to the ubiquitous occurrence of amino acids throughout all cells, other fragments ($C_3H_8N^+$ (*m/z* 58.06, Figure 8-4b), $C_4H_8N^+$ (*m/z* 70.07, Figure 8-4c), $C_5H_{12}N^+$ (*m/z* 86.10, Figure 8-4d)) show a pattern resembling that of $C_5H_{15}NPO_4^+$ from which they may have originated (at least in part). All these distributions reflect the septal structure of the lung tissue (compare K_2CN^+ in Figure 8-3a) and were not associated with ZrO_2 NP.

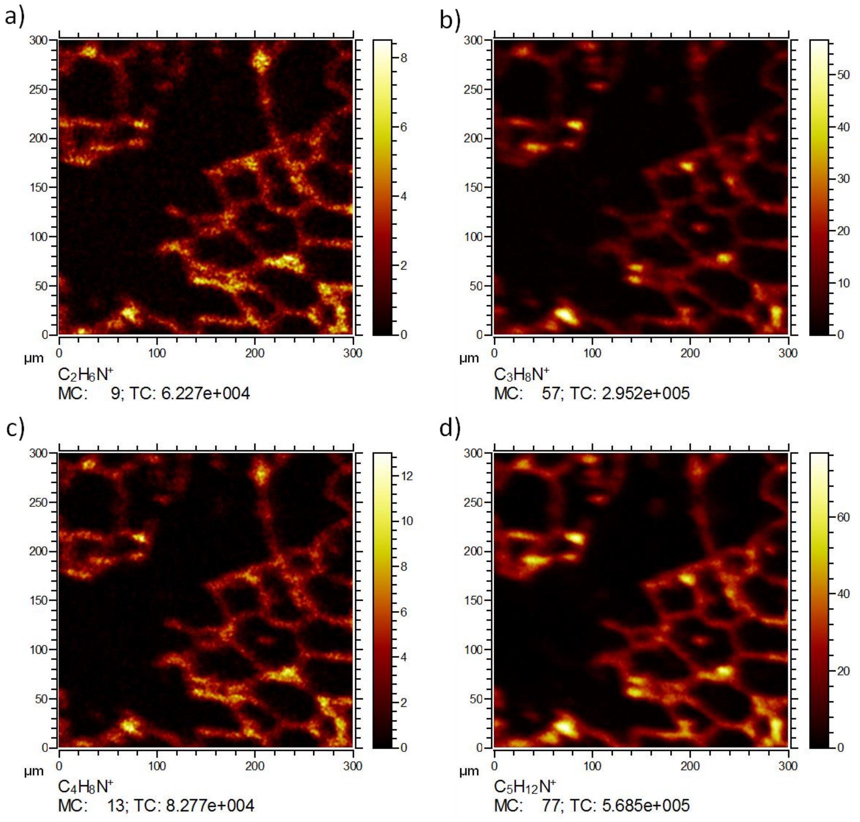

Figure 8-4: ToF-SIMS 3D analysis of an air-dried lung section three days post instillation of ZrO_2 nanoparticles. Same site of analysis as shown in Figure 8-3. The lateral distribution of (a) $C_2H_6N^+$; (b) $C_3H_8N^+$; (c) $C_4H_8N^+$; (d) $C_6H_{12}N^+$ obtained by Ar-cluster sputtering is shown. (a) $C_2H_6N^+$; (b) $C_3H_8N^+$; fragments in (a) and (c) and most likely originate from amino acids; fragments in (b) and (c) originate from phosphatidylcholine fragments. MC: maximum counts per pixel, TC: total counts for the image.

8.3.4 Sequential Analysis of Identical sample sites: Ion Beam Microscopy

To compare the results from IBM and ToF-SIMS analyses, a sequential analysis of the same site of ZrO_2 NP laden lung tissue was carried out. Since the ToF-SIMS using Ar-cluster or O_2 sputtering is a material-consuming (destructive) technique, IBM was done prior to ToF-SIMS analysis.

The IBM results show a notable distribution of P and S signals within the tissue section (Figure 8-5a,b). Phosphorus reveals a patch pattern within the continuously distributed sulfur. Both elements can be used to visualize lung tissue. The origin of the phosphorus signals are most likely phospholipids from the tissue membranes or/and the phosphate of the nucleic acid backbone, which are most concentrated within the nuclei of the cells. Sulfur is a general marker for cells as it occurs in almost all proteins and cytoskeleton. The alveolar walls can be identified by the sulfur distribution indicating the localization of the pneumocytes, macrophages and other cells. An enhanced occurrence of sulfur and phosphorus elements was found in the alveolar junctions. The intense spots of the P and S distributions in the alveolar junction region could indicate the presence of pneumocyte type-2 cells, where their location is normally expected.

Surprisingly, the central area showed a highly intense chlorine signal co-localized with S and P signals (Figure 8-5c,e). As the S signal was strongly interfered with by the intense Cl emission, it was regarded as an artifact. The P signal, however, was partially separated from the Cl signal (as can be seen from the emission spectrum (Figure 8-5f)) and indicated the validity of the assignment in the P image. Furthermore, some Ca and K signals were found at that position, which suggested the presence of a salt residue. Of note, no corresponding structure was detected by ToF-SIMS.

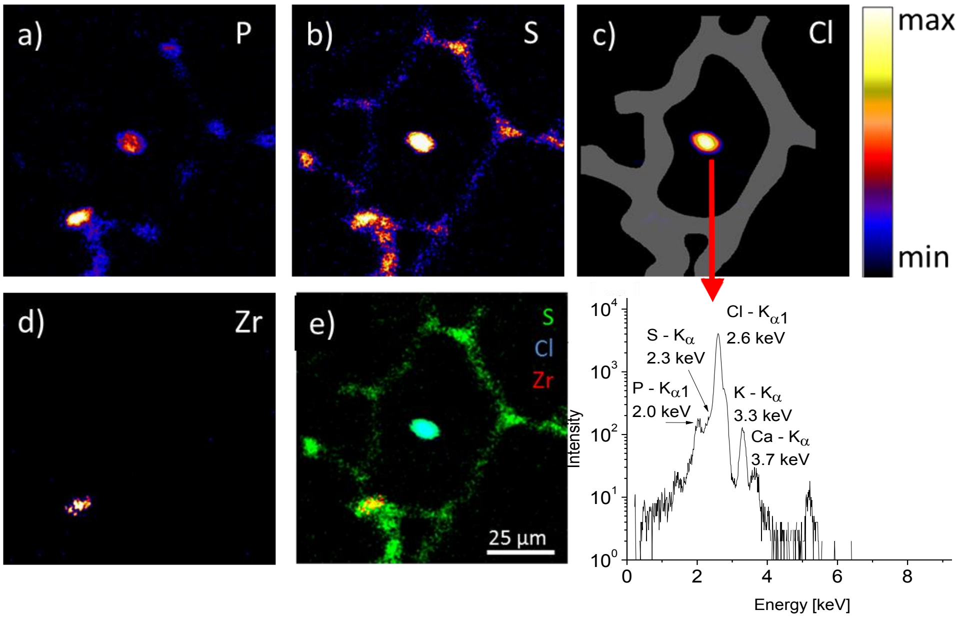

Figure 8-5: PIXE images of a ZrO_2 laden lung tissue section 3 days post instillation. Images (a)–(d) show the elemental distribution patterns of the elements P, S, Cl and Zr in lung tissue (field-of-view: 100 × 100 µm²). The overlay image (e) reveals the co-localization of S with Cl and Zr elements. The intense Cl signal (c) in the center interferes with the signal of S. The interference is revealed by the PIXE emission spectrum from the central area (f).

The zirconium distribution in Figure 8-5d only has a single area of notable intensity. This area is found within the tissue structure. This intense signal is found co-localized with the sulfur intensity. The higher sulfur as well as the phosphorous content compared with that in surrounding tissue could be usually found in macrophages. Furthermore the spatially defined appearance of the zirconium signal in a single area with a diameter of about

10 µm suggests also that the ZrO_2 nanoparticles were accumulated and might be contained in a macrophage. The achieved lateral resolution of about 1 µm revealed the substructure of Zr agglomerates inside a cell.

8.3.5 Sequential Analysis of Identical sample sites: ToF-SIMS

Results of the sequential analyses carried out first by IBM and then by ToF-SIMS are shown in Figures 6, 7 and 8. Treatment with the high-energy proton beam led to locally confined changes of the tissue surface (Figure 8-7a, f), which were used to identify the region-of-interest for the subsequent ToF-SIMS measurement. To maximize the signal yields especially for zirconium, we chose the more fragmenting O_2^+ ion beam sputter method for the comparative analysis, as it increases the yields for electropositive elements.

Furthermore, the lateral distributions of the signals from zirconium derived ions (ZrO_x^+) were analyzed. The respective isotopic signal distributions were used to ensure the identity of the Zr derived signals combined (compare Appendix, chapter 10, Figure 10-3). Figure 8-6 shows several intense Zr signals with diameters below 1 µm and up to 9 µm. As the pixel size limits the minimum diameter for signals to about 600 nm, smaller nanoparticles appeared as single pixels.

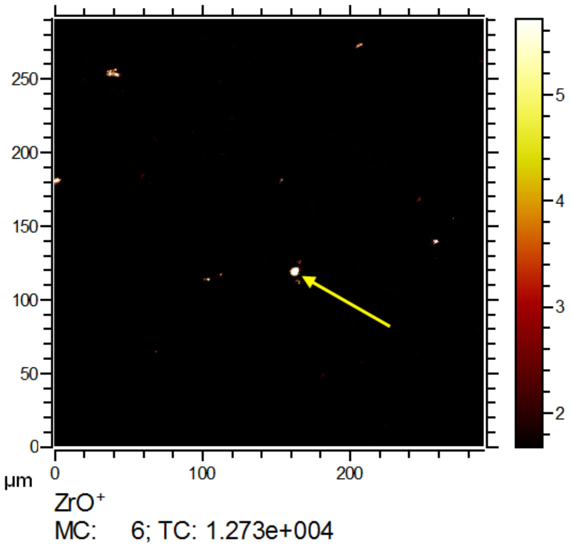

Figure 8-6: ToF-SIMS 3D analysis of the ZrO_2 NP containing lung section previously subjected to IBM measurement (see Figure 8-5). The lateral distribution of ZrO^+ reveals several intense signals; image contrast was enhanced to visualize small signals. The central ZrO^+ signal (yellow arrow) corresponds to the Zr signal in Figure 8-5. MC: maximum counts per pixel, TC: total counts for the image.

The lateral distribution of the total ion intensity reveals the overall structure of the analyzed tissue (Figure 8-7a). The area subjected to IBM analysis was easily recognized due to its reduced total secondary ion yield and the increased levels of small organic fragments (Figure 8-7f). To better compare ToF-SIMS and IBM images, we analyzed the distribution of S and P using SO_2^+ (*m/z* 63.97, Figure 8-7b) and PO^+ (*m/z* 46.96, Figure 8-7d) signals, which show lung tissue typical distributions if compared to the analyses shown above. A comprehensive image is presented as a RGB overlay, and shows the tissue-related SO_2^+ signal in blue, the phosphate signal in green, and the Zr oxide particle signal in red (Figure 8-7e). The RGB image shows agglomerated ZrO_2 NP in the tissue, revealing that most nanoparticles were directly associated with the tissue.

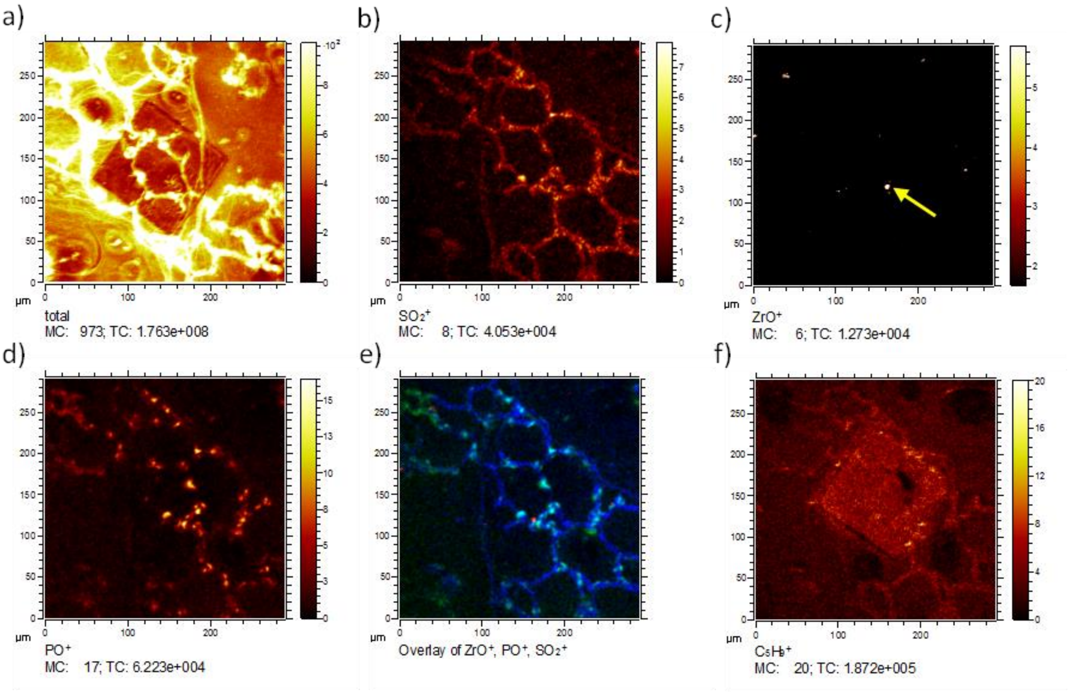

Figure 8-7 ToF-SIMS 3D analysis of a ZrO_2 NP containing lung section three days post-instillation, previously subjected to IBM measurement (see Figure 8-5). Lateral distributions of selected secondary ions. (a) The total ion distribution clearly indicates the area of proton bombardment during IBM analysis; (b) The SO_2^+ distribution resembles the tissue structure; (c) The lateral distribution of $^{90}ZrO^+$ reveals several intense signals. The central Zr signal (yellow arrow) corresponds to the Zr signal in Figure 8-5; (d) The PO+ image indicates the presence of phosphorus related compounds, which are typically nuclei and membrane lipids; (e) The red-green-blue (RGB) overlay shows the localization of the ZrO+ (red), PO+ (green) and SO_2^+ (blue); (f) The C_5H_9 distribution reveals elevated levels of small organic molecules indicating fragmentation of larger molecules in the area that was treated with the ion beam. (MC: maximum counts per pixel, TC: total counts for the image).

As the ion-beam-treated area was visible on ToF-SIMS images, we speculated that the sample was altered during the IBM analysis. A careful evaluation of ToF-SIMS analyses from ion-beam-treated sites showed that a slightly higher amount of small organic fragments (*e.g.* C_5H_9 (*m/z* 69.07, Figure 8-7f)) were detected in the ion beam-treated area and its close vicinity. It is conceivable that due to the impact of high energy protons, alterations of the organic material occurred. This would especially be the case with breaking of chemical bonds (similar to the proton beam writing process)[293, 294], as it would potentially explain the slightly elevated levels of small organic fragments. This shows that the IBM technique could at least gradually change the molecular composition of tissue components, and this aspect is of importance for the direct comparison of results.

8.3.6 Sequential Analysis of Identical Sample Sites: Comparison of IBM *vs.* ToF-SIMS

The results of the IBM analysis were compared to ToF-SIMS results (Figure 8-8). Elemental distributions of the X-ray emission on the left (a–c) were compared to the oxygen containing secondary ion distributions on the right (d–f). For S and SO_2^+, a high degree of correlation was obvious. With both techniques, a relatively weak signal distribution resembled the tissue structure with several higher intensity signals at the alveolar junctions. However, a difference was seen in the intense signal in the centre of the PIXE image (Figure 8-8a,b). This central structure consisted of K, Ca, P, and Cl that formed a salt deposit as a result of the preparation process, and appeared to be an artifact (see above). Also, an indication for this deposit was found neither on micrographs taken after the IBM analysis (not shown), nor in the ToF-SIMS analysis. As the structure was found in the centre of an alveolus, where it was not linked to the tissue material, we assumed that this salt deposit was moved during transport. However, the ToF-SIMS distributions of SO_2^+ and PO^+ both revealed an area similar in size and shape in the lower left corner of the alveolar structure (indicated by blue arrows) which might represent the salt deposit at its new position.

The P and PO^+ distribution overall was highly similar. However, the ToF-SIMS image apparently presented the intense signals of the IBM at a higher resolution and enabled a more detailed assessment of the substructure compared to the IBM.

With respect to the Zr/ZrO^+ signals, a coincidence was obtained for the highly intense signal spot seen in the lower parts of Figure 8-8c,f, although the detailed structure of Zr differed for both methods. Interestingly, the ToF-SIMS analysis revealed additional small

ZrO^+ signals (Figure 8-8f, yellow arrows), suggesting a lower limit of detection for the ToF-SIMS analysis along with a better lateral resolution. In fact, the routinely achieved lateral resolution in IBM experiments is about 1 µm, with limits of detection being in the parts-per-million (ppm) range[107, 288]. In contrast, a lateral resolution of less than 30 nm (under ideal conditions) and limits of detection in the ppm-ppb (parts-per-billion) range may be achieved with ToF-SIMS analysis[41, 295]. However, for both techniques the analytical parameters might still show some room for improvements. Prolonged measurement times and high performance detectors might lead to higher signal intensities and lower limits of detection in both instruments, but these were not available for this study. The application of high performance PIXE detectors will result in improved limits of detection and reduce measurement times. For ToF-SIMS, the amount of material eroded by the sputter beam per analysis cycle could be reduced to enhance the amount of material exposed to the analysis beam. It can be assumed that in particular for this analysis more signal intensity could be revealed under extended measurement conditions, since the majority of the signal intensity of the nanoparticles is only acquired towards the end of the analysis. Also, the lateral resolution (limited by the pixel number at a given Field-of-view to achieve a reasonably fast analysis) could be significantly improved for the detection of smaller agglomerates by selecting a smaller field-of-view or raising the pixel number per length unit. However, in favor of analyzing a larger area and measurement time constraints, a lateral resolution similar to the IBM was selected for this study.

The IBM provides element (inorganic) information[105, 106, 296, 297], whereas ToF-SIMS detects inorganic and organic species[80]. The detection of molecular information is only possible by ToF-SIMS, and works especially well for Ar-cluster ions. Therefore, in contrast to the IBM, ToF-SIMS also can serve for speciation analyses[298, 299]. However, the certainty for the identification for even smaller quantities of small nanomaterials (*i.e.* weak signals) in a complex matrix in ToF-SIMS is challenging, because interfering signals could hinder the separation of small partially overlapping NP-related signals in crowded mass spectra. In IBM, the certainty of the identification depends on the assignment and selection of the correct emission lines and is comparatively high.

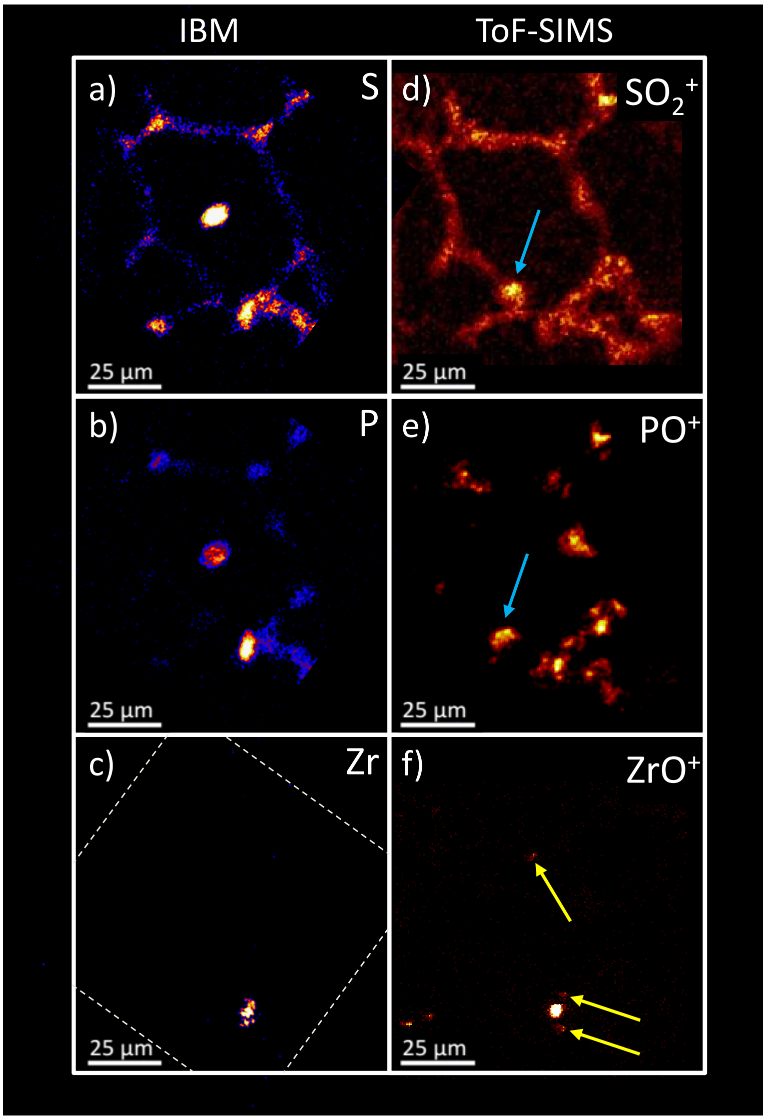

Figure 8-8: Comparison of the IBM and ToF-SIMS lateral distributions for selected signals side-by-side in the ZrO_2 NP containing lung section of Figure 8-5. The IBM distributions (a–c) were tilted to enable a direct comparison to the ToF-SIMS images (d–f, magnified). All distributions show a reasonably high congruency. The central, intense area of the S and P distribution from the IBM results has no direct equivalent in the ToF-SIMS results (interpreted as an artifact, see text). However, an area of similar size and shape is found in the lower left of the alveolar structure in the SO_2^+ and PO^+ ToF-SIMS images (blue arrows). The border of the field-of-view of the IBM is indicated by a dashed line in (c).

Quantitative information is routinely obtained for the IBM measurements without the need for standards or prior knowledge on the sample composition. In ToF-SIMS, quantitative information is only achievable by great efforts for simple, highly characterized samples (*e.g.* silicon wafers doped with boron) with the help of matrix-matched reference samples. For complex tissue samples, no simple routines exist for the quantification only based on ToF-SIMS results. Matrix effects are reported for ToF-SIMS as well, whereas the IBM does not suffer from severe matrix effects.

Depth information in IBM analyses is directly obtained via the RBS spectrometry, which also provides direct information if materials are internalized into cells or covered by tissue material. Depth resolutions of 100 nm are achieved[105, 106]. In ToF-SIMS, depth information is accessed via repeated cycles of surface analysis and surface erosion. Consequently, information on the internalization of materials can be obtained by interpreting the appearance of signals in successive scans. Furthermore, depth distributions as well as 3D distributions of signals can be analyzed. Depth resolutions of about 20 and 10 nm were published for low energy Cs and Ar-cluster ion sputtering of multilayer amino acid films, respectively[87]. However, this excellent resolution comes at the cost of analysis time, which is increasing with lower energy ions (*i.e.* lower sputter yields).

Both ToF-SIMS and ion beam microscopy need vacuum conditions. Vacuum compatibility for biological samples can be achieved by chemical fixation or analysis in the frozen state[249, 300, 301].

The influence of the proton beam on the samples integrity was estimated as the site of the analysis is visible in the successive ToF-SIMS images and a slightly higher amount of small organic fragments was found in the irradiated area. However, the extent of the damaging influence was not fully assessed during this study (compare Figure 8-7f). In comparison, ToF-SIMS 3D imaging, by nature, is a sample consuming technique. This is because signals can only be acquired if the respective materials are sputtered and ionized. Especially for the sensitive detection of low amounts of particle within complex matrices, it is necessary to obtain as much intensity as possible *i.e.* consume as much material as possible to ensure a comprehensive detection of all nanoparticles.

While ToF-SIMS already is a large and complex instrument, the IBM is still much more demanding in terms of size and complexity. Consequently, the pricing of commercially available ToF-SIMS instruments is much lower than for the IBM instruments, which need elaborate particle accelerators and a variety of detection components and are not available as complete kits. The time requirements for ToF-SIMS analyses of a single biological tissue area under the conditions shown here typically are in the order of 8–16 h (depending on the depth resolution and sample thickness). For the IBM measurements, approximately one hour is needed to reach ppm detection limits, however, these large-scale devices usually are shared among several different institutions. In consequence, “beam time” for measurements is precious.

In summary, each technique revealed the position of nanoparticle agglomerations within a tissue section individually and in a successive analysis of the same section. Significant congruency in the lateral distributions for phosphorous, sulfur and zirconium enabled a cross-validation of the results of both techniques. Due to its non-consuming nature and high lateral resolution, the IBM analysis enhances the confidence for the assignments of low intensity signals (especially for nanomaterials) in ToF-SIMS analyses and allows a cross-validation for early ToF-SIMS method development studies.

A promising strategy for achieving quantitative information in ToF-SIMS might be achieved by using IBM and ToF-SIMS for selected samples to obtain quantitative information and establish sensitivity factors for defined experimental conditions/sample matrices.

8.4 Conclusion

The detection of ZrO_2 nanoparticles in a real-world sample (lung tissue section from a toxicity study) was successfully shown by both ion beam techniques, IBM and ToF-SIMS. It is of toxicological relevance that with both techniques, ZrO_2 NP occurred in the lung as agglomerates, most probably in phagocytic cells, whereas no or negligible small quantities were associated with the lung epithelium. Each technique revealed the position of nanoparticle agglomerations within a tissue section individually. ToF-SIMS additionally could reveal the distribution of molecular fragment signals, which is in general not possible by IBM. Significant congruency in the lateral distributions was found for the localization of phosphorous-, sulfur-, and zirconium-containing compounds for both techniques enabling a cross-validation of the results. A comparison of the results revealed similar lateral resolutions with a slight advantage on the ToF-SIMS side. Lower limits of detection for the ToF-SIMS analysis were found in this study, whereas for the IBM measurement quantitative information is obtained without sample consumption. In consequence, a successive analysis by both techniques delivers an extremely high confidence on the validity of the distributions of nanomaterials and other components in tissue sections at high lateral resolutions, along with quantitative information.

Chapter 9

Concluding Remarks and Future Perspectives

9. Concluding Remarks and Future Perspectives

9.1 Conclusion

As the volume of production for nanoparticle-containing products grows, the release of nanoparticles into the environment will be increasing. Although the lung has been identified as one of the major entrance ports for nanoparticles into the human body, the fate and risks of nanoparticles upon inhalation are still largely unknown. Few analytical techniques are available that meet the analytical requirements for the localized detection of small amounts of nanoparticles within tissues. The potential of ToF-SIMS for such applications has been insufficiently explored. To fulfil the analytical requirements, several essential challenges for the detection of the nanoparticles by this technique have to be met. These are a high **sensitivity**, a **reliable** identification, **marker-free detection** and the combination of **high mass resolution** and **high lateral resolution** at the same time.

In the first part of this thesis, the strategies to meet these requirements were elucidated. Recommendations for adequate choices of secondary ion polarity, primary ion, sputter ion and operational modes were discussed and reference techniques were presented (see chapter 3.1 and 3.2). A review of the state-of-the-art literature revealed several applications of the ToF-SIMS technique to address biological/medical questions. However, most of the reported applications deal with the analyses of organic molecules or elemental species in dissolved or bulk form. So far, most of the publications dealing with nanoparticle detection are based on sector-field NanoSIMS instruments. Although this approach enables the parallel detection and identification of unknown nanoparticle species as well as organic species in tissue sections, only few ToF-SIMS studies on the detection of nanoparticles in tissues are published.

In the second part of the thesis, four individual studies were presented, which demonstrate a significant progress that was achieved here to reach the desired goal of a sensitive, reliable and marker-free nanoparticle detection by ToF-SIMS in lung tissue at high mass resolution and high lateral resolution. In each study, ToF-SIMS analyses were combined with carefully selected imaging techniques (depending on the type of nanomaterial) in order to cross-validate the detection of nanoparticles in the lung tissue sections.

In chapter 5, the general suitability of ToF-SIMS for the detection of oxidic nanoparticles in tissues was shown by the detection of rather large (*ca.* 220 nm), core/shell Fe_2O_3/SiO_2

particles in lung tissue, which are visible by bright-field microscopy. The lateral distributions of ^{28}Si (*m/z* 27.9769) and ^{56}Fe (*m/z* 55.9349) related signals were used to ensure the identification of the core/shell particles. The validity of the results was proven by a comparison with optical microscopy images of the particle-containing tissue. Furthermore, elemental distributions obtained with ToF-SIMS revealed the presence of false positive signals in dark-field microscopic images.

Smaller (*ca.* 30 nm) fluorescently labelled FITC-SiO_2 nanoparticles, which are not visible by usual microscopy, were used in the next study (chapter 6). They were detected in lung tissue sections by fluorescence microscopy and ToF-SIMS. The interpretation of the SiO_3^- (*m/z* 75.9622) ion distribution (analysed in the negative ion mode) represents the nanoparticle distribution and at the same time excludes any disturbing influence of frequently found polysiloxane inferences, such as SiO_x^+ in the positive ion polarity. A colocalization analysis based on the results of both techniques suggests a high amount of correlation between ToF-SIMS and fluorescence microscopy signals. Furthermore, the PO_3^- distribution indicated the presence of phosphate-rich areas (phospholipids producing type 2 pneumocytes or the locations of nuclei) in the sample. The evaluation of the advantages and disadvantages of both techniques suggested the preferential use of ToF-SIMS, due to its label-free detection and simultaneous, untargeted detection of components from the sample over the complete mass range.

In chapter 7 a follow-up study ToF-SIMS results are compared to those of the element specific µ-XRF analysis technique. The detection of rather large (*ca.* 155 nm) unlabelled CeO_2 nanoparticles by both techniques was aimed at proving the suitability of ToF-SIMS for the detection of unlabelled nanoparticles. The µ-XRF analysis of the complete lung tissue section enabled the selection of suitable areas for a comparison of the results of µ-XRF and ToF-SIMS. Representative central and peripheral areas from the tissue section including high and no signal intensities in the µ-XRF were analyzed by ToF-SIMS. Due to the lower lateral resolution of the µ-XRF (approx. 25 µm), the ToF-SIMS images with resolution of about 600 nm were binned to achieve a similar resolution for comparison purposes. Based on these binned images similarities of the signal distributions for both techniques were found and used for a cross-validation. Furthermore, in the areas without any µ-XRF intensity, ToF-SIMS could still detect signals for the CeO_2 nanoparticles (^{140}Ce at *m/z* 139.9054, ^{142}Ce at *m/z* 141.9092, ^{140}CeO at *m/z* 155.9003, ^{142}CeO at *m/z* 157.9042, $^{140}Ce_2O_2$ at *m/z* 311.8007, $^{140}Ce_2O_3$ at *m/z* 327.7956, $^{140}Ce^{142}CeO_3$ at *m/z* 329.7994) indicating a superior limit of detection. In spite of inferior limits of detection μ-XRF analysis can still serve as a valuable pre-characterization step prior to ToF-SIMS analysis. This holds true especially for heterogeneous biological specimen. This technique might also be used as a validation technique to a limited extent.

The last study included the label-free detection of unlabelled ZrO_2 nanoparticle with initial agglomerate sizes of 70-80 nm in a lung tissue section (chapter 8) by ToF-SIMS and IBM. The approach of this study allows a cross-validation of the results by showing significant congruency of the lateral distributions of sulphur, phosphorus and zirconium (ToF-SIMS signals: SO_2^+ at *m/z* 63.97, PO^+ at *m/z* 46.96, ZrO^+ at *m/z* 105.86). In a comparison, ToF-SIMS revealed a better lateral resolution (600 nm *vs.* 1000 nm for the IBM) and better limits of detection, whereas for IBM experiments quantitative information was obtained without the need for complete sample consumption. ToF-SIMS allows the detection of elemental ions and cluster such as K_2CN^+ at *m/z* 103.95, and molecular ions ($C_5H_{15}NPO_4^+$ at *m/z* 184.09) whereas IBM only reveals elemental distributions. As a result, ToF-SIMS turned out to be better suited for more general, untargeted analysis of samples, whereas the IBM should better be used for specific, defined samples when quantitative information is desired or further successive analyses at the same positions are planned.

In summary, the approaches show the gradual approach of ToF-SIMS to the marker-free detection of nanoparticles in tissues. With the optimized experimental conditions, a **sensitive** detection of different kinds of oxidic nanoparticles was established. The **reliability** of the identification was supported by a variety of additional analytical techniques, which prove the suitability of ToF-SIMS in every case. No false-positive signals were found for the ToF-SIMS analysis. Furthermore, ToF-SIMS was found to be superior in limit of detection, lateral resolution or number of detected species. Utilizing the delayed extraction mode, the detection of nanoparticles as well as organic signals at high **lateral resolution** and **high mass resolution** in a relatively short time was achieved. Altogether, the suitability of state-of-the-art ToF-SIMS instrumentation for the **marker-free detection** and identification of unlabelled nanoparticles was demonstrated.

9.2 Future Perspectives

The ToF-SIMS approach for the detection of several oxidic nanoparticles in lung tissue was successfully established. As the detection of the nanoparticles was successfully conducted in the challenging, low-density lung tissue, the application of ToF-SIMS to future in-vitro nanoparticle studies with single cells most likely. In the context of lung toxicity, the study of nanoparticle uptake into cells from different cell lines (*e.g.* alveolar macrophages) and their in-cell-localization appears a worthwhile goal.

The step to more dense tissue sections from other organs appears promising. With regards to the fate of nanoparticles in the body, especially the analysis of tissue from the stomach, intestines, kidney, liver, and brain might provide valuable insights on uptake and distribution mechanisms. Furthermore, expanding the application area of the ToF-SIMS approach appears promising for the investigation of particle uptake from the environment and the distributions within plants as the first level of the food chain.

Expanding the use of the approach in this thesis to the detection of other nanoparticle species (*e.g.* other oxides) is a logical consequence. With slight adjustments on the analytical parameters to ensure high sensitivity, the detection of metal nanoparticles is aspired. Furthermore, for the broad applicability of ToF-SIMS to toxicologically relevant real-world samples, the simultaneous detection of different nanoparticle species in a single sample is recommended, but was not followed in this study due to ethical considerations. New animal studies would have had to be conducted, which were not part of the ongoing larger nanoparticle toxicology project. However, as the identification of the Fe_2O_3/SiO_2 core/shell nanoparticles in the tissue was successfully shown, a simultaneous detection of different nanoparticle species in the same section appears to be easily manageable.

Another way to improve the value of the ToF-SIMS information is to conduct ultra high resolution analyses. As lateral resolution in this study were mostly limited to 400-600 nm (due to measurement time constraints), significant improvements on the resolution (of below 100 nm have been shown) are possible[85]. These ultra-high resolution analyses might provide images of the distributions of individual nanoparticles in tissues. With the help of these images, the composition of the relatively large, nanoparticle-signal areas observed in this thesis could be further elucidated. For the case of alveolar macrophages information could be provided on the uptake of different sized nanoparticles. High magnification images might also provide information on the size distributions of particles agglomerations within the tissue at different times after instillation and thereby might reveal the kinetics of agglomeration or uptake mechanisms.

Although optimized, full ToF-SIMS analyses take several hours to achieve a complete analysis with a sufficiently high signal intensity. Although pre-analysis by microscopy or µ-XRF might reduce the total time consumption for a complete study by suggesting promising areas, a shortening of the analysis time for individual analyses is aspired. If only the 2D location of the nanomaterials is of interest, an increased sputtering rate could be useful to erode the tissue components completely and to expose the particles in a fast fashion. Due to softer sputtering, gas cluster ions remove organic components faster than inorganic material. As a result, the nanoparticles are expected to be left behind intact on the substrate material and can be detected subsequently. In consequence, an analysis approach including prolonged GCIB sputtering cycles in the beginning with minimum damage to the particles is a conceivable option to further accelerate the complete process. Within this scope the use of oxygen GCIBs could provide the necessary O_2 to maintain high secondary ion yields for oxide particles while eroding the organic constituents in a fast fashion.

A benefit of the use of the GCIBs is that those allow molecular depth profiling. Optimizing the use of the GCIBs for little fragmentation should allow the detection of further molecular species along with the nanoparticles in a single analysis. This might provide valuable information on the effect of the nanoparticles in tissue. However, the combined use of the delayed extraction mode and GCIB was not available.

The limits of detection for nanoparticles in tissues for ToF-SIMS need to be assessed in order to fully estimate its usefulness in respect to other techniques. The comparison to the IBM data suggests the use of the non-destructive IBM as a reference technique for such studies. However, time slots for measurements are precious and not readily available.

Suitable reference materials of nanoparticles in organic matrices would be valuable for estimating the limits of detection as well as to simplify optimization by providing homogeneous distributions of nanoparticles in all 3 dimensions in space. The development of quantitative approaches based on reference materials seems promising. This is up to now one of the most severe limitations of ToF-SIMS.

Thus, by presenting several further analytical approaches to analyse nanoparticles in tissue, this thesis also indicates a number of interesting research goals towards the increased use of ToF-SIMS in the field of nanoparticle toxicology.

Chapter 10

Appendix

10. Appendix

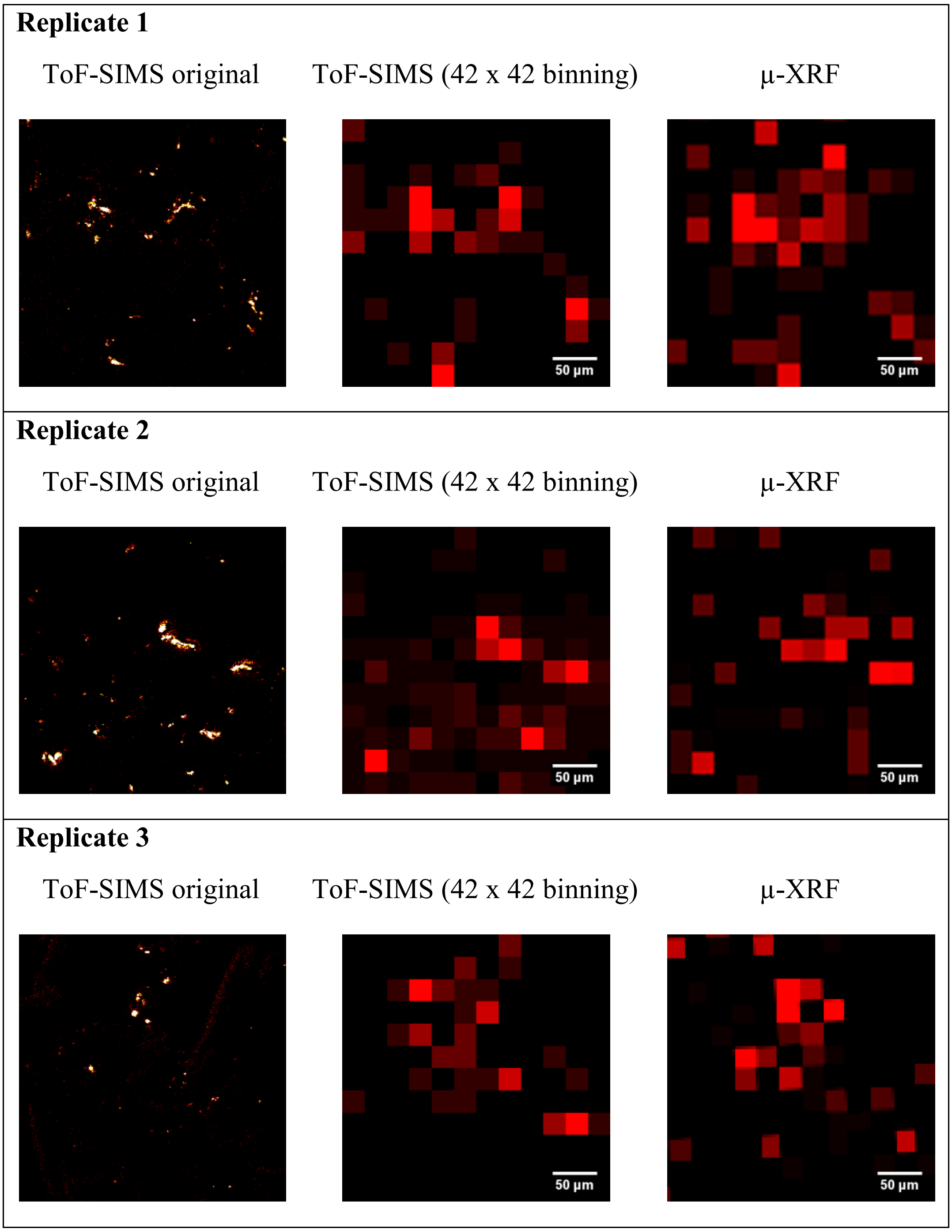

Figure 10-1: The three rows show replicate analyses of Ce-rich areas. The first column shows the original Ce ToF-SIMS signal distributions (at pixel sizes of about 670 x 670 nm²), whereas the central column shows the same signal distribution after formation of superpixels from 42 x 42 individual pixels (42x binning) to reduce the ToF-SIMS lateral resolution to the same value as the μ-XRF (pixel size of 25 x 25 μm²). The third column shows the μ-XRF signal distribution. Similar signal distribution are obtained by both techniques.

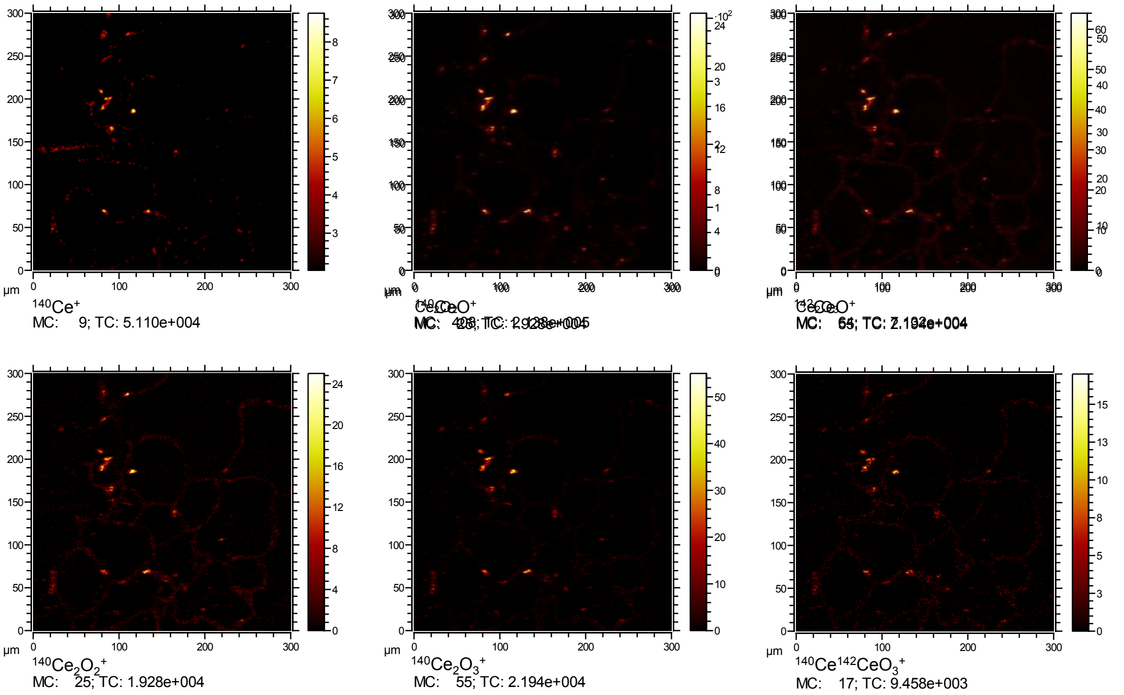

Figure 10-2: Colocalized signal distributions of $Ce_xO_y^+$ isotopes and clusters prove the correct assignment of Ce to the ToF-SIMS signals. Some slightly interfering influences can be observed (for $^{140}Ce^+$ and $^{140}Ce_2O_2^+$). The distribution of the intense areas matches throughout all the displayed secondary ion species.

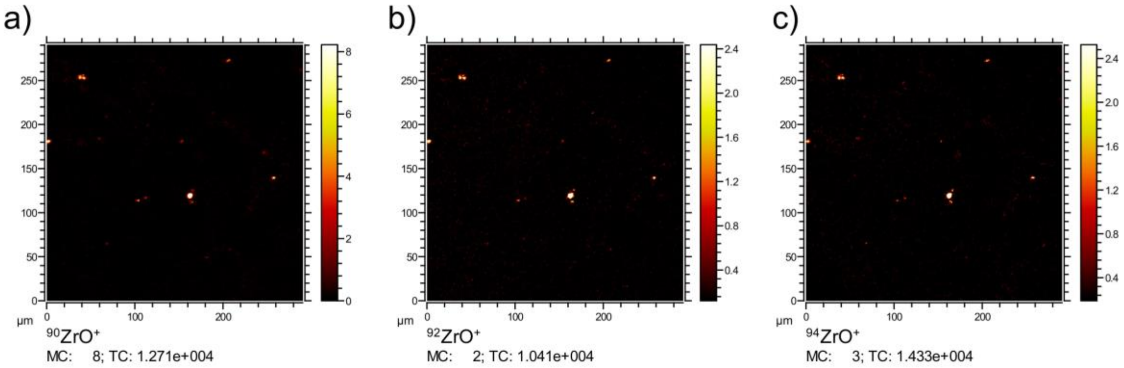

Figure 10-3: Correlating signal distributions of ZrO_2-related isotopes. The lateral signal distributions of the main ZrO isotopes $^{90}ZrO^{+}$ (a), $^{92}ZrO^+$ (b) and ^{94}ZrO (c) are in agreement with each other. Consequently, all the observed signals are derived from the same ZrO_2 source and the identity of the ZrO_2 particles is confirmed.

Chapter 11

References

11. References

1. Potocnik, J., Commission Recommendation of 18 October 2011 on the definition of nanomaterial. *OJ L* **2011,** *L 275* (38), 38-40.
2. Fernández-García, M.; Rodriguez, J. A., Metal Oxide Nanoparticles. In *Encyclopedia of Inorganic Chemistry*, John Wiley & Sons, Ltd: 2006.
3. Morris, J. E., Nanoparticle properties. In *Nanopackaging*, Springer: 2008; pp 93-107.
4. Hristozov, D.; Malsch, I., Hazards and Risks of Engineered Nanoparticles for the Environment and Human Health. *Sustainability* **2009,** *1* (4), 1161-1194.
5. Gunsolus, I. L.; Haynes, C. L., Analytical Aspects of Nanotoxicology. *Anal Chem* **2016,** *88* (1), 451-79.
6. *Novel Materials in the Environment: The Case of Nanotechnology, Royal Commission of Environmental Pollution*; TSO: 2008.
7. Chaudhry, Q.; Scotter, M.; Blackburn, J.; Ross, B.; Boxall, A.; Castle, L.; Aitken, R.; Watkins, R., Applications and implications of nanotechnologies for the food sector. *Food Addit Contam Part A Chem Anal Control Expo Risk Assess* **2008,** *25* (3), 241-58.
8. Jaroenworaluck, A.; Sunsaneeyametha, W.; Kosachan, N.; Stevens, R., Characteristics of silica-coated TiO2 and its UV absorption for sunscreen cosmetic applications. *Surf Interface Anal* **2006,** *38* (4), 473-477.
9. Afzal, A., Implantable zirconia bioceramics for bone repair and replacement: A chronological review. *Mater Express* **2014,** *4* (1), 1-12.
10. Becheri, A.; Dürr, M.; Lo Nostro, P.; Baglioni, P., Synthesis and characterization of zinc oxide nanoparticles: application to textiles as UV-absorbers. *J Nanopart Res* **2007,** *10* (4), 679-689.
11. Chang, Y.-N.; Zhang, M.; Xia, L.; Zhang, J.; Xing, G., The toxic effects and mechanisms of CuO and ZnO nanoparticles. *Materials* **2012,** *5* (12), 2850-2871.
12. Chen, Z.; Meng, H.; Xing, G.; Chen, C.; Zhao, Y.; Jia, G.; Wang, T.; Yuan, H.; Ye, C.; Zhao, F.; Chai, Z.; Zhu, C.; Fang, X.; Ma, B.; Wan, L., Acute toxicological effects of copper nanoparticles in vivo. *Toxicol Lett* **2006,** *163* (2), 109-20.
13. Wang, B.; Feng, W. Y.; Wang, T. C.; Jia, G.; Wang, M.; Shi, J. W.; Zhang, F.; Zhao, Y. L.; Chai, Z. F., Acute toxicity of nano- and micro-scale zinc powder in healthy adult mice. *Toxicol Lett* **2006,** *161* (2), 115-23.
14. Bakand, S.; Hayes, A.; Dechsakulthorn, F., Nanoparticles: a review of particle toxicology following inhalation exposure. *Inhal Toxicol* **2012,** *24* (2), 125-35.
15. Geiser, M.; Kreyling, W. G., Deposition and biokinetcis of inhaled nanoparticles. *Part Fibre Toxicol* **2010,** *7* (2), 2-17.
16. Geiser, M.; Rothen-Rutishauser, B.; Kapp, N.; Schurch, S.; Kreyling, W.; Schulz, H.; Semmler, M.; Im Hof, V.; Heyder, J.; Gehr, P., Ultrafine particles cross cellular membranes by nonphagocytic mechanisms in lungs and in cultured cells. *Environ Health Perspect* **2005,** *113* (11), 1555-60.
17. Yang, W.; Peters, J. I.; Williams, R. O., 3rd, Inhaled nanoparticles--a current review. *Int J Pharm* **2008,** *356* (1-2), 239-47.
18. Kreyling, W. G.; Geiser, M., Dosimetry of inhaled nanoparticles. In *Nanoparticles in medicine and environment*, Springer: 2010; pp 145-171.
19. Kirch, J.; Guenther, M.; Doshi, N.; Schaefer, U. F.; Schneider, M.; Mitragotri, S.; Lehr, C.-M., Mucociliary clearance of micro-and nanoparticles is independent

of size, shape and charge—an ex vivo and in silico approach. *J Controlled Release* **2012,** *159* (1), 128-134.

20. Grassian, V. H.; O'Shaughnessy P, T.; Adamcakova-Dodd, A.; Pettibone, J. M.; Thorne, P. S., Inhalation exposure study of titanium dioxide nanoparticles with a primary particle size of 2 to 5 nm. *Environ Health Perspect* **2007,** *115* (3), 397-402.
21. Donaldson, K.; Tran, L.; Jimenez, L. A.; Duffin, R.; Newby, D. E.; Mills, N.; MacNee, W.; Stone, V., Combustion-derived nanoparticles: a review of their toxicology following inhalation exposure. *Part Fibre Toxicol* **2005,** *2* (1), 10.
22. Stone, V.; Johnston, H.; Clift, M. J., Air pollution, ultrafine and nanoparticle toxicology: cellular and molecular interactions. *IEEE Trans Nanobioscience* **2007,** *6* (4), 331-40.
23. Oberdorster, G.; Maynard, A.; Donaldson, K.; Castranova, V.; Fitzpatrick, J.; Ausman, K.; Carter, J.; Karn, B.; Kreyling, W.; Lai, D.; Olin, S.; Monteiro-Riviere, N.; Warheit, D.; Yang, H.; Group, I. R. F. R. S. I. N. T. S. W., Principles for characterizing the potential human health effects from exposure to nanomaterials: elements of a screening strategy. *Part Fibre Toxicol* **2005,** *2* (1), 8.
24. Borm, P. J.; Robbins, D.; Haubold, S.; Kuhlbusch, T.; Fissan, H.; Donaldson, K.; Schins, R.; Stone, V.; Kreyling, W.; Lademann, J.; Krutmann, J.; Warheit, D.; Oberdorster, E., The potential risks of nanomaterials: a review carried out for ECETOC. *Part Fibre Toxicol* **2006,** *3* (1), 11.
25. Giesen, C.; Wang, H. A.; Schapiro, D.; Zivanovic, N.; Jacobs, A.; Hattendorf, B.; Schuffler, P. J.; Grolimund, D.; Buhmann, J. M.; Brandt, S.; Varga, Z.; Wild, P. J.; Gunther, D.; Bodenmiller, B., Highly multiplexed imaging of tumor tissues with subcellular resolution by mass cytometry. *Nat Methods* **2014,** *11* (4), 417-22.
26. Kempen, P. J.; Hitzman, C.; Sasportas, L. S.; Gambhir, S. S.; Sinclair, R., Advanced Characterization Techniques for Nanoparticles for Cancer Research: Applications of SEM and NanoSIMS for Locating Au Nanoparticles in Cells. *Mater Res Soc Symp Proc* **2013,** *1569*, 157-163.
27. Malucelli, E.; Fratini, M.; Notargiacomo, A.; Gianoncelli, A.; Merolle, L.; Sargenti, A.; Cappadone, C.; Farruggia, G.; Lagomarsino, S.; Iotti, S., Where is it and how much? Mapping and quantifying elements in single cells. *Analyst* **2016,** *141*, 5221-5235.
28. Georgantzopoulou, A.; Balachandran, Y. L.; Rosenkranz, P.; Dusinska, M.; Lankoff, A.; Wojewodzka, M.; Kruszewski, M.; Guignard, C.; Audinot, J. N.; Girija, S.; Hoffmann, L.; Gutleb, A. C., Ag nanoparticles: size- and surface-dependent effects on model aquatic organisms and uptake evaluation with NanoSIMS. *Nanotoxicology* **2013,** *7* (7), 1168-78.
29. Marquis, B. J.; Love, S. A.; Braun, K. L.; Haynes, C. L., Analytical methods to assess nanoparticle toxicity. *Analyst* **2009,** *134* (3), 425-39.
30. Jungnickel, H.; Laux, P.; Luch, A., Time-of-Flight Secondary Ion Mass Spectrometry (ToF-SIMS): A New Tool for the Analysis of Toxicological Effects on Single Cell Level. *Toxics* **2016,** *4* (1), 5.
31. Vickerman, J. C.; Briggs, D., *TOF-SIMS: Materials Analyysis by Mass Spectrometry*. 2nd ed.; IM Publications LLP: Chichester, 2013.
32. Fearn, S., Characterisation of biological material with ToF-SIMS: a review. *Mater Sci Tech Ser* **2014,** *31* (2), 148-161.
33. Rutten, F. J. M.; Roe, M. J.; Henderson, J.; Briggs, D., Surface analysis of ancient glass artefacts with ToF-SIMS: A novel tool for provenancing? *Appl Surf Sci* **2006,** *252* (19), 7124-7127.
34. Liu, H.; Ye, X.; Zhou, X.; Huang, J.; Wang, F.; Zhou, X.; Wu, W.; Jiang, X.; Sui, Z.; Zheng, W., Subsurface defects characterization and laser damage

performance of fused silica optics during HF-etched process. *Opt Mater* **2014,** *36* (5), 855-860.

35. Sui, T.; Song, B.; Dluhos, J.; Lu, L.; Korsunsky, A. M., Nanoscale chemical mapping of Li-ion battery cathode material by FIB-SEM and TOF-SIMS multi-modal microscopy. *Nano Energy* **2015,** *17*, 254-260.
36. Iuraş, A.; Scurr, D. J.; Boissier, C.; Nicholas, M. L.; Roberts, C. J.; Alexander, M. R., Imaging of crystalline and amorphous surface regions using time-of-flight secondary-ion mass spectrometry (ToF-SIMS): application to pharmaceutical materials. *Anal Chem* **2016,** *88* (7), 3481-3487.
37. Holzlechner, G.; Sobol, O.; Böllinghaus, T.; Unger, W., Imaging ToF-SIMS as a Chemical Metrology Tool to Support Material and Analytical Science. In *Materials for Energy Infrastructure*, Udomkichdecha, W.; Mononukul, A.; Böllinghaus, T.; Lexow, J., Eds. Springer Singapore: Singapore, 2016; pp 63-72.
38. Weng, L. T.; Chan, C.-M., Characterisation of polymeric materials. In *TOF-SIMS: Materials analysis by mass spectrometry*, 2nd ed.; Vickerman, J. C.; Briggs, D., Eds. IM Publishings LLP and SurfaceSpectra Limited: Chichester, 2012; pp 503-530.
39. Hagenhoff, B., High Resolution Surface Analysis by TOF-SIMS. *Mikrochim Acta* **2000**.
40. Sigmund, P., Mechanisms and theory of physical sputtering by particle impact. *Nucl Instrum Methods Phys Res, Sect B* **1987,** *27* (1), 1-20.
41. Senoner, M.; Unger, W. E. S., SIMS imaging of the nanoworld: applications in science and technology. *J Anal At Spectrom* **2012,** *27* (7), 1050-1068.
42. Muramoto, S.; Brison, J.; Castner, D. G., Exploring the surface sensitivity of TOF-secondary ion mass spectrometry by measuring the implantation and sampling depths of Bi(n) and C60 ions in organic films. *Anal Chem* **2012,** *84* (1), 365-72.
43. Van Vaeck, L.; Adriaens, A.; Gijbels, R., Static Secondary Ion Mass Spectrometry (S-SIMS) Part 1. Methodology and structural interpretation. *Mass Spectrom Rev* **1999,** *18*, 1-47.
44. Postawa, Z.; Czerwinski, B.; Szewczyk, M.; Smiley, E. J.; Winograd, N.; Garrison, B. J., Microscopic insights into the sputtering of Ag {111} induced by C60 and Ga bombardment. *J Phys Chem B* **2004,** *108* (23), 7831-7838.
45. Mahoney, C. M., Cluster secondary ion mass spectrometry of polymers and related materials. *Mass Spectrom Rev* **2010,** *29* (2), 247-93.
46. Vickerman, J. C.; Briggs, D., *ToF-SIMS: Surface Analysis by Mass Spectrometry*. IMPublication: Chichester, 2001.
47. Benninghoven, A.; Rüdenauer, F. G.; Werner, H. W., *Secondary Ion Mass Spectrometry*. John Wiley & Sons: 1987; Vol. 86.
48. Cooks, R. G.; Busch, K. L., Matrix effects, internal energies and MS/MS spectra of molecular ions sputtered from surfaces. *Int J Mass Spectrom Ion Phys* **1983,** *53*, 111-124.
49. Garrison, B. J., Molecular desorption induced by heavy particle bombardment of solids. *Int J Mass Spectrom Ion Phys* **1983,** *53*, 243-254.
50. Benninghoven, A., Molecular Secondary Ion Emission. In *Secondary Ion Mass Spectrometry SIMS II: Proceedings of the Second International Conference on Secondary Ion Mass Spectrometry (SIMS II) Stanford University, Stanford, California, USA August 27–31, 1979*, Benninghoven, A.; Evans, C. A.; Powell, R. A.; Shimizu, R.; Storms, H. A., Eds. Springer Berlin Heidelberg: Berlin, Heidelberg, 1979; pp 116-121.
51. Vickerman, J.; Brown, A.; Reed, N., *Spectrometry, Secondary Ion Mass*. Oxford University Press: New York: Oxford, New York, 1989.

52. Plog, C.; Wiedmann, L.; Benninghoven, A., Empirical formula for the calculation of secondary ion yields from oxidized metal surfaces and metal oxides. *Surface Science* **1977,** *67* (2), 565-580.
53. Riedel, M.; Düsterhöft, H.; Kuska, J. P., Models of energy dependence of the secondary ion yield compared with experimental results. *Rapid Commun Mass Spectrom* **1997,** *11* (6), 667-672.
54. Benninghoven, A., Some aspects of secondary ion mass spectrometry of organic compounds. *Int J Mass Spectrom Ion Phys* **1983,** *53*, 85-99.
55. Benninghoven, A. In *Secondary Ion Mass Spectrometry of Organic Compounds (Review)*, Berlin, Heidelberg, Springer Berlin Heidelberg: Berlin, Heidelberg, 1983; pp 64-89.
56. Cooks, R.; Busch, K., Matrix effects, internal energies and MS/MS spectra of molecular ions sputtered from surfaces. *Int J Mass Spectrom Ion Phys* **1983,** *53*, 111-124.
57. Benninghoven, A., Chemical Analysis of Inorganic and Organic Surfaces and Thin Films by Static Time-of-Flight Secondary Ion Mass Spectrometry (TOF-SIMS). *Angew Chem Int Ed Engl* **1994,** *33*, 1023-1043.
58. Hagenhoff, B.; van Leyen, D.; Niehuis, E.; Benninghoven, A., Time-of-flight secondary ion mass spectrometry of insulators with pulsed charge compensation by low-energy electrons. *J Vac Sci Technol, A* **1989,** *7* (5), 3056-3064.
59. ION-TOF GmbH, *TOF.SIMS^5 product brochure*. Münster, 2017.
60. Hill, R., Analysis beams used in ToF-SIMS. In *TOF-SIMS: Surface Analysis by Mass Spectrometry*, 2nd ed.; Vickerman, J. C.; Briggs, D., Eds. IM Publication LLP and SurfaceSpectra Limited: 2013; pp 271-275.
61. Todd, P. J.; Schaaff, T. G.; Chaurand, P.; Caprioli, R. M., Organic ion imaging of biological tissue with secondary ion mass spectrometry and matrix-assisted laser desorption/ionization. *J Mass Spectrom* **2001,** *36* (4), 355-69.
62. Davies, N.; Weibel, D. E.; Blenkinsopp, P.; Lockyer, N.; Hill, R.; Vickerman, J. C., Development and experimental application of a gold liquid metal ion source. *Appl Surf Sci* **2003,** *203-204*, 223-227.
63. Benguerba, M.; Brunelle, A.; Della-Negra, S.; Depauw, J.; Joret, H.; Le Beyec, Y.; Blain, M. G.; Schweikert, E. A.; Ben Assayag, G.; Sudraud, P., Impact of slow gold clusters on various solids: nonlinear effects in secondary ion emission. *Nucl Instrum Methods Phys Res, Sect B* **1991,** *62* (1), 8-22.
64. Kollmer, F., Cluster primary ion bombardment of organic materials. *Appl Surf Sci* **2004,** *231-232*, 153-158.
65. Clampitt, R.; Jefferies, D., Miniature ion sources for analytical instruments. *Nucl Instrum Methods* **1978,** *149* (1-3), 739-742.
66. Schnieders, A.; Hagenhoff, B.; Rading, D. *Short Course SIMS: Fundamentals*; SIMS Europe Conference Münster, 2002.
67. Wittmaack, K., Oxygen-concentration dependence of secondary ion yield enhancement. *Surface Science* **1981,** *112*, 168-180.
68. Matsuo, J.; Ninomiya, S.; Nakata, Y.; Honda, Y.; Ichiki, K.; Seki, T.; Aoki, T., What size of cluster is most appropriate for SIMS? *Appl Surf Sci* **2008,** *255* (4), 1235-1238.
69. Yamada, I.; Matsuo, J.; Toyoda, N.; Kirkpatrick, A., Materials processing by gas cluster ion beams. *Mater Sci Eng: R: Reports* **2001,** *34* (6), 231-295.
70. Seki, T.; Matsuo, J.; Takaoka, G. H.; Yamada, I., Generation of the large current cluster ion beam. *Nucl Instrum Methods Phys Res, Sect B* **2003,** *206*, 902-906.

71. Swenson, D.; Atoms, Measurement of averages of charge, energy and mass of large, multiply charged cluster ions colliding with atoms. *Nucl Instrum Methods Phys Res, Sect B* **2004,** *222* (1-2), 61-67.
72. Swenson, D., Analysis of charge, mass and energy of large gas cluster ions and applications for surface processing. *Nucl Instrum Methods Phys Res, Sect B* **2005,** *241* (1-4), 599-603.
73. Wittmaack, K., Basic requirements for quantitative SIMS analyis using cesium bombardment and detection of MCs^+ secondary ions. *Nucl Instrum Methods Phys Res, Sect B* **1992,** *64*, 621-625.
74. ION-TOF GmbH, TOF-SIMS Help. *ION-TOF GmbH, TOF-SIMS Help* **2016,** *Version 6.7.905*.
75. Breitenstein, D. Strukturelle Organisation des alveolaren Surfactant: Tensiometrische und oberflächenmassenspektrometrische Untersuchungen zur Lipidspezifität. Dissertatition, Westfälische Wilhelms-Universittät Münster, Münster, 2004.
76. Sodhi, R. N., Time-of-flight secondary ion mass spectrometry (TOF-SIMS): versatility in chemical and imaging surface analysis. *Analyst* **2004,** *129* (6), 483-7.
77. Niehuis, E.; Grehl, T., Depth profiling of inorganic materials. In *ToF-SIMS: Materials Analysis by Mass Spectrometry*, 2nd ed.; IM Publications LLP: Chichester, 2013; pp 613-635.
78. Lee, J. L.; Gilmore, I. S.; Seah, M. P.; Fletcher, I. W., Topography and field effects in secondary ion mass spectrometry--part I: conducting samples. *J Am Soc Mass Spectrom* **2011,** *22* (10), 1718-28.
79. Lee, J. L. S.; Gilmore, I. S.; Fletcher, I. W.; Seah, M. P., Topography and field effects in the quantitative analysis of conductive surfaces using ToF-SIMS. *Appl Surf Sci* **2008,** *255* (4), 1560-1563.
80. Vickerman, J. C.; Briggs, D., *TOF-SIMS: Materials Analysis by Mass Spectrometry*. 2nd ed.; IM Publications LLP: Chichester, 2013.
81. Radionova, A.; Filippov, I.; Derrick, P. J., In pursuit of resolution in time-of-flight mass spectrometry: A historical perspective. *Mass Spectrom Rev* **2016,** *35* (6), 738-757.
82. Niehuis, E.; Heller, T.; Jürgens, U.; Benninghoven, A., Surface and trace analysis by high-resolution time-of-flight secondary ion mass spectrometry. *J Vac Sci Technol, A* **1989,** *7* (3), 1823-1828.
83. Lee, J. L. S.; Gilmore, I. S.; Seah, M. P.; Levick, A. P.; Shard, A. G., Topography and field effects in secondary ion mass spectrometry Part II: insulating samples. *Surf Interface Anal* **2012,** *44* (2), 238-245.
84. Touboul, D.; Kollmer, F.; Niehuis, E.; Brunelle, A.; Laprevote, O., Improvement of biological time-of-flight-secondary ion mass spectrometry imaging with a bismuth cluster ion source. *J Am Soc Mass Spectrom* **2005,** *16* (10), 1608-18.
85. Kollmer, F.; Paul, W.; Krehl, M.; Niehuis, E., Ultra high spatial resolution SIMS with cluster ions - approaching the physical limits. *Surf Interface Anal* **2013,** *45* (1), 312-314.
86. Kubicek, M.; Holzlechner, G.; Opitz, A. K.; Larisegger, S.; Hutter, H.; Fleig, J., A novel ToF-SIMS operation mode for sub 100 nm lateral resolution: Application and performance. *Appl Surf Sci* **2014,** *289* (100), 407-416.
87. Wehbe, N.; Tabarrant, T.; Brison, J.; Mouhib, T.; Delcorte, A.; Bertrand, P.; Moellers, R.; Niehuis, E.; Houssiau, L., TOF-SIMS depth profiling of multilayer amino-acid films using large Argon cluster Ar_n^+, C_{60}^+ and Cs^+ sputtering ions: A comparative study. *Surf Interface Anal* **2013,** *45* (1), 178-180.

88. Dong, X.; Gusev, A.; Hercules, D. M., Characterization of polysiloxanes with different functional groups by time-of-flight secondary ion mass spectrometry. *J Am Soc Mass Spectrom* **1998,** *9* (4), 292-8.
89. Polydimethylsiloxane Spectra. *Iontof Surfacelab 6.7 Spectra Library* **2016**.
90. Kanyal, S. S.; Jensen, D. S.; Zhu, Z.; Linford, M. R., Silicon (100)/SiO2 by ToF-SIMS. *Surf Sci Spectra* **2015,** *22* (2), 1-6.
91. Demirev, P. A., Particle-Induced Desorption in Mass Spectrometry. *Mass Spectrom Rev* **1995,** *14*, 309-326.
92. Evennett, P. J.; Hammond, C., *Microscopy Overview*. 2nd ed.; Elsevier: Amsterdam, The Netherlands: 2005; p 32-41.
93. Sluder, G.; Nordberg, J. J., *Microscope Basics*. Elsevier Inc: 2003; Vol. 72, p 1-10.
94. Vander Voort, G. W., *Optical Microscopy*. Elsevir Academic Press: 2005.
95. Bass, M., *Devices, measurements, and properties*. 2nd ed.; McGraw-Hill Inc.: New York, 1994; Vol. 2.
96. Davidson, M. W.; Abramowitz, M., *Optical Microscopy*. John Wiley & Sons, Inc.: New York, NY, USA: 2002.
97. Huang, Y.; Kim, D. H., Dark-field microscopy studies of polarization-dependent plasmonic resonance of single gold nanorods: rainbow nanoparticles. *Nanoscale* **2011,** *3* (8), 3228-32.
98. Hu, M.; Novo, C.; Funston, A.; Wang, H.; Staleva, H.; Zou, S.; Mulvaney, P.; Xia, Y.; Hartland, G. V., Dark-field microscopy studies of single metal nanoparticles: understanding the factors that influence the linewidth of the localized surface plasmon resonance. *J Mater Chem* **2008,** *18* (17), 1949-1960.
99. Spring, K. R., *Fluorescence Microscopy*. Marcel Dekker Inc.: New York, 2003.
100. Haschke, M.; Rossek, U.; Tagle, R.; Waldschläger, U., Fast elemental mapping with micro-XRF. *Adv X Ray Anal* **2012,** *55*, 286-298.
101. Van Grieken, R.; Injuk, J. In *Current applications of XRF and micro-XRF techniques in environmental and industrial fields*, Industrial and environmental applications of nuclear analytical techniques, Vienna, IAEA: Vienna, 1998; p 29.
102. Van Grieken, R.; Markowicz, A., *Handbook of X-ray Spectrometry*. CRC Press: 2001.
103. Reinert, T.; Spemann, D.; Morawski, M.; Arendt, T., Quantitative trace element analysis with sub-micron lateral resolution. *Nucl Instrum Methods Phys Res, Sect B* **2006,** *249* (1-2), 734-737.
104. Lichtenstein, D.; Ebmeyer, J.; Meyer, T.; Behr, A. C.; Kastner, C.; Bohmert, L.; Juling, S.; Niemann, B.; Fahrenson, C.; Selve, S.; Thunemann, A. F.; Meijer, J.; Estrela-Lopis, I.; Braeuning, A.; Lampen, A., It takes more than a coating to get nanoparticles through the intestinal barrier in vitro. *Eur J Pharm Biopharm* **2017,** *118*, 21-29.
105. Zhou, X.; Dorn, M.; Vogt, J.; Spemann, D.; Yu, W.; Mao, Z.; Estrela-Lopis, I.; Donath, E.; Gao, C., A quantitative study of the intracellular concentration of graphene/noble metal nanoparticle composites and their cytotoxicity. *Nanoscale* **2014,** *6* (15), 8535-42.
106. Collins, A. R.; Annangi, B.; Rubio, L.; Marcos, R.; Dorn, M.; Merker, C.; Estrela-Lopis, I.; Cimpan, M. R.; Ibrahim, M.; Cimpan, E.; Ostermann, M.; Sauter, A.; Yamani, N. E.; Shaposhnikov, S.; Chevillard, S.; Paget, V.; Grall, R.; Delic, J.; de-Cerio, F. G.; Suarez-Merino, B.; Fessard, V.; Hogeveen, K. N.; Fjellsbo, L. M.; Pran, E. R.; Brzicova, T.; Topinka, J.; Silva, M. J.; Leite, P. E.; Ribeiro, A. R.; Granjeiro, J. M.; Grafstrom, R.; Prina-Mello, A.; Dusinska, M., High throughput toxicity screening and intracellular detection of nanomaterials. *Wiley Interdiscip Rev Nanomed Nanobiotechnol* **2017,** *9* (1), e1413.

107. Reinert, T.; Andrea, T.; Barapatre, N.; Hohlweg, M.; Koal, T.; Larisch, W.; Reinert, A.; Spemann, D.; Vogt, J.; Werner, R., Biomedical research at LIPSION–Present state and future developments. *Nucl Instrum Methods Phys Res, Sect B* **2011,** *269* (20), 2254-2259.
108. Borm, P. J.; Kreyling, W., Toxicological hazards of inhaled nanoparticles--potential implications for drug delivery. *J Nanosci Nanotechnol* **2004,** *4* (5), 521-31.
109. Krug, H. F., Nanosicherheitsforschung - sind wir auf dem richtigen Weg? *Angew Chem* **2014,** *126* (46), 12502-12518.
110. Oberdörster, G., Safety assessment for nanotechnology and nanomedicine: concepts of nanotoxicology. *J Intern Med* **2010,** *267* (1), 89-105.
111. Powers, K. W.; Brown, S. C.; Krishna, V. B.; Wasdo, S. C.; Moudgil, B. M.; Roberts, S. M., Research strategies for safety evaluation of nanomaterials. Part VI. Characterization of nanoscale particles for toxicological evaluation. *Toxicological Sciences* **2006,** *90* (2), 296-303.
112. Elsaesser, A.; Howard, C. V., Toxicology of nanoparticles. *Adv Drug Delivery Rev* **2012,** *64* (2), 129-137.
113. Nemmar, A.; Holme, J. A.; Rosas, I.; Schwarze, P. E.; Alfaro-Moreno, E., Recent advances in particulate matter and nanoparticle toxicology: a review of the in vivo and in vitro studies. *BioMed research international* **2013,** *2013*.
114. De Jong, W. H.; Hagens, W. I.; Krystek, P.; Burger, M. C.; Sips, A. J.; Geertsma, R. E., Particle size-dependent organ distribution of gold nanoparticles after intravenous administration. *Biomaterials* **2008,** *29* (12), 1912-1919.
115. Cho, E. J.; Holback, H.; Liu, K. C.; Abouelmagd, S. A.; Park, J.; Yeo, Y., Nanoparticle characterization: state of the art, challenges, and emerging technologies. *Mol Pharmaceutics* **2013,** *10* (6), 2093-2110.
116. Vance, M. E.; Kuiken, T.; Vejerano, E. P.; McGinnis, S. P.; Hochella Jr, M. F.; Rejeski, D.; Hull, M. S., Nanotechnology in the real world: Redeveloping the nanomaterial consumer products inventory. *Beilstein J Nanotechnol* **2015,** *6*, 1769.
117. Wiechers, J. W.; Musee, N., Engineered inorganic nanoparticles and cosmetics: facts, issues, knowledge gaps and challenges. *J Biomed Nanotechnol* **2010,** *6* (5), 408-31.
118. Johnson, A. C.; Park, B., Predicting contamination by the fuel additive cerium oxide engineered nanoparticles within the United Kingdom and the associated risks. *Environ Toxicol Chem* **2012,** *31* (11), 2582-7.
119. Johnston, C. J.; Driscoll, K. E.; Finkelstein, J. N.; Baggs, R.; O'Reilly, M. A.; Carter, J.; Gelein, R.; Oberdorster, G., Pulmonary chemokine and mutagenic responses in rats after subchronic inhalation of amorphous and crystalline silica. *Toxicol Sci* **2000,** *56* (2), 405-13.
120. NanoCare-Project-Consortium, *NanoCare - Health related Apsects of Nanomaterials - Final Report*. DECHEMA e.V.: Frankfurt am Main, 2009.
121. Knorr, F.; Lademann, J.; Patzelt, A.; Sterry, W.; Blume-Peytavi, U.; Vogt, A., Follicular transport route–research progress and future perspectives. *Eur J Pharm Biopharm* **2009,** *71* (2), 173-180.
122. Vogt, A.; Combadiere, B.; Hadam, S.; Stieler, K. M.; Lademann, J.; Schaefer, H.; Autran, B.; Sterry, W.; Blume-Peytavi, U., 40 nm, but not 750 or 1,500 nm, nanoparticles enter epidermal CD1a+ cells after transcutaneous application on human skin. *J Invest Dermatol* **2006,** *126* (6), 1316-1322.
123. Rong, M.; Zhang, M.; Ruan, W., Surface modification of nanoscale fillers for improving properties of polymer nanocomposites: a review. *Mater Sci Technol* **2006,** *22* (7), 787-796.

124. Xu, X.; Luo, J.; Lu, X.; Zhang, C.; Guo, D., Effect of nanoparticle impact on material removal. *Tribol Trans* **2008,** *51* (6), 718-722.
125. International Agency for Research on Cancer, IARC Monograph on the Evaluation of carcinogenic risks to humans, No. 68: Silica. *IARC Monogr Eval Carcinog Risks Hum* **1997,** *68*, 41-242.
126. Van Hoecke, K.; Quik, J. T.; Mankiewicz-Boczek, J.; De Schamphelaere, K. A.; Elsaesser, A.; Van der Meeren, P.; Barnes, C.; McKerr, G.; Howard, C. V.; Van de Meent, D.; Rydzynski, K.; Dawson, K. A.; Salvati, A.; Lesniak, A.; Lynch, I.; Silversmit, G.; De Samber, B.; Vincze, L.; Janssen, C. R., Fate and effects of CeO2 nanoparticles in aquatic ecotoxicity tests. *Environ Sci Technol* **2009,** *43* (12), 4537-46.
127. Hoshino, T.; Kurata, Y.; Terasaki, Y.; Susa, K., Mechanism of polishing of SiO 2 films by CeO 2 particles. *J Non-Cryst Solids* **2001,** *283* (1), 129-136.
128. Gutsch, A.; Averdung, J.; Mühlenweg, H., Von der technischen Entwicklung zum erfolgreichen nanotechnologischen Produkt. *Chem Ing Tech* **2005,** *77* (9), 1377-1392.
129. Lahive, E.; Jurkschat, K.; Shaw, B. J.; Handy, R. D.; Spurgeon, D. J.; Svendsen, C., Toxicity of cerium oxide nanoparticles to the earthworm Eisenia fetida: subtle effects. *Environ Chem* **2014,** *11* (3), 268.
130. Arnold, M. C.; Badireddy, A. R.; Wiesner, M. R.; Di Giulio, R. T.; Meyer, J. N., Cerium oxide nanoparticles are more toxic than equimolar bulk cerium oxide in Caenorhabditis elegans. *Arch Environ Contam Toxicol* **2013,** *65* (2), 224-33.
131. Lin, S.; Wang, X.; Ji, Z.; Chang, C. H.; Dong, Y.; Meng, H.; Liao, Y. P.; Wang, M.; Song, T. B.; Kohan, S.; Xia, T.; Zink, J. I.; Lin, S.; Nel, A. E., Aspect ratio plays a role in the hazard potential of CeO2 nanoparticles in mouse lung and zebrafish gastrointestinal tract. *ACS Nano* **2014,** *8* (5), 4450-64.
132. Chevalier, J.; Gremillard, L., Ceramics for medical applications: A picture for the next 20 years. *J Eur Ceram Soc* **2009,** *29* (7), 1245-1255.
133. Kaya, C.; He, J.; Gu, X.; Butler, E., Nanostructured ceramic powders by hydrothermal synthesis and their applications. *Microporous Mesoporous Mater* **2002,** *54* (1), 37-49.
134. Mitra, S. B.; Wu, D.; Holmes, B. N., An application of nanotechnology in advanced dental materials. *J Am Dent Assoc* **2003,** *134* (10), 1382-90.
135. Maskell, W. C., Progress in the development of zirconia gas sensors. *Solid State Ionics* **2000,** *134* (1), 43-50.
136. Zhang, Y.; Gao, J.; Peng, D.; Guangyao, M.; Liu, X., Dip-coating thin yttria-stabilized zirconia films for solid oxide fuel cell applications. *Ceram Int* **2004,** *30* (6), 1049-1053.
137. Hadjimichael, O. C.; Brubaker, R. E., Evaluation of an occupational respiratory exposure to a zirconium-containing dust. *J Occup Med* **1981,** *23* (8), 543-7.
138. Lanone, S.; Rogerieux, F.; Geys, J.; Dupont, A.; Maillot-Marechal, E.; Boczkowski, J.; Lacroix, G.; Hoet, P., Comparative toxicity of 24 manufactured nanoparticles in human alveolar epithelial and macrophage cell lines. *Part Fibre Toxicol* **2009,** *6* (1), 14.
139. U. S. National Institutes of Health-National Cancer Institute Anatomy & Physiology: Bronchi, Bronchial Tree, and Lungs. https://training.seer.cancer.gov/anatomy/respiratory/passages/bronchi.html (accessed 12.09.17).
140. Scheid, P., Atmung. In *Physiologie*, 5th ed.; Klinke, R.; Pape, H.-C.; Silbernagl, S., Eds. Georg Thieme Verlag: Stuttgart, New York, 2005; pp 255-324.
141. Lippert, H., *Lehrbuch Anatomie*. Urban & Fischer: München, 2011.

142. Benninghoff, A.; Drenkhahn, D., *Anatomie: Makoskopische Anatomie, Histologie, Embryologie, Zellbiologie. Band 1.* Urban und Fischer Verlag: München, Jena, 2003; Vol. Band 1.
143. Kim, Y. S.; Kim, J. S.; Cho, H. S.; Rha, D. S.; Kim, J. M.; Park, J. D.; Choi, B. S.; Lim, R.; Chang, H. K.; Chung, Y. H.; Kwon, I. H.; Jeong, J.; Han, B. S.; Yu, I. J., Twenty-eight-day oral toxicity, genotoxicity, and gender-related tissue distribution of silver nanoparticles in Sprague-Dawley rats. *Inhal Toxicol* **2008,** *20* (6), 575-83.
144. Fabian, E.; Landsiedel, R.; Ma-Hock, L.; Wiench, K.; Wohlleben, W.; van Ravenzwaay, B., Tissue distribution and toxicity of intravenously administered titanium dioxide nanoparticles in rats. *Arch Toxicol* **2008,** *82* (3), 151-7.
145. Duffin, R.; Tran, L.; Brown, D.; Stone, V.; Donaldson, K., Proinflammogenic effects of low-toxicity and metal nanoparticles in vivo and in vitro: highlighting the role of particle surface area and surface reactivity. *Inhal Toxicol* **2007,** *19* (10), 849-56.
146. Meyer, O.; Svendsen, O., Animal Models in Pharmacology and Toxicology. In *Handbook of Laboratory Animal Science*, 2nd ed.; Hau, J.; Van Hoosier, G. L., Eds. CRC Press: Boca Raton, London, New York, Washington, D.C., 2003; Vol. 2.
147. Werner, H. W., SIMS: from research to production control. *Surf Interface Anal* **2003,** *35* (11), 859-879.
148. Boxer, S. G.; Kraft, M. L.; Weber, P. K., Advances in imaging secondary ion mass spectrometry for biological samples. *Annu Rev Biophys* **2009,** *38*, 53-74.
149. Williams, P., Secondary Ion Mass Spectrometry. *Ann Rev Mater Sci* **1985,** *15*, 517-548.
150. Steffens, P.; Niehuis, E.; Friese, T.; Benninghoven, A., Secondary Ion Formation from Organic Solids. *Ion Form Org Solids: Proc Int Conf, 2nd* **1983,** *25*.
151. Hagenhoff, B., High Resolution Surface Analysis by TOF-SIMS. *Mikrochim Acta* **2000,** *132*, 259-271.
152. Lozano-Perez, S.; Kilburn, M.; Yamada, T.; Terachi, T.; English, C.; Grovenor, C., High-resolution imaging of complex crack chemistry in reactor steels by NanoSIMS. *J Nucl Mater* **2008,** *374* (1-2), 61-68.
153. Behrens, S.; Losekann, T.; Pett-Ridge, J.; Weber, P. K.; Ng, W. O.; Stevenson, B. S.; Hutcheon, I. D.; Relman, D. A.; Spormann, A. M., Linking microbial phylogeny to metabolic activity at the single-cell level by using enhanced element labeling-catalyzed reporter deposition fluorescence in situ hybridization (EL-FISH) and NanoSIMS. *Appl Environ Microbiol* **2008,** *74* (10), 3143-50.
154. Hauri, E. H.; Papineau, D.; Wang, J.; Hillion, F., High-precision analysis of multiple sulfur isotopes using NanoSIMS. *Chem Geol* **2016,** *420*, 148-161.
155. Zhang, J.; Lin, Y.; Yang, W.; Shen, W.; Hao, J.; Hu, S.; Cao, M., Improved precision and spatial resolution of sulfur isotope analysis using NanoSIMS. *J Anal At Spectrom* **2014,** *29* (10), 1934-1943.
156. Lechene, C.; Hillion, F.; McMahon, G., High-resolution quantitative imaging of mammalian and bacterial cells using stable isotope mass spectrometry. *Journal of Biology* **2006,** *5* (20).
157. Tian, H.; Wucher, A.; Winograd, N., Dynamic Reactive Ionization with Cluster Secondary Ion Mass Spectrometry. *J. Am. Soc. Mass Spectrom.* **2015**, 285-292.
158. Azari, F.; Vali, H.; Guerquin-Kern, J. L.; Wu, T. D.; Croisy, A.; Sears, S. K.; Tabrizian, M.; McKee, M. D., Intracellular precipitation of hydroxyapatite mineral and implications for pathologic calcification. *J Struct Biol* **2008,** *162* (3), 468-79.
159. Elbast, M.; Wu, T. D.; Guiraud-Vitaux, F.; Guerquin-Kern, J. L.; Petiet, A.; Hindie, E.; Champion, C.; Croisy, A.; Colas-Linhart, N., Kinetics of intracolloidal

iodine in thyroid of iodine-deficient or equilibrated newborn rats. Direct imaging using secondary ion mass spectrometry. *Cell Mol Biol (Noisy-le-grand)* **2007,** *53 Suppl*, OL1018-24.

160. Guerquin-Kern, J. L.; Hillion, F.; Madelmont, J. C.; Labarre, P.; Papon, J.; Croisy, A., Ultra-structural cell distribution of the melanoma marker iodobenzamide: improved potentiality of SIMS imaging in life sciences. *Biomed Eng Online* **2004,** *3*, 10.
161. Quintana, C.; Bellefqih, S.; Laval, J. Y.; Guerquin-Kern, J. L.; Wu, T. D.; Avila, J.; Ferrer, I.; Arranz, R.; Patino, C., Study of the localization of iron, ferritin, and hemosiderin in Alzheimer's disease hippocampus by analytical microscopy at the subcellular level. *J Struct Biol* **2006,** *153* (1), 42-54.
162. Quintana, C.; Wu, T. D.; Delatour, B.; Dhenain, M.; Guerquin-Kern, J. L.; Croisy, A., Morphological and chemical studies of pathological human and mice brain at the subcellular level: correlation between light, electron, and nanosims microscopies. *Microsc Res Tech* **2007,** *70* (4), 281-95.
163. Orphan, V. J.; House, C. H.; Hinrichs, K.-U.; McKeegan, K. D.; DeLong, E. F., Methane-consuming Archaea revealed by directly coupled isotopic and phylogenetic analyses. *Science* **2001,** *293*, 484-87.
164. Audinot, J. N.; Guignard, C.; Migeon, H. N.; Hoffmann, L., Study of the mechanism of diatom cell division by means of 29Si isotope tracing. *Appl Surf Sci* **2006,** *252* (19), 6813-6815.
165. Li, T.; Wu, T. D.; Mazeas, L.; Toffin, L.; Guerquin-Kern, J. L.; Leblon, G.; Bouchez, T., Simultaneous analysis of microbial identity and function using NanoSIMS. *Environ Microbiol* **2008,** *10* (3), 580-8.
166. Musat, N.; Halm, H.; Winterholler, B.; Hoppe, P.; Peduzzi, S.; Hillion, F.; Horreard, F.; Amann, R.; Jorgensen, B. B.; Kuypers, M. M., A single-cell view on the ecophysiology of anaerobic phototrophic bacteria. *Proc Natl Acad Sci U S A* **2008,** *105* (46), 17861-6.
167. Peteranderl, R.; Lechene, C., Measure of carbon and nitrogen stable isotope ratios in cultured cells. *J Am Soc Mass Spectrom* **2004,** *15* (4), 478-85.
168. Steinhauser, M. L.; Lechene, C. P., Quantitative imaging of subcellular metabolism with stable isotopes and multi-isotope imaging mass spectrometry. *Semin Cell Dev Biol* **2013,** *24* (8-9), 661-7.
169. Kraft, M. L.; Fishel, S. F.; Marxer, C. G.; Weber, P. K.; Hutcheon, I. D.; Boxer, S. G., Quantitative analysis of supported membrane composition using the NanoSIMS. *Appl Surf Sci* **2006,** *252* (19), 6950-56.
170. Kraft, M. L.; Weber, P. K.; Longo, M. L.; Hutcheon, I. D.; Boxer, S. G., Phase separation of lipid membranes analyzed with high-resolution secondary ion mass spectrometry. *Science* **2006,** *313* (5795), 1948-51.
171. Guerquin-Kern, J. L.; Wu, T. D.; Quintana, C.; Croisy, A., Progress in analytical imaging of the cell by dynamic secondary ion mass spectrometry (SIMS microscopy). *Biochim Biophys Acta* **2005,** *1724* (3), 228-38.
172. Wilson, R. L.; Frisz, J. F.; Hanafin, W. P.; Carpenter, K. J.; Hutcheon, I. D.; Weber, P. K.; Kraft, M. L., Fluorinated colloidal gold immunolabels for imaging select proteins in parallel with lipids using high-resolution secondary ion mass spectrometry. *Bioconjug Chem* **2012,** *23* (3), 450-60.
173. Angelo, M.; Bendall, S. C.; Finck, R.; Hale, M. B.; Hitzman, C.; Borowsky, A. D.; Levenson, R. M.; Lowe, J. B.; Liu, S. D.; Zhao, S.; Natkunam, Y.; Nolan, G. P., Multiplexed ion beam imaging of human breast tumors. *Nat Med* **2014,** *20* (4), 436-42.

174. Gnaser, H.; Fujii, M.; Nakagawa, S.; Seki, T.; Aoki, T.; Matsuo, J., Peptide dissociation patterns in secondary ion mass spectrometry under large argon cluster ion bombardment. *Rapid Commun Mass Spectrom* **2013,** *27* (13), 1490-6.
175. McArthur, S. L.; Vendettuoli, M. C.; Ratner, B. D.; Castner, D. G., Methods for generating protein molecular ions in ToF-SIMS. *Langmuir* **2004,** *20* (9), 3704-9.
176. Mochiji, K.; Hashinokuchi, M.; Moritani, K.; Toyoda, N., Matrix-free detection of intact ions from proteins in argon-cluster secondary ion mass spectrometry. *Rapid Commun Mass Spectrom* **2009,** *23* (5), 648-52.
177. Touboul, D.; Roy, S.; Germain, D. P.; Chaminade, P.; Brunelle, A.; Laprevote, O., MALDI-TOF and cluster-TOF-SIMS imaging of Fabry disease biomarkers. *Int J Mass Spectrom* **2007,** *260* (2-3), 158-165.
178. Roddy, T. P.; Cannon, D. M.; Meserole, C. A.; Winograd, N.; Ewing, A. G., Imaging of Freeze-Fractured Cells with in Sito Fluorescenc and Time-of-Flight Secondary Ion Mass Spectrometry. *Anal Chem* **2002,** *74*, 4011-4019.
179. Roddy, T. P.; Cannon, D. M.; Ostrowski, S.; Winograd, N.; Ewing, A. G., Identification of Cellular Sections with Imaging Mass Spectrometry Following Freeeze Fracture. *Anal Chem* **2002,** *74* (4020-4026).
180. Parry, S.; Winograd, N., High-resolution TOF-SIMS imaging of eukaryotic cells preserved in a trehalose matrix. *Anal Chem* **2005,** *77* (24), 7950-7.
181. Altelaar, A. F.; Klinkert, I.; Jalink, K.; de Lange, R. P.; Adan, R. A.; Heeren, R. M.; Piersma, S. R., Gold-enhanced biomolecular surface imaging of cells and tissue by SIMS and MALDI mass spectrometry. *Anal Chem* **2006,** *78* (3), 734-42.
182. Pacholski, M. L.; Cannon, D. M.; Ewing, A. G.; Winograd, N., Imaging of Exposed Headgroups and Tailgroups of Phospholipid Membranes by Mass Spectrometry. *J Am Chem Soc* **1999,** *121*, 4716-4717.
183. McQuaw, C. M.; Zheng, L.; Ewing, A. G.; Winograd, N., Localization of sphingomyelin in cholesterol domains by imaging mass spectrometry. *Langmuir* **2007,** *23* (10), 5645-50.
184. Sostarecz, A. G.; McQuaw, C. M.; Wucher, A.; Winograd, N., Depth profiling of Langmuir-Blodgett films with a buckminsterfullerene probe. *Anal Chem* **2004,** *76* (22), 6651-8.
185. Harbottle, R. R.; Nag, K.; McIntyre, N. S.; Possmayer, F.; Petersen, N. O., Molecular Organization Revealed by Time-of-Flight Secondary Ion Mass Spetrometry of a Clinically Used Extracted Pulmonary Surfactant. *Langmuir* **2003,** *19*, 3698-3704.
186. Breitenstein, D.; Batenburg, J. J.; Hagenhoff, B.; Galla, H. J., Lipid specificity of surfactant protein B studied by time-of-flight secondary ion mass spectrometry. *Biophys J* **2006,** *91* (4), 1347-56.
187. Colliver, T. L.; Brummel, C. L.; Pacholski, M. L.; Swanek, F. D.; Ewing, A. G.; Winograd, N., Atomic and Molecular Imaging at the Single-Cell Level with TOF-SIMS. *Anal Chem* **1997,** *69*, 2225-2231.
188. Nygren, H.; Hagenhoff, B.; Malmberg, P.; Nilsson, M.; Richter, K., Bioimaging TOF-SIMS: High resolution 3D imaging of single cells. *Microsc Res Tech* **2007,** *70* (11), 969-74.
189. Zhen, L.; McQuaw, C. M.; Ewing, A. G.; Winograd, N., Sphingomyelin/Phosphatidylcholine and Cholesterol Interactions Studied by Imaging Mass Spectrometry. *J Am Chem Soc* **2007,** *129*, 15730-31.
190. Bourdos, N.; Kollmer, F.; Benninghoven, A.; Ross, M.; Sieber, M.; Galla, H. J., Analysis of lung surfactant model systems with time-of-flight secondary ion mass spectrometry. *Biophys J* **2000,** *79* (1), 357-69.

191. Ostrowski, S. G.; Van Bell, C. T.; Winograd, N.; Ewing, A. G., Mass spectrometric imaging of highly curved membranes during Tetrahymena mating. *Science* **2004,** *305* (5680), 71-3.

192. Ingram, J. C.; Bauer, W. F.; Lehman, R. M.; O'Connell, S. P.; Shaw, A. D., Detection of fatty acids from intact microorganisms by molecular beam static secondary ion mass spectrometry. *J Microbiol Methods* **2003,** *53* (3), 295-307.

193. Jungnickel, H.; Jones, E. A.; Lockyer, N. P.; Oliver, S. G.; Stephens, G. M.; Vickerman, J. C., Application of TOF-SIMS with chemometrics to discriminate between four different yeast strains from the species Candida glabrata and Saccharomyces cerevisiae. *Anal Chem* **2005,** *77* (6), 1740-5.

194. Wehrli, P. M.; Lindberg, E.; Angerer, T. B.; Wold, A. E.; Gottfries, J.; Fletcher, J. S., Maximising the potential for bacterial phenotyping using time-of-flight secondary ion mass spectrometry with multivariate analysis and Tandem Mass Spectrometry. *Surf Interface Anal* **2014,** *46* (S1), 173-176.

195. Nygren, H.; Borner, K.; Hagenhoff, B.; Malmberg, P.; Mansson, J. E., Localization of cholesterol, phosphocholine and galactosylceramide in rat cerebellar cortex with imaging TOF-SIMS equipped with a bismuth cluster ion source. *Biochim Biophys Acta* **2005,** *1737* (2-3), 102-10.

196. Sjovall, P.; Lausmaa, J.; Johansson, B., Mass spectrometric imaging of lipids in brain tissue. *Anal Chem* **2004,** *76* (15), 4271-8.

197. Touboul, D.; Halgand, F.; Brunelle, A.; Kersting, R.; Tallarek, E.; Hagenhoff, B.; Laprevote, O., Tissue molecular ion imaging by gold cluster ion bombardment. *Anal Chem* **2004,** *76* (6), 1550-9.

198. Sjövall, P.; Johansson, B.; Lausmaa, J., Localization of lipids in freeze-dried mouse brain sections by imaging TOF-SIMS. *Appl Surf Sci* **2006,** *252* (19), 6966-6974.

199. Denbigh, J. L.; Lockyer, N. P., ToF-SIMS as a tool for profiling lipids in cancer and other diseases. *Mater Sci Technol* **2014,** *31* (2), 137-147.

200. Fornai, L.; Angelini, A.; Klinkert, I.; Giskes, F.; Kiss, A.; Eijkel, G.; Amstalden-van Hove, E. A.; Klerk, L. A.; Fedrigo, M.; Pieraccini, G.; Moneti, G.; Valente, M.; Thiene, G.; Heeren, R. M., Three-dimensional molecular reconstruction of rat heart with mass spectrometry imaging. *Anal Bioanal Chem* **2012,** *404* (10), 2927-38.

201. Szakal, C.; Narayan, K.; Fu, J.; Lefman, J.; Subramaniam, S., Compositional mapping of the surface and interior of mammalian cells at submicrometer resolution. *Anal Chem* **2011,** *83* (4), 1207-13.

202. Breitenstein, D.; Rommel, C. E.; Mollers, R.; Wegener, J.; Hagenhoff, B., The chemical composition of animal cells and their intracellular compartments reconstructed from 3D mass spectrometry. *Angew Chem Int Ed Engl* **2007,** *46* (28), 5332-5.

203. Fletcher, J. S.; Lockyer, N. P.; Vaidyanathan, S.; Vickerman, J. C., TOF-SIMS 3D Biomolecular Imaging of Xenopus Iaevis Oocytes Using Buckminsterfullerene (C60) Primary Ions. *Anal Chem* **2007,** *79*, 2199-2206.

204. Brison, J.; Robinson, M. A.; Benoit, D. S.; Muramoto, S.; Stayton, P. S.; Castner, D. G., TOF-SIMS 3D imaging of native and non-native species within HeLa cells. *Anal Chem* **2013,** *85* (22), 10869-77.

205. Jung, S.; Foston, M.; Kalluri, U. C.; Tuskan, G. A.; Ragauskas, A. J., 3D chemical image using TOF-SIMS revealing the biopolymer component spatial and lateral distributions in biomass. *Angew Chem Int Ed Engl* **2012,** *51* (48), 12005-8.

206. Draude, F.; Galla, S.; Pelster, A.; Tentschert, J.; Jungnickel, H.; Haase, A.; Mantion, A.; Thünemann, A. F.; Taubert, A.; Luch, A.; Arlinghaus, H. F., ToF-

SIMS and Laser-SNMS analysis of macrophages after exposure to silver nanoparticles. *Surf Interface Anal* **2013,** *45* (1), 286-289.

207. Pauksch, L.; Hartmann, S.; Rohnke, M.; Szalay, G.; Alt, V.; Schnettler, R.; Lips, K. S., Biocompatibility of silver nanoparticles and silver ions in primary human mesenchymal stem cells and osteoblasts. *Acta Biomater* **2014,** *10* (1), 439-49.
208. Angerer, T. B.; Fletcher, J. S., 3D Imaging of TiO2nanoparticle accumulation inTetrahymena pyriformis. *Surf Interface Anal* **2014,** *46* (S1), 198-203.
209. Hagenhoff, B.; Breitenstein, D.; Tallarek, E.; Möllers, R.; Niehuis, E.; Sperber, M.; Goricnik, B.; Wegener, J., Detection of micro- and nano-particles in animal cells by ToF-SIMS 3D analysis. *Surf Interface Anal* **2013,** *45* (1), 315-319.
210. Lee, P. L.; Chen, B. C.; Gollavelli, G.; Shen, S. Y.; Yin, Y. S.; Lei, S. L.; Jhang, C. L.; Lee, W. R.; Ling, Y. C., Development and validation of TOF-SIMS and CLSM imaging method for cytotoxicity study of ZnO nanoparticles in HaCaT cells. *J Hazard Mater* **2014,** *277*, 3-12.
211. Arts, J. H. E.; Muijser, H.; Duistermaat, E.; Junker, K.; Kuper, C. F., Five-day inhalation toxicity study of three types of synthetic amorphous silicas in Wistar rats and post-exposure evaluations for up to 3months. *Food Chem Toxicol* **2007,** *45* (10), 1856-1867.
212. Wiemann, M.; Sauer, U.; Vennemann, A.; Backer, S.; Keller, J.-G.; Ma-Hock, L.; Wohlleben, W.; Landsiedel, R., In Vitro and In Vivo Short-Term Pulmonary Toxicity of Differently Sized Colloidal Amorphous SiO2. *Nanomaterials* **2018,** *8* (3), 160.
213. Landsiedel, R.; Ma-Hock, L.; Hofmann, T.; Wiemann, M.; Strauss, V.; Treumann, S.; Wohlleben, W.; Groters, S.; Wiench, K.; van Ravenzwaay, B., Application of short-term inhalation studies to assess the inhalation toxicity of nanomaterials. *Part Fibre Toxicol* **2014,** *11*, 16.
214. Marzaioli, V.; Aguilar-Pimentel, J. A.; Weichenmeier, I.; Luxenhofer, G.; Wiemann, M.; Landsiedel, R.; Wohlleben, W.; Eiden, S.; Mempel, M.; Behrendt, H.; Schmidt-Weber, C.; Gutermuth, J.; Alessandrini, F., Surface modifications of silica nanoparticles are crucial for their inert versus proinflammatory and immunomodulatory properties. *Int J Nanomed* **2014,** *9*, 2815-32.
215. Lopez-Rodriguez, E.; Gay-Jordi, G.; Mucci, A.; Lachmann, N.; Serrano-Mollar, A., Lung surfactant metabolism: early in life, early in disease and target in cell therapy. *Cell Tissue Res* **2017,** *367* (3), 721-735.
216. Wright, J. R., Immunoregulatory functions of surfactant proteins. *Nat Rev Immunol* **2005,** *5*, 58-68.
217. Monopoli, M. P.; Walczyk, D.; Campbell, A.; Elia, G.; Lynch, I.; Baldelli Bombelli, F.; Dawson, K. A., Physical−Chemical Aspects of Protein Corona: Relevance to in Vitro and in Vivo Biological Impacts of Nanoparticles. *J Am Chem Soc* **2011,** *133* (8), 2525-2534.
218. Wohlleben, W.; Driessen, M. D.; Raesch, S.; Schaefer, U. F.; Schulze, C.; Vacano, B. v.; Vennemann, A.; Wiemann, M.; Ruge, C. A.; Platsch, H., Influence of agglomeration and specific lung lining lipid/protein interaction on short-term inhalation toxicity. *Nanotoxicology* **2016,** *10* (7), 970-980.
219. Kapralov, A. A.; Feng, W. H.; Amoscato, A. A.; Yanamala, N.; Balasubramanian, K.; Winnica, D. E.; Kisin, E. R.; Kotchey, G. P.; Gou, P.; Sparvero, L. J.; Ray, P.; Mallampalli, R. K.; Klein-Seetharaman, J.; Fadeel, B.; Star, A.; Shvedova, A. A.; Kagan, V. E., Adsorption of Surfactant Lipids by Single-Walled Carbon Nanotubes in Mouse Lung upon Pharyngeal Aspiration. *ACS Nano* **2012,** *6* (5), 4147-4156.

220. Veith, L.; Vennemann, A.; Breitenstein, D.; Engelhard, C.; Wiemann, M.; Hagenhoff, B., Detection of SiO2 nanoparticles in lung tissue by ToF-SIMS imaging and fluorescence microscopy. *Analyst* **2017,** *142* (14), 2631-2639.
221. Rehn, B.; Bruch, J.; Zou, T.; Hobusch, G., Recovery of rat alveolar macrophages by bronchoalveolar lavage under normal and activated conditions. *Environ Health Perspect* **1992,** *97*, 11-16.
222. Forster, B.; Van De Ville, D.; Berent, J.; Sage, D.; Unser, M., Complex wavelets for extended depth-of-field: A new method for the fusion of multichannel microscopy images. *Microsc Res Tech* **2004,** *65* (1-2), 33-42.
223. Schneider, C. A.; Rasband, W. S.; Eliceiri, K. W., NIH Image to ImageJ: 25 years of image analysis. *Nat Methods* **2012,** *9* (7), 671-5.
224. Schindelin, J.; Arganda-Carreras, I.; Frise, E.; Kaynig, V.; Longair, M.; Pietzsch, T.; Preibisch, S.; Rueden, C.; Saalfeld, S.; Schmid, B.; Tinevez, J. Y.; White, D. J.; Hartenstein, V.; Eliceiri, K.; Tomancak, P.; Cardona, A., Fiji: an open-source platform for biological-image analysis. *Nat Methods* **2012,** *9* (7), 676-82.
225. Adler, J.; Parmryd, I., Quantifying colocalization by correlation: the Pearson correlation coefficient is superior to the Mander's overlap coefficient. *Cytometry A* **2010,** *77* (8), 733-42.
226. Thevenaz, P.; Ruttimann, U. E.; Unser, M., A pyramid approach to subpixel registration based on intensity. *IEEE Trans Image Process* **1998,** *7* (1), 27-41.
227. Jasieniak, M.; Graham, D.; Kingshott, P.; Gamble, L. J.; Griesser, H. J., Surface Analysis of Biomaterials. In *Handbook of Surface and Interface Analysis: Methods for Problem-Solving*, 2nd ed.; Riviere, J. C.; Myhra, S., Eds. CRC Press: Boca Raton, London, New York, 2009; pp 536-538.
228. Sandoval, L.; Urbassek, H. M., Collision-spike Sputtering of Au Nanoparticles. *Nanoscale Res Lett* **2015,** *10* (1), 1009.
229. Yang, L.; Seah, M. P.; Anstis, E. H.; Gilmore, I. S.; Lee, J. L. S., Sputtering yields of Gold Nanoparticles by C60 Ions. *J Phys Chem C* **2012,** *116*, 9311-9318.
230. Alivisatos, A. P., Semiconductor Clusters, Nanocrystals, and Quantum Dots. *Science* **1996,** *271* (5251), 933-937.
231. Shon, H. K.; Park, J.; Choi, I.; Park, H. M.; Moon, D. W.; Lee, T. G., Mass imaging of iron oxide nanoparticles inside cells for in vitro cytotoxicity. *J Nanosci Nanotechnol* **2011,** *11* (1), 638-41.
232. Mercer, R. R.; Scabilloni, J. F.; Wang, L.; Battelli, L. A.; Antonini, J. M.; Roberts, J. R.; Qian, Y.; Sisler, J. D.; Castranova, V.; Porter, D. W.; Hubbs, A. F., The Fate of Inhaled Nanoparticles: Detection and Measurement by Enhanced Dark-field Microscopy. *Toxicol Pathol* **2018,** *46* (1), 28-46.
233. Creutzenberg, O.; Bellmann, B.; Korolewitz, R.; Koch, W.; Mangelsdorf, I.; Tillmann, T.; Schaudien, D., Change in agglomeration status and toxicokinetic fate of various nanoparticles in vivo following lung exposure in rats. *Inhal Toxicol* **2012,** *24* (12), 821-30.
234. Gosens, I.; Post, J. A.; de la Fonteyne, L. J.; Jansen, E. H.; Geus, J. W.; Cassee, F. R.; de Jong, W. H., Impact of agglomeration state of nano- and submicron sized gold particles on pulmonary inflammation. *Part Fibre Toxicol* **2010,** *7* (1), 37.
235. Passarelli, M. K.; Pirkl, A.; Moellers, R.; Grinfeld, D.; Kollmer, F.; Havelund, R.; Newman, C. F.; Marshall, P. S.; Arlinghaus, H.; Alexander, M. R.; West, A.; Horning, S.; Niehuis, E.; Makarov, A.; Dollery, C. T.; Gilmore, I. S., The 3D OrbiSIMS—label-free metabolic imaging with subcellular lateral resolution and high mass-resolving power. *Nature Methods* **2017,** *14*, 1175.
236. Selvan, V. A. M.; Anand, R. B.; Udayakumar, M., Effects of Cerium Oxide Nanoparticle Addition in Diesel and Diesel-Biodiesel-Ethanol Blends on the

Performance and Emission Characteristics of a CI engine. *ARPN J. Eng. Appl. Sci.* **2009,** *4* (7), 1-6.

237. Fairley, P. Cleaning Up Combustion? https://www.technologyreview.com/s/406345/cleaning-up-combustion/ (accessed 16.01.17).
238. Oberdörster, G.; Sharp, Z.; Atudorei, V.; Elder, A.; Gelein, R.; Kreyling, W.; Cox, C., Translocation of inhaled ultrafine particles to the brain. *Inhal Toxicol* **2004,** *16* (6-7), 437-45.
239. Kwon, J. T.; Hwang, S. K.; Jin, H.; Kim, D. S.; Minai-Tehrani, A.; Yoon, H. J.; Choi, M.; Yoon, T. J.; Han, D. Y.; Kang, Y. W.; Yoon, B. I.; Lee, J. K.; Cho, M. H., Body distribution of inhaled fluorescent magnetic nanoparticles in the mice. *J Occup Health* **2008,** *50* (1), 1-6.
240. Silge, A.; Bräutigam, K.; Bocklitz, T.; Rosch, P.; Vennemann, A.; Schmitz, I.; Popp, J.; Wiemann, M., ZrO_2 nanoparticles labeled via a native protein corona: detection by fluorescence microscopy and Raman microspectroscopy in rat lungs. *Analyst* **2015,** *140* (15), 5120-8.
241. Matthaus, C.; Chernenko, T.; Newmark, J. A.; Warner, C. M.; Diem, M., Label-free detection of mitochondrial distribution in cells by nonresonant Raman microspectroscopy. *Biophys J* **2007,** *93* (2), 668-73.
242. Yang, J.; Gilmore, I., Application of secondary ion mass spectrometry to biomaterials, proteins and cells: a concise review. *Mater Sci Tech Ser* **2014,** *31* (2), 131-136.
243. Gulin, A.; Nadtochenko, V.; Astafiev, A.; Pogorelova, V.; Rtimi, S.; Pogorelov, A., Correlating microscopy techniques and ToF-SIMS analysis of fully grown mammalian oocytes. *Analyst* **2016,** *141* (13), 4121-9.
244. Larue, C.; Castillo-Michel, H.; Sobanska, S.; Cecillon, L.; Bureau, S.; Barthes, V.; Ouerdane, L.; Carriere, M.; Sarret, G., Foliar exposure of the crop Lactuca sativa to silver nanoparticles: evidence for internalization and changes in Ag speciation. *J Hazard Mater* **2014,** *264*, 98-106.
245. Wohlleben, W.; Driessen, M. D.; Raesch, S.; Schaefer, U. F.; Schulze, C.; Vacano, B.; Vennemann, A.; Wiemann, M.; Ruge, C. A.; Platsch, H.; Mues, S.; Ossig, R.; Tomm, J. M.; Schnekenburger, J.; Kuhlbusch, T. A.; Luch, A.; Lehr, C. M.; Haase, A., Influence of agglomeration and specific lung lining lipid/protein interaction on short-term inhalation toxicity. *Nanotoxicology* **2016,** *10* (7), 970-80.
246. Stöber, W.; Fink, A.; Bohn, E., Controlled Growth of Monodisperse Silica Spheres in the Micron Size Range. *J Colloid Interf Sci* **1968,** *26*, 62-69.
247. Hellack, B.; Hülser, T.; Izak, E.; Kuhlbusch, T. A. J.; Meyer, F.; Spree, M.; Voetz, M.; Wiggers, H.; Wohlleben, W. Deliverable 1.3.1 Charakterisierungsbericht zu allen Materialien/Characterization report for all nanoGEM materials. http://www.nanogem.de/cms/nanogem/upload/Veroeffentlichungen/nanoGEM_Del1.3.1_Characterization_Materials_2013_04_24.pdf (accessed 06.03.2017).
248. Izak-Nau, E.; Voetz, M., As-Produced Intrinsic Physico-Chemiacl Properties and Appropriate Characterization Tools. In *Safety of Nanomaterials along their lifecycle*, Wohlleben, W.; Kuhlbusch, T. A.; Schnekenburger, J.; Lehr, C. M., Eds. Taylor & Francis Group: Boca Raton, 2015; Vol. 1, pp 3-20.
249. Malm, J.; Giannaras, D.; Riehle, M. O.; Gadegaard, N.; Sjovall, P., Fixation and drying protocols for the preparation of cell samples for time-of-flight secondary ion mass spectrometry analysis. *Anal Chem* **2009,** *81* (17), 7197-205.
250. Nygren, H.; Eriksson, C.; Malmberg, P.; Sahlin, H.; Carlsson, L.; Lausmaa, J.; Sjövall, P., A cell preparation method allowing subcellular localization of

cholesterol and phosphocholine with imaging TOF-SIMS. *Colloids Surf, B* **2003,** *30* (1-2), 87-92.

251. Collins, J. S.; Goldsmith, T. H., Spectral properties of fluorescence induced by glutaraldehyde fixation. *J Histochem Cytochem* **1981,** *29* (3), 411-4.
252. Dunn, K. W.; Kamocka, M. M.; McDonald, J. H., A practical guide to evaluating colocalization in biological microscopy. *Am J Physiol Cell Physiol* **2011,** *300* (4), C723-42.
253. Fletcher, J. S.; Vickerman, J. C., Secondary ion mass spectrometry: characterizing complex samples in two and three dimensions. *Anal Chem* **2013,** *85* (2), 610-39.
254. Tian, H.; Wucher, A.; Winograd, N., Dynamic Reactive Ionization with Cluster Secondary Ion Mass Spectrometry. *J Am Soc Mass Spectrom* **2016,** *27* (2), 285-92.
255. Tian, H.; Maciazek, D.; Postawa, Z.; Garrison, B. J.; Winograd, N., CO2 Cluster Ion Beam, an Alternative Projectile for Secondary Ion Mass Spectrometry. *J Am Soc Mass Spectrom* **2016,** *27* (9), 1476-82.
256. Sheraz nee Rabbani, S.; Barber, A.; Fletcher, J. S.; Lockyer, N. P.; Vickerman, J. C., Enhancing secondary ion yields in time of flight-secondary ion mass spectrometry using water cluster primary beams. *Anal Chem* **2013,** *85* (12), 5654-8.
257. 3D Nanosims—Label-Free Molecular Imaging. http://www.npl.co.uk/news/3d-nanosimslabel-free-molecular-imaging (accessed 25.08.2016).
258. Piehowski, P. D.; Carado, A. J.; Kurczy, M. E.; Ostrowski, S. G.; Heien, M. L.; Winograd, N.; Ewing, A. G., MS/MS methodology to improve subcellular mapping of cholesterol using TOF-SIMS. *Anal Chem* **2008,** *80* (22), 8662-7.
259. Fisher, G. L.; Bruinen, A. L.; Ogrinc Potocnik, N.; Hammond, J. S.; Bryan, S. R.; Larson, P. E.; Heeren, R. M., A New Method and Mass Spectrometer Design for TOF-SIMS Parallel Imaging MS/MS. *Anal Chem* **2016,** *88* (12), 6433-40.
260. Wildanger, D.; Patton, B. R.; Schill, H.; Marseglia, L.; Hadden, J. P.; Knauer, S.; Schonle, A.; Rarity, J. G.; O'Brien, J. L.; Hell, S. W.; Smith, J. M., Solid immersion facilitates fluorescence microscopy with nanometer resolution and sub-angstrom emitter localization. *Adv Mater* **2012,** *24* (44), OP309-13.
261. Peralta-Videa, J. R.; Zhao, L.; Lopez-Moreno, M. L.; de la Rosa, G.; Hong, J.; Gardea-Torresdey, J. L., Nanomaterials and the environment: a review for the biennium 2008-2010. *J Hazard Mater* **2011,** *186* (1), 1-15.
262. Sun, T. Y.; Gottschalk, F.; Hungerbühler, K.; Nowack, B., Comprehensive probabilistic modelling of environmental emissions of engineered nanomaterials. *Environ pollut* **2014,** *185*, 69-76.
263. *nano.DE-Report 2013*; Federal Ministry of Education and Reserach (BMBF) Bonn, 2013.
264. Kuhlbusch, T. A.; Asbach, C.; Fissan, H.; Göhler, D.; Stintz, M., Nanoparticle exposure at nanotechnology workplaces: a review. *Part Fibre Toxicol* **2011,** *8* (1), 22.
265. Project on Emerging Nanotechnologies (2013). Consumer Products Inventory. http://www.nanotechproject.org/inventories/ (accessed 11.08.2017).
266. Detailed information on nanomaterials from A to Z | Knowledge Base Nanomaterials. http://nanopartikel.info/en/nanoinfo/materials (accessed 11.08.2017).
267. Cotogno, G.; Totaro, S.; Rasmussen, K.; Pianella, F.; Roncaglia, M.; Olsson, H.; Sintes, J. R.; Crutzen, H. *Cerium Dioxide, NM-211, NM-212, NM-213. Characterization and test item preparation*; Publications Office of the European Union: Luxembourg, 2014.

268. Cordelli, E.; Keller, J.; Eleuteri, P.; Villani, P.; Ma-Hock, L.; Schulz, M.; Landsiedel, R.; Pacchierotti, F., No genotoxicity in rat blood cells upon 3- or 6-month inhalation exposure to CeO2 or BaSO4 nanomaterials. *Mutagenesis* **2017,** *32* (1), 13-22.
269. Pozebon, D.; Scheffler, G. L.; Dressler, V. L.; Nunes, M. A. G., Review of the applications of laser ablation inductively coupled plasma mass spectrometry (LA-ICP-MS) to the analysis of biological samples. *J. Anal. At. Spectrom.* **2014,** *29* (12), 2204-2228.
270. Sadrieh, N.; Wokovich, A. M.; Gopee, N. V.; Zheng, J.; Haines, D.; Parmiter, D.; Siitonen, P. H.; Cozart, C. R.; Patri, A. K.; McNeil, S. E.; Howard, P. C.; Doub, W. H.; Buhse, L. F., Lack of significant dermal penetration of titanium dioxide from sunscreen formulations containing nano- and submicron-size TiO2 particles. *Toxicol Sci* **2010,** *115* (1), 156-66.
271. Vavpetič, P.; Pelicon, P.; Vogel-Mikuš, K.; Grlj, N.; Pongrac, P.; Jeromel, L.; Ogrinc, N.; Regvar, M., Micro-PIXE on thin plant tissue samples in frozen hydrated state: A novel addition to JSI nuclear microprobe. *Nucl Instrum Methods Phys Res, Sect B* **2013,** *306*, 140-143.
272. Vavpetič, P.; Vogel-Mikuš, K.; Jeromel, L.; Ogrinc Potočnik, N.; Pongrac, P.; Drobne, D.; Pipan Tkalec, Ž.; Novak, S.; Kos, M.; Koren, Š.; Regvar, M.; Pelicon, P., Elemental distribution and sample integrity comparison of freeze-dried and frozen-hydrated biological tissue samples with nuclear microprobe. *Nucl Instrum Methods Phys Res, Sect B* **2015,** *348*, 147-151.
273. Angel, B. M.; Vallotton, P.; Apte, S. C., On the mechanism of nanoparticulate CeO2 toxicity to freshwater algae. *Aquat Toxicol* **2015,** *168*, 90-7.
274. Roth, G. A.; Tahiliani, S.; Neu-Baker, N. M.; Brenner, S. A., Hyperspectral microscopy as an analytical tool for nanomaterials. *Wiley Interdiscip Rev Nanomed Nanobiotechnol* **2015,** *7* (4), 565-79.
275. Diem, M.; Romeo, M.; Boydston-White, S.; Miljkovic, M.; Matthaus, C., A decade of vibrational micro-spectroscopy of human cells and tissue (1994-2004). *Analyst* **2004,** *129* (10), 880-5.
276. Gouadec, G.; Colomban, P., Raman Spectroscopy of Nanomaterials: How Spectra Relate to Disorder, Particle Size and Mechanical Properties. *Prog. Cryst. Growth Charact. Mater.* **2007,** *53* (1), 1-56.
277. Watts, J. F., X-ray photoelectron spectroscopy. *Vacuum* **1994,** *6* (7), 653-671.
278. Hachmöller, O.; Buzanich, A. G.; Aichler, M.; Radtke, M.; Dietrich, D.; Schwamborn, K.; Lutz, L.; Werner, M.; Sperling, M.; Walch, A.; Karst, U., Elemental bioimaging and speciation analysis for the investigation of Wilson's disease using muXRF and XANES. *Metallomics* **2016,** *8* (7), 648-53.
279. Behrends, T.; Kleingeld, P. Bench-top micro-XRF - a useful apparatus for geochemists? https://www.geochemsoc.org/publications/geochemicalnews/gn138jan09/benchtopmicroxrfausefulapp/ (accessed 03.04.2017).
280. Bivas-Benita, M.; Zwier, R.; Junginger, H. E.; Borchard, G., Non-invasive pulmonary aerosol delivery in mice by the endotracheal route. *Eur J Pharm Biopharm* **2005,** *61* (3), 214-8.
281. Hoet, P. H.; Brüske-Hohlfeld, I.; Salata, O. V., Nanoparticles - known and unknown health risks. *J Nanobiotechnology* **2004,** *2* (1), 12.
282. Blaske, F.; Reifschneider, O.; Gosheger, G.; Wehe, C. A.; Sperling, M.; Karst, U.; Hauschild, G.; Holl, S., Elemental bioimaging of nanosilver-coated prostheses using X-ray fluorescence spectroscopy and laser ablation-inductively coupled plasma-mass spectrometry. *Anal Chem* **2014,** *86* (1), 615-20.

283. Dias, A. A.; Carvalho, M.; Carvalho, M. L.; Pessanha, S., Quantitative evaluation of ante-mortem lead in human remains of the 18th century by triaxial geometry and bench top micro X-ray fluorescence spectrometry. *J Anal At Spectrom* **2015,** *30* (12), 2488-2495.
284. Schnieders, A.; Benninghoven, A., Detection and Quantification of Metal in Organic Materials by Laser-SNMS with Nonresonant Multiphoton Ionization. *Anal Chem* **2000,** *72*, 4289-4295.
285. Gauglitz, G.; Vo-Dinh, T., *Handbook Of Spectroscopy*. Wiley-VCH Verlag Weinheim, 2003; Vol. 1.
286. Baum, P.; Kosacka, J.; Estrela-Lopis, I.; Woidt, K.; Serke, H.; Paeschke, S.; Stockinger, M.; Klöting, N.; Blüher, M.; Dorn, M. J. M., The role of nerve inflammation and exogenous iron load in experimental peripheral diabetic neuropathy (PDN). **2016,** *65* (4), 391-405.
287. Vennemann, A.; Alessandrini, F.; Wiemann, M., Differential Effects of Surface-Functionalized Zirconium Oxide Nanoparticles on Alveolar Macrophages, Rat Lung, and a Mouse Allergy Model. *Nanomaterials* **2017,** *7* (9), 280-300.
288. Tanaka, N.; Kimura, H.; Faried, A.; Sakai, M.; Sano, A.; Inose, T.; Sohda, M.; Okada, K.; Nakajima, M.; Miyazaki, T. J. C. s., Quantitative analysis of cisplatin sensitivity of human esophageal squamous cancer cell lines using in-air micro-PIXE. **2010,** *101* (6), 1487-1492.
289. Barapatre, N.; Morawski, M.; Butz, T.; Reinert, T. J. N. I.; Materials, M. i. P. R. S. B. B. I. w.; Atoms, Trace element mapping in Parkinsonian brain by quantitative ion beam microscopy. **2010,** *268* (11-12), 2156-2159.
290. Weissleder, R.; Nahrendorf, M.; Pittet, M. J., Imaging macrophages with nanoparticles. *Nat Mater* **2014,** *13* (2), 125-38.
291. Ninomiya, S.; Nakata, Y.; Ichiki, K.; Seki, T.; Aoki, T.; Matsuo, J., Measurements of secondary ions emitted from organic compounds bombarded with large gas cluster ions. *Nucl Instrum Methods Phys Res, Sect B* **2007,** *256* (1), 493-496.
292. Ninomiya, S.; Nakata, Y.; Honda, Y.; Ichiki, K.; Seki, T.; Aoki, T.; Matsuo, J., A fragment-free ionization technique for organic mass spectrometry with large Ar cluster ions. *Appl Surf Sci* **2008,** *255* (4), 1588-1590.
293. Rajta, I.; Gomez-Morilla, I.; Abraham, M. H.; Kiss, A. Z., Proton beam micromachining on PMMA, Foturan and CR-39 materials. *Nucl Instrum Methods Phys Res, Sect B* **2003,** *210*, 260-265.
294. Proton Beam Writing. www.pbeamwriting.com (accessed 29.06.17).
295. Belu, A. M.; Graham, D. J.; Castner, D. G., Time-of-flight secondary ion mass spectrometry: techniques and applications for the characterization of biomaterial surfaces. *Biomaterials* **2003,** *24* (21), 3635-53.
296. Laux, P.; Riebeling, C.; Booth, A. M.; Brain, J. D.; Brunner, J.; Cerrillo, C.; Creutzenberg, O.; Estrela-Lopis, I.; Gebel, T.; Johanson, G. J. N., Biokinetics of nanomaterials: The role of biopersistence. **2017,** *6*, 69-80.
297. Llop, J.; Estrela-Lopis, I.; Ziolo, R. F.; González, A.; Fleddermann, J.; Dorn, M.; Vallejo, V. G.; Simon-Vazquez, R.; Donath, E.; Mao, Z. J. P.; Characterization, P. S., Uptake, biological fate, and toxicity of metal oxide nanoparticles. **2014,** *31* (1), 24-35.
298. Van Ham, R.; Adriaens, A.; Van Vaeck, L.; Gijbels, R.; Adams, F., Molecular information in static SIMS for the speciation of inorganic compounds. *Nucl Instrum Methods Phys Res, Sect B* **2000,** *161-163*, 245-249.
299. Van Vaeck, L., Molecular speciation analysis of inorganic compounds. In *TOF-SIMS: Materials Analysis by Mass Spectrometry* 2ed.; Vickerman, J. C.; Briggs, D., Eds. IM Publications LLP: Chichester, 2013.

300. Chandra, S., Challenges of biological sample preparation for SIMS imaging of elements and molecules at subcellular resolution. *Appl Surf Sci* **2008,** *255* (4), 1273-1284.
301. Kurczy, M. E.; Piehowski, P. D.; Parry, S. A.; Jiang, M.; Chen, G.; Ewing, A. G.; Winograd, N., Which is more important in bioimaging SIMS experiments-The sample preparation or the nature of the projectile? *Appl Surf Sci* **2008,** *255* (4), 1298-1304.

Chapter 12

List of Abbreviations

12. List of Abbreviations

[M±X]	Molecular Ion M with adducted/removed atom X
µ-XRF	Micro X-Ray Fluorescence Microscopy
2D	Two-dimensional
3D	Three-dimensional
BET	Brunauer-Emmett-Teller (surface area determination technique)
CCD	Charge-coupled device
CLSM	Confocal laser scanning microscope
Da	Dalton (atomic mass unit)
DC	Direct Current
DFM	Dark-field microscopy
DNA	Deoxyribonucleic acid
EI	Electron ionization
eV	Electron volt (energy unit)
FIB	Focused ion beam
FITC	Fluorescein Isothiocyanate
FM	Fluorescence Microscopy
GCIB	Gas cluster ion beam
HaCaT	Immortalized skin cell line
HeLa	He(nrietta) La(cks), (Human immortalized cell line)
IBM	Ion Beam Microscope (*i.e.* Nuclear Microscope)
IF	Instillation fluid
ITO	Indium-tin-oxide (translucent, conductive substrate material)
keV	Kilo electron Volt (energy unit)
LA-ICP-MS	Laser-Ablation Inductively-Coupled-Plasma Mass Spectrometry
LMIG	Liquid metal ion gun
m/z ratio	Mass to charge ratio
MC	Maximum counts
MCP	Multi-channelplate
MDCK II	Madin Darbey Canine Kidney (epithelial dog kidney cell line)
MeV	Mega electron Volt
MS/MS	Tandem Mass Spectrometry

nA	Nano Ampere
NanoSIMS	Sector-field SIMS from Cameca, Gennevilliers Cedex, France
nm	Nanometer
NP	Nanoparticle
NRK	Normal Rat Kidney (cell type)
ns	Nanosecond
NTA	Nanoparticle Tracking Analysis
Ω	Surface resistivity
pA	Picoampere
PIDD	Primary ion Dose density
PIXE	Particle induced X-Ray Emission
ps	Picosecond
RBS	Rutherford Backscattering Spectrometry
RGB	Red-Green-Blue
RNA	Ribonucleic Acid
ROI	Region-of-Interest
SEM-EDX	Scanning electron microscopy
SIMS	Secondary Ions Mass Spectrometry
SNMS	Secondary Neutral Mass Spectrometry
TC	Total counts
TDC	Time-to-digital converter
TI	Thermal ionization
ToF	Time-of-Flight
ToF-SIMS	Time-of-Flight Secondary Ion Mass Spectrometry
Torr	Pressure unit
UHV	Ultra-high vacuum
XPS	X-Ray Photoelectronspectroscopy
Z	Atomic number

Chapter 13

List of Figures

13. List of Figures